Numerical Investigations of the Plasma Actuator Flow Problem

by

Ajay Peter Manuel

A thesis submitted in partial fulfillment of the requirements for the degree of

Master of Science

Department of Physics
University of Alberta

Abstract

The Single Dielectric Barrier Discharge (SDBD) plasma actuator is currently considered as one among the many promising active flow-control devices. Research interest in modeling the plasma actuator is motivated by the fundamental principle of facilitating the prediction of airflow over different object configurations, and gaining further knowledge on plasma and flow properties in aerospace environments.

Two categories of plasma actuator models exist: Phenomenological (or Simplified), and First-principles-based models. First-principles-based models are generally more complex and computationally intensive compared to Phenomenological models. This work focuses on such numerical investigations of the plasma actuator. In specific, this thesis is a comparative study of Kinetic, Hybrid, and Fluid models of the SDBD plasma actuator.

Two particular models are considered including an Electrostatic (Fluid) model proposed by Orlov et al. [1], and a Particle-in-Cell (Hybrid) model constructed by the author.

The two models are tested with different configurations and environmental parameters commonly encountered in the SDBD plasma actuator flow problem.

The codes are separately verified, and validated by the comparison of results obtained to supporting literature. The electric field, electric potential, and plasma body forces are accurately modeled, albeit with minor differences.

Suggestions for corrections and modifications for model development, and efficiency were also outlined, along with the necessary prerequisite research and an agenda for future prospects.

I would like to dedicate this thesis to my ever-supportive family, and my loving partner Leina.

Acknowledgements

First, I would like to thank my family for the support they have provided me throughout my life. Thank you for giving me the strength and motivation to reach for the stars, and chase my dreams.

I would also like to thank my partner and best friend, Leina, whose love, encouragement, and support helped me to successfully complete this thesis.

And I would like to express the utmost gratitude to my supervisor Dr. Richard Sydora whose expertise, understanding, counsel, and patience helped considerably toward a beneficial graduate experience.

In conclusion, I would like to recognize that this research would not have been possible without the financial assistance of the University of Alberta's Faculty of Graduate Studies and the Department of Physics, and express my thanks to those agencies.

Contents

List of Figures

List of Tables

Chapter 1

Introduction

1.1 A Brief History of Flow Control

Historically, flow control research accompanied a human instinct to comprehend the nature of fluid behavior about object configurations, and is the humble beginning of the now expansive field of aerodynamics. The aeroplane is the foundational invention of this field. Its successful commercialization in the modern era has now fueled a growing interest in the developmental research of flow control systems to further enhance its structure and efficiency.

As stated by Gad-el-Hak [2], flow control concerns the ability to manipulate a flow for a desired change. Flow control devices come in two forms: Active, and Passive (Figure 1.1). Active flow control devices involve the addition of energy to a system via an actuator. The actuator requires auxiliary power, and is integrated in a control loop [6]. Passive flow control devices require no such support, and are largely mechanical in nature.

Mechanical flaps on an airplane wing are examples of active flow control devices. These devices generate a kind of blowing at the beginning of the wing by increasing the flow velocity close to the wall, and delaying the null velocity gradient that is the onset of separation [7]. They also enlarge the area of the wing at the back to enhance lift (Figure 1.2).

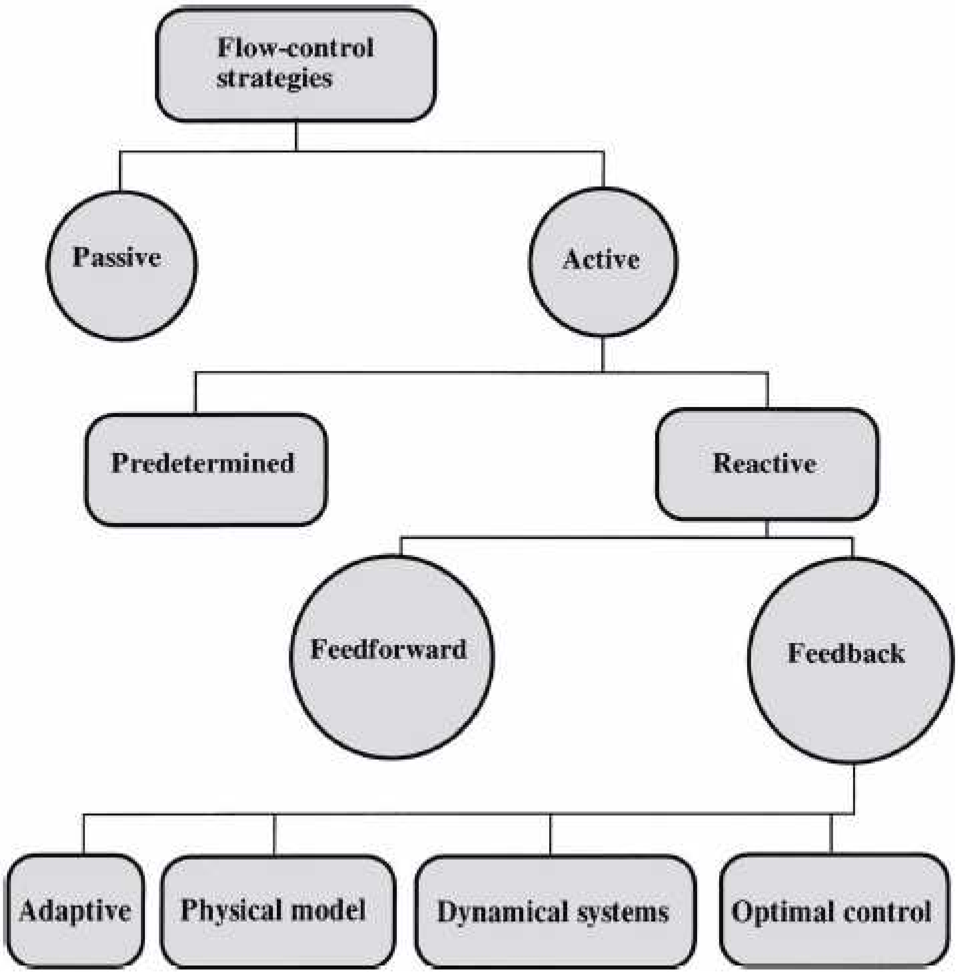

Figure 1.1: *Flow control classification [2].*

Riblets and Large Eddy Break-up (LEBU) devices are passive flow control systems. As explained by Touchard [7], Riblets are small grooves aligned with the free air-stream, and assist in modifying the boundary layer near the surface. The best shapes have been found to be a sharp peak, and sharp or round valley (Figure 1.3). LEBUs help alter and breakup vortices that appear at the outer edge of the turbulent boundary layer around an airfoil, but generally do not perform as well as Riblets since they do not produce an efficient global reduction of the resultant drag.

(a) Front Flap (b) Back Slot

Figure 1.2: *Convertible mechanical flaps [3].*

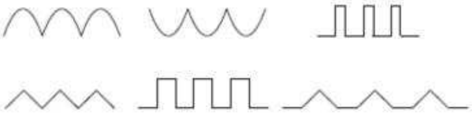

Figure 1.3: *Various shapes of riblets commonly utilized on airplane wings [3].*

In recent years, one particular active flow control device known as the Single Dielectric Barrier Discharge (SDBD) plasma actuator has shown great promise. Its popularity stems from its properties: low weight, robustness, lower power consumption, simplicity, and ability for real time control at high frequencies [8]. Like the mechanical flaps on an airplane wing, the plasma actuator is another flow control device that uses blowing, or an injection of momentum at the near-wall region to induce and modify a flow configuration. The use of plasma actuators for flow control has promoted studies on the applications of plasmas towards tackling flow control problems, and exemplifies the union of the two fields of plasma physics and modern-day aerodynamics.

The common goal of flow control studies involves the use of the aforementioned systems to achieve greater lift enhancement and drag reduction, noise suppression, transition and separation delays. Such studies are beneficial towards progressive economic and environmental industrial processes involving fluid flows, allowing for prodigious energy savings in the use of land, air, and sea vehicles [2].

Several experiments have been conducted to look at the evolution of a variety of plasma, and airflow effects with respect to different mechanical, and electrical properties of the SDBD plasma actuator [5; 6; 8; 9; 10]. Such preliminary experiments have played a vital role toward progressive research in the field. With the rapid growth of computing power and technology, these efforts have culminated in the development of numerical models for plasma actuators, paving the way towards greater understanding of the device and the inherent plasma-fluid processes involved.

1.2 Project Proposal, and Approach

In this thesis, we will begin by analyzing the physics of the SDBD plasma actuator, and its operational principles. The beneficial effects of the SDBD plasma actuator as an active flow control device arise from the electrohydrodynamic (EHD) or plasma body force through which it is able to modify the boundary layer of a flow along an arbitrary surface.

Since the development of the plasma discharge in time and space is complex, it is understood predominantly through modeling and simulation without detailed measurements at the microscopic level. But, the body force induced by the plasma component at the macroscopic level can be measured.

Thus, we will briefly review the various numerical plasma body force models that have been used to analyze the SDBD plasma actuator flow problem following which we will discuss and compare two particular models including a fluid Electrostatic model proposed by Orlov [1], and a hybrid Particle in Cell model formulated by the author.

The objectives of this work will be to test the applicability of each model with different configurations, and environmental parameters for the SDBD plasma actuator flow problem. An attempt will be made to generalize the results in order to provide for wider applicability.

The following goals will be met:

i. Comparison of the two SDBD plasma actuator models.

ii. Testing of the models based on different sets of parameters and requirements.

iii. Verification, and validation of the models.

iv. Generalization of the models, and their applicability.

v. Discussion of prospects for future research on the SDBD plasma actuator flow problem, and the numerical models.

Chapter 2

Physics of the Plasma Actuator

2.1 Fundamentals of Plasmas

All visible matter in the known universe can be categorized into four separate states: solid, liquid, gaseous, and plasma. In fact, the visible universe is predominantly composed of plasma (Figure 2.1).

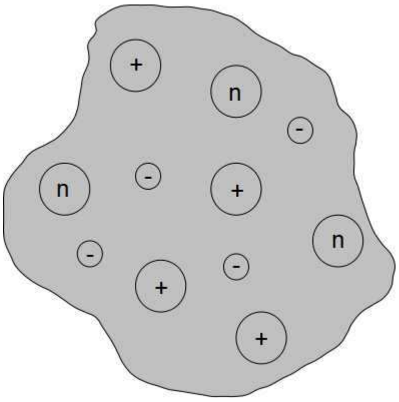

Figure 2.1: *A plasma is a quasi-neutral gas of charged particles interacting in collective behavior.*

The word *plasma* originates from the Greek language to describe something that is *molded.* Tonks and Langmuir first used the word in 1929 to describe a glowing, and ionized, but neutral gas produced by an electrical discharge in a tube [11]. If left alone, a plasma has a strong tendency to become electrically neutral, where the charge densities of ions and electrons are equivalent. This is what is meant when a plasma is said to be *quasi-neutral*.

This system of charged particles, including free electrons and ionized atoms or molecules exhibits collective behavior, similar to a continuum, through interactions via long-range electrostatic forces. Plasmas can also be identified as hot or cold. A hot plasma is fully-ionized, while most industrial applications, including plasma actuators, use cold plasmas where only a fraction of the plasma is ionized [6].

2.2 Physics of the Plasma Actuator

2.2.1 Introduction

There are several configurations of plasma actuators that span existing literature. Research on these devices is relatively recent, with preliminary studies first initiated in the early 1950s in Europe, and the USA [8]. The steady development of micro-scale technologies and plasma applications promoted scientific interest, resulting in the publication of various experimental tests, and modeling techniques supporting the use of plasma actuators as potential devices for active flow control.

Plasma actuators are now considered to be naturally superior to other commonly used mechanical devices for flow control. Although they are efficient, mechanical devices tend to be heavy, adding weight and volume, and are also sources of noise and vibration [8]. Due to their inherent mechanical composition, such devices are also at risk of wear and tear, and may completely breakdown through overuse. Plasma actuators do not suffer these drawbacks.

The main advantages of the plasma actuator, contributing to its natural preference over other traditional mechanical flow control devices, include its reduced size and weight, which is particularly important in applications with high-g loads [9], as well as an absence of moving parts, robustness, increased reliability, inexpensiveness, fast time-response, and the ability to be applied onto surfaces without requiring holes or cavities [1; 5; 8; 9]. The plasma actuator's efficient conversion of input electric energy into output fluid momentum is of great significance, and the straightforward nature of simulating the effects of the device using numerical flow solvers is also an asset [9].

It is necessary to fully comprehend the operational principles of the plasma actuator, and revise the knowledge we have gleaned from the various experimental results that have been procured on the physical properties of the device before proceeding with its modeling, and analysis.

2.2.2 The SDBD plasma actuator

The SDBD is the most commonly used configuration of plasma actuators. It consists of two electrodes asymmetrically positioned, and separated by a dielectric material. One of the electrodes is exposed to the airflow while the other is encapsulated within the dielectric material. The electrodes are long and thin, arranged in a span-wise direction on the aerodynamic surface, and connected to a DC or AC voltage power source. The encapsulated electrode is usually grounded [1]. A rough schematic of the asymmetric SDBD is provided in Figure 2.2.

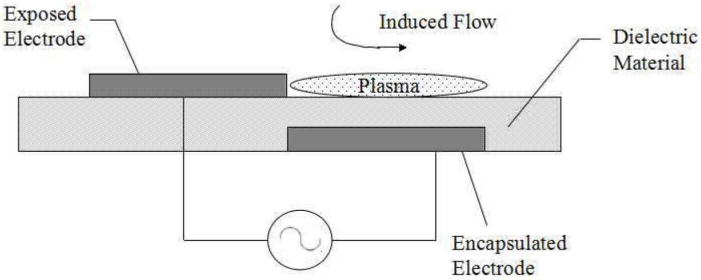

Figure 2.2: *Schematic of the asymmetric SDBD plasma actuator.*

AC voltages are generally preferred as they provide for a more stable plasma discharge in the presence of a dielectric barrier. Nevertheless, other methods have been developed to enable the use of DC voltages to provide for stable plasma discharges in the presence of a dielectric barrier. One method involves the use of a high resistivity layer covering one of the electrodes, otherwise known as the

Resistive Barrier Discharge plasma actuator [12]. Another method involves the use of a semiconductor layer of gallium arsenide (GaAs) to replace the dielectric layer, allowing for the device to be driven by a DC voltage between 580 V and 740 V [13]. This will be discussed in greater detail through the course of our work.

For the SDBD plasma actuator, an AC voltage of a peak value of 5-20 kV is usually applied to the electrodes at a frequency range from 3-15 kHz [1; 6]. This results in the formation of a plasma discharge above the encapsulated electrode on the surface of the dielectric, due to the ionization of air, aptly providing the device its moniker as a plasma actuator. The plasma is blue in color, and of low emission intensity [5; 9]. A dark space is required to view the plasma by eye. It is this plasma discharge that modifies the airflow by injecting momentum into the boundary layer region. This momentum addition can be used for flow control purposes. We will elaborate on this process in the following sections.

2.2.3 Debye Length, and Shielding

The *Debye length* is the distance over which deviations from macroscopic neutrality can naturally occur. An individual charged particle can *communicate* its electric field, its presence, to its neighboring particles in a plasma over the distance of a Debye length.

Debye shielding describes how the charged particles in a plasma can rearrange themselves such that they *shield* out any electrostatic field within a distance on the order of a Debye length. The shielding is attributed to the collective behavior of the charged particles in a plasma, and helps sustain its quasi-neutrality. As such, the influence of electrostatic interaction potentials caused by say, the insertion of a single charged particle within the plasma, can be averted. Beyond the Debye length, this shielding mechanism effectively vanishes and deviations from macroscopic neutrality occur naturally. As Bittencourt states [11], the charged particles now respond to large interaction potentials, and move freely to neutralize other regions of excess space charge.

The Debye length is defined as,

$$\lambda_D = \Big[\frac{e^2 n_0}{\epsilon_0}\Big(\frac{1}{kT_i} + \frac{1}{kT_e}\Big)\Big]^{-\frac{1}{2}}, \tag{2.1}$$

where n_0 is the background plasma density, k is the Boltzmann constant, ϵ_0 is the permittivity of free space, T_i and T_e are the temperatures of the ion and electron species. Roth [4] states that for industrial plasmas, the Debye length is approximately 0.00017 m, and the density of charged particles is about 10^{16} $particles/m^3$.

2.2.4 Plasma Frequency

A gradient in space-charge fields is formed when a plasma is disturbed from equilibrium, resulting in collective wave-like oscillatory particle motions that work to restore the original macroscopic neutrality.

The *plasma frequency* is the time-scale used to describe the collective natural frequency of such oscillations. These oscillations are inherently related to the stability of a plasma's charge neutrality. Therefore, as Bittencourt [11] states, the plasma frequency can be used to analyze the damping mechanisms that may destroy the collective motion of charged particles in a plasma.

Electrons, due to their smaller mass relative to the heavier ions, constitute these plasma oscillations, and provide the restoring force in a plasma. The electron plasma frequency, ω_{pe}, is defined as,

$$\omega_{pe} = \sqrt{\Big(\frac{n_e e^2}{m_e \epsilon_0}\Big)}, \tag{2.2}$$

where n_e is the electron number density, e is the elementary charge of an electron, m_e is the mass of an electron, and ϵ_0 is the permittivity of free space. In a typical gas discharge, the electron plasma frequency is ≈ 6 GHz. Collisions between electrons and neutral particles can be a source of oscillatory dissipation, resulting in the dampening of the collective oscillations, and a reduction of their amplitude. These collisions are generally dictated by the Coulomb force. In a plasma, a

Coulomb collision rarely results in a large deflection, but the cumulative effect of many small angle collisions is often larger than the effect of a few large angle collisions. Thus, when it comes to plasmas, it is usually preferable to consider collision dynamics involving the limit of small angle deflections. Particle collisions and interactions in a plasma usually involve binary interactions with elastic, and inelastic collisions. Common models of such interactions involve the Hard-Sphere, and Coulomb Potential models. In order for the collisions to be only slightly damped, it is necessary that the electron collision frequency ν_{en} is smaller than the electron plasma frequency,

$$\nu_{pe} > \nu_{en}, \tag{2.3}$$

where $\nu_{pe} = \frac{\omega_{pe}}{2\pi}$. This condition can be rewritten as,

$$\omega\tau > 1, \tag{2.4}$$

where $\tau = 1/\nu_{en}$ representing the average time an electron travels between collisions with neutral particles, and ω is the angular frequency of typical plasma collisions. In other words, in a plasma, it is necessary that the time-scales at which electron-neutral collisions transpire be large compared to the time-scale during which the physical parameters of a plasma are changing.

In an interstellar gas, τ is relatively large with a small neutral particle number density. Therefore, electrons behave independently and the medium can be treated as a plasma. But when the number density of neutral particles is far larger than that of the number density of electrons, the motion of the electrons will be coupled to the neutral particles resulting in nothing more than a neutral gas. The Plasma Frequency, together with Macroscopic Neutrality and Debye Shielding, are the three main properties that fundamentally define plasma behavior.

2.2.5 Operational Principles

Plasma actuators, in general, involve the use of *non-thermal atmospheric pressure plasmas* or plasmas that are not in thermodynamic equilibrium. This can be due to either the ion and electron temperatures being different, or if the distribution of velocities of either of the two species does not satisfy the Maxwell-Boltzmann distribution [11]. Non-thermal plasmas can be produced by a variety of electrical discharges, and are of low energy cost as most of the electrical energy is utilized for the production of high energy electrons, rather than the heating of the surrounding gas [8].

The formation of the SDBD plasma is based on the Townsend mechanism. This is an electron avalanche process involving the multiplication of an initial set of free electrons through cascade ionization [8]. The behavior of the SDBD plasma actuator is strictly defined by this charge mechanism in alternating half-cycles by the AC voltage power source. Simply put, when an AC voltage is applied to the electrodes, a plasma discharge appears on the surface above the encapsulated electrode, injecting momentum into the surrounding air during each half-cycle of the applied voltage. This injection of momentum is characterized as a macroscopic EHD or plasma body force that can be measured, and is transferred to the neutral continuum through collisions between charged and neutral particles. In fact, while the plasma appears to be a relatively uniform diffuse discharge, measurements have indicated that it is highly ordered in space, and time [1]. The SDBD is widely preferred due to its ability to be able to sustain a large volume discharge at atmospheric pressure without the discharge collapsing into a constricted arc [9]. This is because the configuration of the SDBD plasma actuator is inherently self-limiting; a behavior that is dictated by the build-up of charges on the dielectric surface.

Let us consider this in more detail. We begin with the half-cycle of the discharge where the exposed electrode is of greater negative potential compared to the encapsulated electrode, as shown in Figure 2.3. In other words, the exposed electrode acts as a cathode, while the encapsulated electrode, or rather, the dielectric surface, acts as an anode. As stated by Orlov [1], electrons are emitted from the exposed electrode when the electric potential is large enough, and are deposited onto the dielectric surface. In the space between the electrodes, these primary electrons induce an electron avalanche by ionization of neutral air particles as

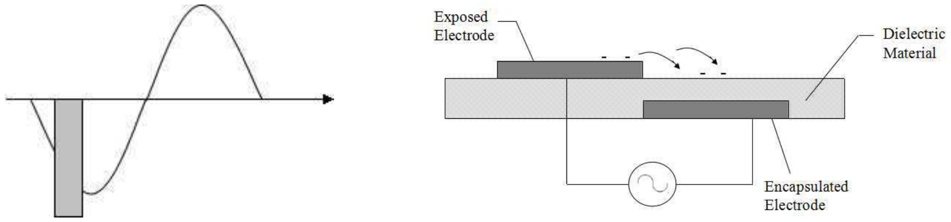

(a) AC voltage input for the corresponding cycle.

(b) Deposition of electrons on the dieletric layer.

Figure 2.3: *Forward-Phase Charge Cycle*

they continue their drift from the cathode to the anode. A plasma discharge is then created. By definition, momentum is injected or transferred to the flow through the collisions of these charged and neutral particles. Electrons contribute little to the momentum transfer due to their small mass in contrast to the more massive ions. The plasma is formed as the result of a series of discharges, as electrons are transferred onto and off the dielectric surface.

Meanwhile, the dielectric surface opposes the applied voltage on the exposed electrode in response to the charge buildup. As electrons move toward the positive electrode, and ions move to the negative electrode, a charge imbalance similar to an electric dipole is set at the edges of the plasma. This charge imbalance forms an internal electric field that opposes the external electric field (due to the AC voltage). The rearrangement of the charged particles continue until the net electric field in the plasma is neutralized. Thus, the discharge is self-limiting in that it is shut off unless the magnitude of the applied voltage is continually increased.

In the opposite half-cycle, electrons return to the exposed electrode as presented in Figure 2.4, where the dielectric surface is of greater negative potential playing the role of the cathode. The charge available to the discharge is now delimited to the amount that was deposited in the previous half-cycle onto the dielectric surface. This self-limiting behavior of the SDBD plasma actuator helps avoid the formation of an unfavorable arc-discharge. An arc discharge can have harmful effects on electronic equipment and results in an unstable plasma [8]. A stable glow discharge is instead observed. The net effect of the plasma on the flow is

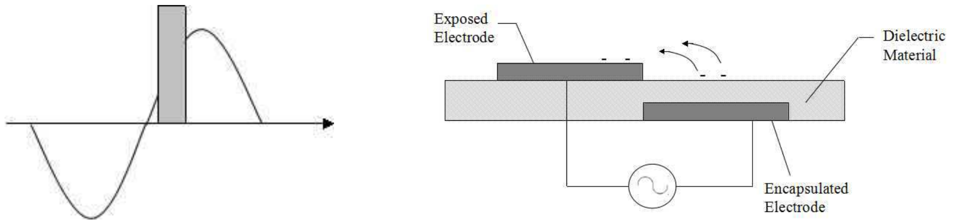

(a) AC voltage input for the corresponding cycle.

(b) Deposition of electrons onto the exposed electrode.

Figure 2.4: *Backward-Phase Charge Cycle*

measured, and observed as a localized body force.

2.2.6 Temporal Scales in the SDBD process

Temporal cycles within the plasma are dictated by the motion of the charged species in response to the externally applied electric field. The formation of the plasma discharge is a highly dynamic, spatially evolving, non-equilibrium process. Time-resolved observations of the ionization process have shown that the discharge's features develop on the timescale of the AC period of milliseconds or less [5]. Further observations and calculations made by Orlov [1], and Vidmar et al. [14] have identified three distinct timescales in the SDBD process:

i. The shortest time scale, on the order of 10^{-8} s, is associated with the time required for charge rearrangement for net neutrality in the plasma.

ii. The second timescale refers to the operational cycles of the plasma actuator, and is defined by the period of the AC cycle that supports the alternating electrical discharge. This is on the order of 10^{-4} s.

iii. Lastly, the third timescale corresponds to the collective motion of the neutral continuum (airflow) in response to the plasma actuator, and is on the order of 10^{-2} s.

2.2.7 Mechanical and Electrical properties

The primary mechanism behind the SDBD plasma actuator's ability to manipulate or induce a flow configuration is the ionized air that appears over the dielectric

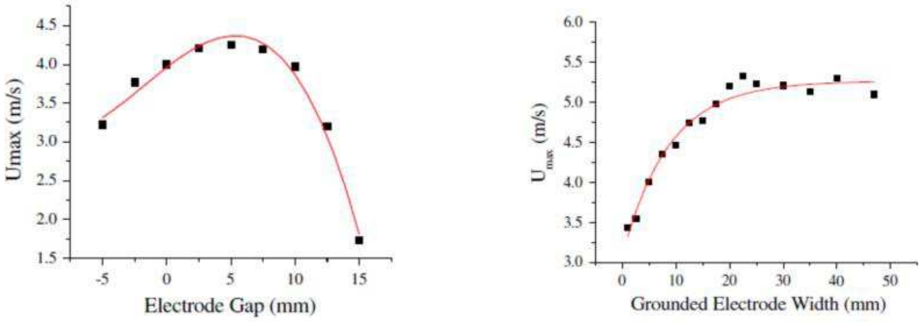

(a) (b)

Figure 2.5: U_{Max} as a function of electrode gaps, and widths [4].

surface. In the presence of the electric field produced by the electrode geometry, the ionized air results in a body-force that acts on the ambient, neutrally charged air. This effect is classically termed as an electric wind, directed from the exposed electrode toward the dielectric surface, that modifies the boundary layer, and allowing for the active manipulation of the airflow [7; 8; 9]. This act of producing a mechanical output or kinetic energy, for an electrical input or electric energy, without the use of mechanical moving parts, classifies the plasma actuator as a Micro-Electro-Mechanical-System (MEMS) [8].

The SDBD plasma actuator usually involves electrodes with widths of a few mm, and thicknesses between 0.1, and a few *mm* [8]. The electrode gap is equal to zero, with a chosen dielectric among various materials from Teflon, Kapton, Glass, Ceramics, or Plexiglass. The variance of the representative parameters concerning these parts of the device can result in differing mechanical effects including: electric wind velocity (measured using Particle-Image Velocimetry (PIV) or Laser Doppler Velocimetry (LDV)), mechanical power, and electric force.

For example, Forte et al. [15] performed a parametric study to increase the plasma actuator's induced velocity. Figures 2.5a-2.5b present their observations on the evolution of the maximum induced velocity as a function of the electrode gap (g), and the encapsulated electrode width (w). The plasma actuator system in these cases involve a 2 *mm*-thick Plexiglass plate, with two 5 *mm*-wide electrodes, with an applied voltage $V = 20\ kV$, and frequency $f = 700\ Hz$. A rough schematic of the general configuration is provided in Figure 2.6.

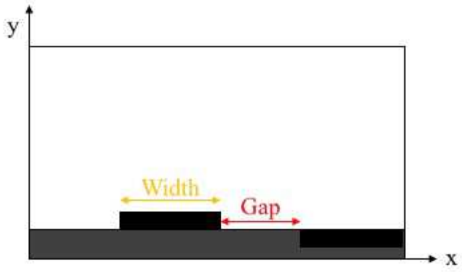

Figure 2.6: *Electrode Gaps and Widths in Forte's experiments.*

The influence of different parameters on the generated plasma, and the induced velocities was observable. The maximum induced velocity was almost always found to be at a distance of y=0.5 mm above the dielectric surface. An optimum electrode gap of 5 mm was noted. For g greater than 5 mm it was postulated that the electric field may fall down, and that the space charge may not be able to make it to the downstream electrode.

A second series of measurements were made using the same actuator configuration but with $g = 0$ and the encapsulated electrode width (w_B) increased little by little. Figure 2.5b shows that the induced velocity above the dielectric surface increases with the electrode width, and eventually levels off. It could be said that the wider the electrode, the greater the plasma extent. Thus, ions are accelerated for a longer distance, resulting in an increase in induced velocity magnitudes. On the other hand, since the process behind the formation of a self-sustaining plasma is dissipative (as reviewed earlier in the formation of the plasma discharge dictated by AC voltage half-cycles, the self-limiting nature of which delimits the number of electrons deposited onto the dielectric surface, which can influecne the plasma extent), the plasma was found to not expand more than about 20 mm. This led to the conclusion that the best configurations involve $g = 0$ and $w_B = 20\ mm$, or $g = 5\ mm$ and $w_B = 15\ mm$.

Another experiment by Forte [15] captures the velocity profiles for varying voltages above the dielectric surface, as presented in Figure 2.7. Y in units of mm represents the vertical distance above the dielectric surface. The plasma actuator configuration here consisted of a 4 mm-thick glass plate, with an electrode gap and electrode width equal to 5 mm. A constant frequency of 300 Hz is utilized for all voltage values.

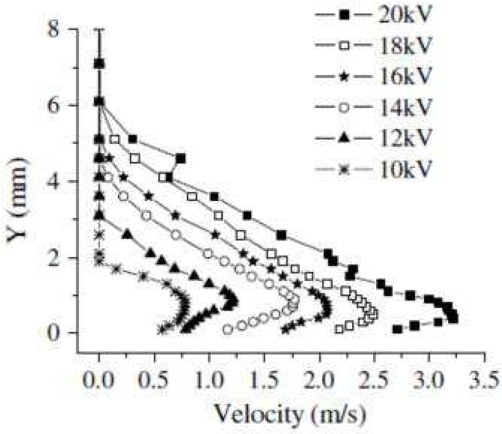

Figure 2.7: *Variance of the velocity profile near the dielectric surface [4].*

Along with various other experimental efforts as outlined by Moreau [8], a general conclusion can be drawn that the plasma actuator's influence on the induced flow field and the plasma formation is a function of several parameters ranging from the AC voltage amplitudes and frequencies, electrode configurations, and dielectric materials etc.

2.3 Modeling of the Plasma Actuator

The effectiveness of plasma actuators in controlling flow separation has been thoroughly demonstrated by several researchers. Many such experiments, as discussed in the previous section, focused on the modification of the physical and macroscopic parameters of the plasma actuator system. The major drawback with this approach is the large number of parameters that are involved, making it incredibly difficult to monitor the system's dynamic behavior at short timescales.

The macroscopic effects of the plasma actuator on the airflow is highly influenced by its microscopic structure. The SDBD plasma is typically small in the physical sense, ranging from 2-3 mm in height and 1-2 cm in width. It is composed of multiple micro-discharges of short duration, around tens of nanoseconds, varying significantly over the period of the source AC voltage at about 0.1-10 ms [16]. This makes direct measurements on microscopic properties such as the number density of the charged species, and the electric field, extremely difficult.

Numerical modeling, and simulations serve as efficient alternatives providing useful and flexible tools to model the development of the SDBD in space and time, as well as monitor the continued evolution of such complex flow control systems. The SDBD plasma actuator generates an EHD or plasma body force that inherently depends on the electric field $\vec{E}(\vec{r}, t)$ produced by the electrode geometry, and the charged particle densities $n_i(\vec{r}, t)$ as a function of position $\vec{r}$ and time t integrated over the volume V of the plasma,

$$\vec{F}_i(t) = \int_V q_i n_i(\vec{r}, t) E(\vec{r}, t)\, dt, \tag{2.5}$$

and summed over all species,

$$\vec{F}_{EHD}(t) = \sum_i \vec{F}_i(t), \tag{2.6}$$

where q_i is the corresponding charge of the particle species.

Over the years, various body force models have been proposed. These models can be classified into two categories: Phenomenological (or Simplified), and First-Principles-Based models. *Phenomenological* models involve approaches with reduced complexity providing reasonable qualitative correspondence with experimental observations. Such models are limited in their ability to accurately predict, and explain the physics involved. Meanwhile, *First-Principles-Based* models distinctly address the necessary knowledge required towards understanding the fundamental physical processes involved [6; 10]. Let us begin by briefly reviewing the prominent models in the two categories. The reader is referred to the corresponding literature, for more detail.

2.3.1 Phenomenological Models

2.3.1.1 Roth Model

This is one of the earliest models present in the literature, and is based on the approximation that the body forces can be taken to be similar to forces in gaseous dielectrics as given by Landau, and Lifshitz [17]. Thus, the body force is defined as,

$$||\vec{f_b}|| = \frac{d}{dx}(\frac{1}{2}\epsilon_0||\vec{E}||^2). \tag{2.7}$$

This model was deficient in its static formulation and inability to account for the presence of charged particles, both of which are of great importance in experiments [5; 18]. This was re-iterated by work done by Boeuf and Pitchford in their derivation of (2.7) [19]. Enloe et al. also showed that the body force given by this equation is correct only in the special case of a 1D condition, and is not applicable to physical scenarios in two dimensions [20].

2.3.1.2 Electrostatic Model

This model utilizes the Enloe formulation of the plasma electromagnetics [18] assuming that the electric field is due to two additive components: the external electric field due to the voltage of the electrodes, and the electric field due to the charged particles [21; 22]. A Gaussian charge distribution is assumed, and is used to compute the body force produced by the plasma. The model's main advantage is its simplicity, making it fast and easy to implement. The separation of the electric field into the two aforesaid components also allows the body force to be decoupled from the flow field [6]. But, while the model is qualitatively correct in its portrayal of the net body force vectors, the scaling of the AC voltage is incorrect [5].

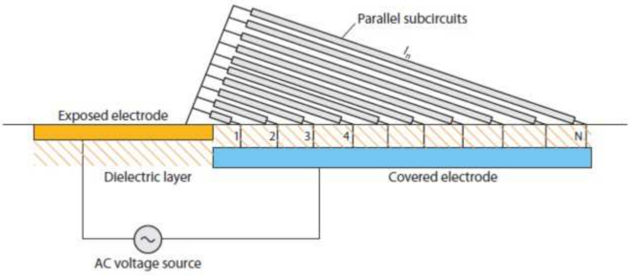

Figure 2.8: *Lumped-Element Circuit Model where the region over the encapsulated electrode is divided into N sub-regions each representing a parallel arrangement of circuit elements [5].*

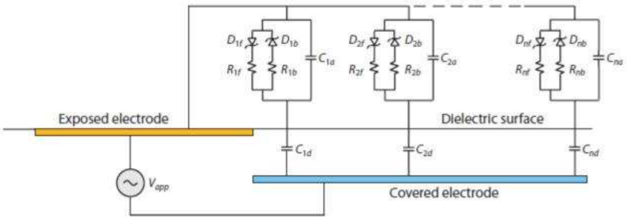

Figure 2.9: *A closer look at the circuit model [5].*

2.3.1.3 Lumped-Element Circuit Model

This model was suggested by Orlov et al. [23] to address the necessities of efficiently predicting the body forces produced by SDBD plasma actuators. As reviewed by Corke [5], the model divides the area over the covered electrode into N parallel networks, each of whose properties are unique depending on its distance from the exposed electrode as seen in Figure 2.8. The corresponding schematic of electric circuits is provided in Figure 2.9.

Each network is characterized by capacitors representing air and the dielectric layer, along with a plasma-resistive element. The plasma's time-dependent behavior, due to the AC voltage half-cycles, is applied within each of these lumped-element circuits. The plasma is assumed to operate in a quasi-steady state. When the charge distribution is disturbed, the charges cancel the external electric field everywhere except near the electrodes or the plasma edge [6]. This assumption can follow through when modeling the plasma, and computing the body force.

Maxwell's equations are used to obtain a function to describe the body force per volume of plasma, which is then solved with a set of five equations using the lumped-element circuit model.

In conclusion, while the lumped-element circuit model is computationally efficient, it is not without its drawbacks as it requires empirically determined coefficients which are functions of the frequency of the voltage supplied. Thus, it is valid for only one single frequency [5; 6].

2.3.1.4 Other Models

Shyy et al. [24] have presented a model that assumes the linear decrease of the electric field strength from the edge of the exposed electrode to the encapsulated electrode. This assumption was later found to be inconsistent with empirical measurements which showed an exponential spatial decay [20; 23]. The model was also found to produce body force vectors that point away from the dielectric surface, and with magnitudes being a linear function of the AC voltage rather than $V^{3.5}$ as observed in experiments [5].

Likhanskii et al. [25] provide a model of a weakly ionized-air plasma that is a mixture of four components including neutral molecules, electrons, positive, and negative ions. This mixture included ionization and recombination processes, and the simulations displayed the significance of the presence of negative ions in the air [5]. Such charged-particle models have been helpful in understanding the charging of the dielectric surface by electrons in the forward half-cycle phase, and its significance in helping pull positive ions forward and accelerate the gas in the backward half-cycle-phase. But, the models are time-consuming and require enormous computational resources particularly when applied to natural flow conditions at atmospheric pressures. These models are not suitable as practical design tools for the simulation and optimization of plasma actuators as flow control devices.

2.3.2 First-Principles-Based Models

2.3.2.1 Kinetic Models

Kinetic models describe the macroscopic properties of fluids by studying the interactions of their molecular composition and motion [6]. With the SDBD, this can include the interaction between a plasma and the electric field, or that between the plasma and neutral particles in the air. These models generally involve solving the Boltzmann equation of the relevant species' velocity or energy distribution function in space and time, or particle simulations such as Monte-Carlo methods [10].

The Boltzmann equation is defined as an equation for the distribution function $f(\vec{r}, \vec{v}, t)$ in phase space where $\vec{r}$ is the position of the particle, and $\vec{v}$ is the velocity of the particle at time t such that,

$$\frac{\partial f_\alpha}{\partial t} + \vec{v}_\alpha \cdot \nabla f_\alpha + \vec{a}_\alpha \cdot \nabla_v f_\alpha = \left(\frac{\partial f_\alpha}{\partial t}\right)_{coll}, \tag{2.8}$$

where the index α refers to the individual charged particle species. Using the del operator notation,

$$\nabla = \hat{x}\frac{\partial}{\partial x} + \hat{y}\frac{\partial}{\partial y} + \hat{z}\frac{\partial}{\partial z} \tag{2.9}$$

,

and similarly the del operator in velocity space is,

$$\nabla_v = \hat{x}\frac{\partial}{\partial v_x} + \hat{y}\frac{\partial}{\partial v_y} + \hat{z}\frac{\partial}{\partial v_z}. \tag{2.10}$$

The particle acceleration $\vec{a}_\alpha$ can be defined as,

$$\frac{\vec{F}(\vec{r}, t)_\alpha}{m_\alpha}, \tag{2.11}$$

or the force field acting on the particles in the fluid, where m_α is the mass of the particle species. In modeling the SDBD plasma, it is generally assumed that the current is low enough such that self-induced magnetic fields can be ignored.

Therefore, only electric forces are considered, hence the force is proportional to the electric field, and particle charge,

$$\vec{F}_\alpha = q_\alpha \vec{E}_\alpha. \tag{2.12}$$

The term on the right hand side of Equation 2.8 is the collision term and describes collisions between particles. In order to obtain a self-consistent solution, one needs to solve for the electric field $\vec{E}$ using Poisson's equation,

$$\nabla \cdot \vec{E} = \frac{\rho}{\epsilon_0}, \tag{2.13}$$

where $\rho = e(\sum n_i - n_e)$ is the charge density of the ions (assumed to be singly ionized) and the electrons, and ϵ_0 is the vacuum permittivity.

The solution of the Boltzmann equation is inherently a multi-dimensional and time-dependent problem. Furthermore, given the short timescales of electron collision and relaxation, this system of equations is exceedingly difficult to solve without simplifying assumptions. The collision term in (2.8) is non-linear and is modeled using the Monte-Carlo method.

Monte-Carlo methods are particle techniques. One such method, known as the Direct Simulation Monte-Carlo (DSMC) method is used to model the collision term in the Boltzmann equation [10]. The main assumption in DSMC methods is that particle motion can be decoupled from particle collisions if an appropriately small time-step is used. The collisions themselves are calculated using existing statistical collision model.

Particle-in-Cell (PIC) techniques are also a common alternative in modeling the collision term. The PIC method follows the motion of particles in prescribed force fields, based on the fundamental, and deterministic laws of classical mechanics [10]. The simulation region is divided into a cellular grid, which is then used to solve for the force field helping determine the force on each particle inside a given cell. The equations of motion of each particle are integrated to get the new position, and velocity.

All in all, Monte-Carlo methods are statistical in nature compared to their deterministic counterparts in PIC techniques. An integrated PIC-MC has been demonstrated by Nitschke, and Graves [26]. A direct solution of the Boltzmann equation is possible, but is time consuming.

2.3.2.2 Fluid Models

Unlike the computationally intensive Kinetic models, Fluid models incorporate the use of transport equations for the charged and neutral species' concentration, momentum, and energy i.e. the moments of the distribution function. The n*th* moment of a distribution function, about a mean value c is given by,

$$\mu_n = \int_{-\infty}^{\infty} (x-c)^n f(x)\, dx, \tag{2.14}$$

with x being either the space or velocity coordinate. The distribution function is usually not known. In order to solve for the moments, one can utilize any of the following three methods [6; 11],

i. Assume the form of the distribution function.

ii. Use basis functions as a means to define and expand the distribution function.

iii. Use phenomenological equations to describe integrals of the distribution function.

The governing equations for each species consist of the Continuity, Momentum, and Energy equations. This forms a system of equations that can be solved together with Poisson's equation,

$$\nabla \cdot \vec{E} = \frac{e}{\epsilon_0}(\sum n_i - n_e). \tag{2.15}$$

The various parameters used in these conservation equations are obtained either by directly solving the Boltzmann equation, or from empirical data.

2.3.2.3 Hybrid Models

Fluid models lose their validity at environments involving lower pressures less than 100 mTorr [6]. Such models are also prone to error in cases where there are large deviations from system equilibrium usually due to the presence of strong gradients or transient effects. Kinetic models are highly descriptive but are computationally expensive methods.

Hybrid models are utilized when there is a need for the high accuracy and the descriptive results of the kinetic models, along with the computational efficiency of fluid models. In using these models we try to strike a balance between obtaining accurate and efficient results [10]. For example, if one were to use a hybrid model to simulate a plasma environment, regions with small particle number densities and strong fields would be computed using a particle model, while regions with weak fields and large particle number densities would be treated with the fluid model. A model interface would be used to monitor the transitions between the two regimes [27].

2.4 Conclusion

It is up to the individual to choose appropriately between these modeling approaches with consideration of the phenomena being investigated. In this work, we focus on two particular methods to understand and evaluate the SDBD plasma actuator system: a fluid electrostatic model by Orlov [1], and a hybrid PIC model formulated by the author. Both models are based on first-principles. Our goal will be to provide a comparative study of the two models in their application to the SDBD plasma actuator flow problem focusing specifically on the formation of the plasma body force.

Chapter 3

Orlov's Electrostatic Model

3.1 Theoretical Overview

This chapter discusses the mathematical, and numerical formulation of Orlov's Electrostatic model for the SDBD plasma actuator. The governing equations for the electrostatic theory of the SDBD plasma actuator flow problem will be presented, and the corresponding solution for the body force of the plasma will be derived.

Some facts pertaining to this flow problem are that,

- Velocities for fluid transport processes are on the order of 10-100 m/s.
- Electron velocities, and the subsequent motion of electrons that describes plasma formation, are on the order of 10^5 to 10^6 m/s for electron temperatures ranging between 1000-10000 K [4].

Orlov's model utilizes the assumption of the differing velocity time scales in the SDBD process to decouple the problem into two separate parts involving the plasma body force formation, and the fluid flow response [1]. We will focus mainly on the numerical formulation of the model involving the derivation of the electrostatic equations concerning the solution for the plasma body force vector.

3.2 The Electrostatic Model

3.2.1 Governing Equations

The plasma is a quasi-neutral system with an equal distribution of positive and negative charges throughout its volume. It can be assumed that charged particles in the plasma have sufficient time to redistribute themselves to maintain this quasineutrality.

The governing equations used to represent the electrostatics of the plasma actuator flow problem can be derived by simplifying Maxwell's equations,

$$\begin{gathered}\oint_P \vec{H} \cdot d\vec{L} = \int (\vec{J} + \tfrac{\partial \vec{D}}{\partial t}) \cdot d\vec{S}, \\ \oint_P \vec{E} \cdot d\vec{L} = -\int \tfrac{\partial \vec{B}}{\partial t} \cdot d\vec{S}, \\ \oint_A \vec{D} \cdot d\vec{S} = \int \rho_c \, dV, \\ \oint_A \vec{B} \cdot d\vec{S} = 0,\end{gathered} \tag{3.1}$$

where $\vec{H}$ is the magnetic field strength, $\vec{B}$ is the magnetic flux density, $\vec{E}$ is the electric field, $\vec{D}$ is the electric displacement, $\vec{J}$ is the electric current density (excluding the dielectric), ρ_c is the charge density (excluding the dielectric), while P is the path of integration, and A is the bounding area or surface of the volume V. In differential form, this system of equations is rewritten as,

$$\begin{aligned}\nabla \times \vec{H} &= \vec{J} + \frac{\partial \vec{D}}{\partial t}, \\ \nabla \times \vec{E} &= -\frac{\partial \vec{B}}{\partial t}, \\ \nabla \cdot \vec{D} &= \rho_c, \\ \nabla \cdot \vec{B} &= 0.\end{aligned} \tag{3.2}$$

With reference to the temporal scales in the plasma actuator flow problem (Section 2.2.6), the orders of magnitude difference in time scales between the collective motion of the neutral continuum i.e. the fluid response and the charge arrangement, justifies the assumption that the plasma formation and charge rearrangement processes are instantaneous. Due to this, Orlov considers the plasma to be quasi-neutral-steady, resulting in the following simplifications:

- The electric current density, $\vec{J}$, the magnetic field strength, $\vec{H}$, and the magnetic flux density, $\vec{B}$, can be set to zero.
- The corresponding partial time derivatives of the electric displacement, $\frac{\partial D}{\partial t}$, and the magnetic flux, $\frac{\partial \vec{B}}{\partial t}$ can also be set to zero.

This leaves us with one Maxwell equation that describes the density of charged particles in our system,

$$\nabla \cdot \vec{D} = \rho_c. \tag{3.3}$$

The electric displacement, $\vec{D}$, is defined as,

$$\vec{D} = \epsilon \vec{E}, \tag{3.4}$$

where $\epsilon = \epsilon_0 \epsilon_r$ with ϵ_0 the vacuum permittivity, and ϵ_r the relative permittivity or dielectric coefficient of the media. Similarly, the electric field can be defined via the electric potential,

$$\vec{E} = -\nabla \phi. \tag{3.5}$$

Substituting equations (3.4), and (3.5) into (3.3) we arrive at Poisson's equation, which says,

$$\nabla(\epsilon_r \nabla \phi) = -\frac{\rho_c}{\epsilon_0}. \tag{3.6}$$

In order to examine the mechanism by which the SDBD plasma strives to shield itself from the disturbing influence of the external electric field due to the imposed voltage on the electrodes, we consider the scenario of a plasma gas subjected to an electric field. This is similar to the classic example in plasma physics where this electric field is due to an external charged particle, or even one of the charged particles inside the plasma, isolated for observation. Our goal is to determine the electrostatic potential $\phi(\vec{r})$ and the corresponding internal electric field $\vec{E}(\vec{r})$ established in the plasma due to the combined influence of the external electric field and the distribution of charged particles in the discharge. We are assuming a two dimensional electric field such that $\vec{r} = (x, y)$ for the plasma actuator flow problem.

A plasma can be considered as a conducting fluid, without specifying its composition of various individual species. Therefore, the macroscopic transport equation to describe the behavior of the plasma as a whole can be written without considering the individual species present [11]. Each macroscopic variable is rather combined by adding the contributions of the various particle species in the plasma. The equation of motion for a plasma gas subjected to an electric field acting along a single direction s can then be written as,

$$mn\Big[\frac{\partial \vec{u}}{\partial t} + (\vec{u} \cdot \vec{\nabla})\vec{u}\Big] = qn\vec{E} - \nabla \cdot \mathrm{P}, \tag{3.7}$$

where mn represents the mass density of the charged particles (ions and electrons) in the plasma gas, and $\vec{u}$ is the mean velocity of the plasma gas, since the velocity of each species is weighted proportionally to its mass density. qn is the corresponding electric charge density, and P is the total kinetic pressure dyad of the plasma gas. The kinetic pressure dyad for each particle species in the plasma is generally defined as,

$$\mathrm{P}_\alpha = n_\alpha m_\alpha < \vec{c}_\alpha \vec{c}_\alpha >, \tag{3.8}$$

where $\vec{c}_\alpha = \vec{v} - \vec{u}_\alpha$ is the peculiar or random velocity of the type α particles relative to the average velocity $\vec{u}_\alpha$. The peculiar velocity is associated with the random or thermal motions of the particle species. The term $-\nabla \cdot \mathrm{P}$ is the force exerted in a unit volume of plasma due to the random variations of the particles' peculiar velocities. This volumetric force also accounts for forces associated with the scalar pressure and viscous forces. Viscous effects are relatively unimportant in plasmas [11]. Additionally, if the distribution of peculiar velocities is isotropic, P corresponds to a scalar kinetic pressure p.

Orlov's model neglects viscous effects and assumes an isotropic velocity distribution which makes $-\nabla \cdot \mathrm{P} = -\nabla p$. Thus, (3.7) can be rewritten as,

$$mn\Big[\frac{\partial \vec{u}}{\partial t} + (\vec{u} \cdot \vec{\nabla})\vec{u}\Big] = qn\vec{E} - \nabla p. \tag{3.9}$$

(3.9) is in fact the momentum equation for a collisionless plasma system of ions and electrons. Given the plasma's quasi-neutral-steady behavior, the left hand side of (3.9) vanishes giving,

$$qn\vec{E} = \nabla p. \tag{3.10}$$

Now, according to thermodynamics, there is a mean thermal energy of $kT/2$ associated with each translational degree of freedom $(i = x, y, z)$ such that,

$$\frac{1}{2}kT_{\alpha i} = \frac{1}{2}m_\alpha < c_{\alpha i}^2 >, \tag{3.11}$$

where α denotes the relevant particle species, and k is Boltzmann's constant. Now, the scalar pressure p is defined as one-third the trace of the pressure tensor,

$$p_\alpha = \frac{1}{3}\sum_{i,j} \mathrm{P}_{\alpha ij}\delta_{ij} = \frac{1}{3}\sum_{i} \mathrm{P}_{\alpha ii} = \frac{1}{3}(\mathrm{P}_{\alpha xx} + \mathrm{P}_{\alpha yy} + \mathrm{P}_{\alpha zz}), \tag{3.12}$$

where δ_{ij} is the Kronecker delta, defined such that $\delta_{ij} = 1$ for $i = j$ and $\delta_{ij} = 0$ for $i \neq j$. The pressure tensor elements $P_{\alpha ii}$, with $i = x, y, z$, are the hydrostatic pressures *normal* to the surfaces described by $i = constant$ such that [11],

$$p_\alpha = \frac{1}{3}n_\alpha m_\alpha < c_\alpha^2 >, \tag{3.13}$$

where $c_\alpha^2 = c_{\alpha x}^2 + c_{\alpha y}^2 + c_{\alpha z}^2$. Since the distribution of random velocities in the plasma is assumed to be isotropic, we have $c_{\alpha x}^2 = c_{\alpha y}^2 = c_{\alpha z}^2 = c_\alpha^2/3$, and therefore,

$$p_\alpha = n_\alpha m_\alpha < c_{\alpha i}^2 > . \tag{3.14}$$

Combining (3.11) and (3.14) gives,

$$p_\alpha = n_\alpha kT_\alpha, \tag{3.15}$$

which is the equation of state of an ideal gas. Substituting (3.15) in (3.10) we get,

$$qn_\alpha\vec{E} = kT_\alpha\frac{\partial n_\alpha}{\partial\vec{r}}. \tag{3.16}$$

The plasma discharge is in the presence of a conservative force due to an electrostatic field as defined by (3.5). Such a system is characterized by a distribution function that differs from the Maxwell-Boltzmann distribution by an exponential factor known as the *Boltzmann factor*. Substituting, $\vec{E} = -\frac{\partial\phi}{\partial\vec{r}}$ for the electric field we get,

$$-q\frac{\partial\phi}{\partial\vec{r}} = \frac{kT_\alpha}{n_\alpha}\frac{\partial n_\alpha}{\partial\vec{r}}, \tag{3.17}$$

the solution of which is the Boltzmann relation [11],

$$n_\alpha(\vec{r}) = n_0 exp\Big(\frac{-q\phi(\vec{r})}{kT_\alpha}\Big), \tag{3.18}$$

where q is the charge of the particle, e for ions, and -e for electrons, while n_0 is the number density of the charged particles in the plasma, otherwise known as the *background plasma density*. The Boltzmann relation expresses the number density of charged particles as a function of the electric potential. The total electric charge density ρ_c can be expressed as,

$$\rho_c = -e(n_e(\vec{r}) - n_i(\vec{r})) = -en_0\Big[exp\Big(\frac{e\phi(\vec{r})}{kT_e}\Big) - exp\Big(\frac{-e\phi(\vec{r})}{kT_i}\Big)\Big], \tag{3.19}$$

where T_i and T_e are the ion and electron temperatures. Assuming that the perturbing electrostatic potential is weak so that the electrostatic potential energy is much less than the mean thermal energy,

$$e\phi(\vec{r}) << kT, \tag{3.20}$$

we can make the approximation using a power series expansion that,

$$exp\Big[\pm\frac{e\phi(\vec{r})}{kT_\alpha}\Big] \approx 1 \pm \frac{e\phi(\vec{r})}{kT_\alpha}, \tag{3.21}$$

leading to the simplification,

$$\rho_c = -e(n_e - n_i) \approx -en_0\Big(\frac{e\phi(\vec{r})}{kT_e} + \frac{e\phi(\vec{r})}{kT_i}\Big). \tag{3.22}$$

Therefore, substituting (3.22) into (3.6) we arrive at the fundamental equation that describes the electrostatic formulation of the plasma actuator flow problem,

$$\nabla(\epsilon_r \nabla\phi(\vec{r})) = \frac{\phi(\vec{r})}{\lambda_D^2}, \tag{3.23}$$

where λ_D is the Debye length, defined as,

$$\lambda_D = \Big[\frac{e^2 n_0}{\epsilon_0}\Big(\frac{1}{kT_i} + \frac{1}{kT_e}\Big)\Big]^{-\frac{1}{2}}. \tag{3.24}$$

As mentioned earlier, the Debye length is the characteristic distance over which the electric field influence of an individual charged particle can be felt by other particles in the system. In other words, free charges in the plasma are shielded from this electric *influence* to a distance given by the Debye length. Roth [4] states that for industrial plasmas the Debye length is approximately 0.00017 m, and the density of charged particles is about 10^{16} $particles/m^3$. Debye shielding is valid if there are enough particles in the charge cloud. The dimensionless parameter that characterizes this criteria is Λ which for unmagnetized plasma systems, is defined as,

$$\Lambda = \frac{4}{3}\pi\lambda_D^3 n_e. \tag{3.25}$$

If the plasma parameter $\Lambda >> 1$ it follows that the plasma is weakly-coupled and that Debye shielding is valid. Roth's values provide $\Lambda = 3.5 \times 10^5$, indicating the assumption that Debye shielding is valid.

A rough schematic of the computational domain for our problem is shown in Figure 3.1. The plasma actuator is configured in an asymmetric arrangement with one electrode exposed to air while the other is completely encapsulated in a dielectric material.The electrostatic equation (3.23) is solved throughout this domain. The boundary conditions on our domain are said to represent the condition at infinity, where the electric potential, ϕ, is set to zero,

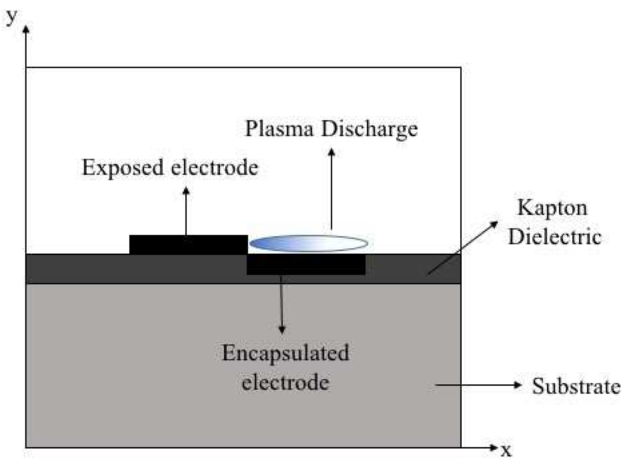

Figure 3.1: *Computational domain for the SDBD plasma actuator flow problem.*

$$\phi|_{Boundary} = 0. \tag{3.26}$$

However, the value of the electric potential on the electrodes is set to a constant,

$$\phi|_{Electrodes} = \pm\phi_0. \tag{3.27}$$

The lack of complex boundary conditions in the Orlov model will be discussed in detail during the analysis of the model's computational results. But for now, what is left is the solution for two fundamental values including the electric potential from (3.23) and the plasma body force. Using equations (3.6) and (3.23), the charge density ρ_c can be found as,

$$\nabla(\epsilon_r \nabla\phi(\vec{r})) = \frac{-\rho_c}{\epsilon_0} = \frac{\phi(\vec{r})}{\lambda_D^2}, \tag{3.28}$$

or,

$$\rho_c = -\frac{\epsilon_0}{\lambda_D^2}\phi(\vec{r}). \tag{3.29}$$

Due to the electric field in the plasma, in regions where there is a net charge density, a plasma body force exists. Using the Lorentz equation for electric force,

$$\vec{f}_b(\vec{r}) = q\vec{E}(\vec{r}), \tag{3.30}$$

the plasma body force for a given charge density ρ_c is,

$$\vec{f}_b(\vec{r}) = q\vec{E}(\vec{r}) = \rho_c\vec{E}(\vec{r}) = -\Big(\frac{\epsilon_0}{\lambda_D^2}\Big)\phi(\vec{r})\vec{E}(\vec{r}). \tag{3.31}$$

This body force is at the crux of the plasma actuator's macroscopic influence on the neutral continuum, and the subsequent modification of the flow's boundary layer. The plasma body force acts in the vector direction as that of the internal electric field in the plasma, and as such is directed from the exposed electrode to the dielectric surface or the encapsulated electrode. It is important to note that Orlov's model treats ions and electrons as a fluid background through the Boltzmann relation making it similar to a quasistatic approach to the plasma actuator flow problem.

3.3 Conclusion

This completes our discussion of Orlov's Electrostatic model used in this thesis. Orlov's model treats the electrons and ions, via the Boltzmann relation, as a fluid background. The following chapter will detail the collisionless Electrostatic Particle-In-Cell method formulated by the author to model the SDBD plasma actuator flow problem.

Chapter 4

Particle-in-Cell Model

4.1 Particle Models for Plasmas

Particle models have been highly successful in the simulation of plasmas, and involve tracking the motions of a large number of charged particles interacting via external and self-induced electromagnetic fields. These models are mainly limited by computational standards as even the most advanced computers can only follow the motion of a few million particles for a considerable amount of time. In comparison, laboratory and space plasmas typically have number densities of $10^{12}\ cm^{-3}$, and $10^{18}\ cm^{-3}$ [28].

Thus, in particle models, there are two predominant methods which are used in the representation of large numbers of particles. One can either view each particle in a simulation as a super-particle i.e. a particle which represents many particles or one may focus the computational domain such that the simulation can be viewed as modeling a very small region of the plasma. Various particle models have been used throughout history ranging from one-, two-, and three-dimensional models that are either electrostatic, magnetostatic, or electromagnetic in nature. In this thesis, we utilize a collisionless Electrostatic Particle-in-Cell (PIC) model.

4.2 Theoretical Overview

4.2.1 Introduction

In this thesis, we consider the behavior of charged particles in a low-density plasma. The modeling of plasmas is difficult due to the high number of charged particle interactions through external and self-induced electromagnetic fields, the presence of solid objects, and most importantly the differing time-scales of propagation for electrons and ions. Simplifying assumptions have to be made in order to make the PIC method computationally efficient, and suitable.

We begin by assuming that the plasma current is low enough such that self-induced magnetic fields can be ignored. Furthermore, unlike the Orlov model where both the ions and the electrons are modeled as a fluid background, the PIC model considers ions to be kinetic while the electrons are modeled as fluidic via the Boltzmann relationship. This is done so that the equations are time integrated over the larger ion time scale allowing for an increase in computational speed. Lastly, the plasma density is sufficiently low such that particle collisions can be neglected. The use of full dynamic ions along with massless or Boltzmann electrons defines the PIC model's hybrid approach.

Charged particles interact such that particles of opposite charge are attracted towards each other, while particles of like charge repel. This is classically described by Coulomb's law which states,

$$\vec{F} = \frac{1}{4\pi\epsilon_0}\frac{q_1 q_2}{r^2}\vec{r}_{12}, \tag{4.1}$$

where q_1 and q_2 represent the charges of the two particles, r is the distance between the two particles, and ϵ_0 is the vacuum permittivity constant. In plasma simulations, rather than computing the Coulomb force directly, the force acting on charged particles is given by the Lorentz Force,

$$\vec{F} = q(\vec{E} + \vec{v} \times \vec{B}), \tag{4.2}$$

where q is the particle charge, $\vec{E}$ is the electric field, $\vec{v}$ is the particle velocity, and $\vec{B}$ is the magnetic field. In the electrostatic case, the magnetic field term in the Lorentz force equation can be ignored. As mentioned earlier, it is exceedingly difficult to simulate every single charged particle and track their motions. Our method uses the approach where each computational particle is in fact a super-particle representing a large collection of particles. A *specific weight* is assigned to each particle, describing the ratio of real particle per super-particle.

4.2.2 Governing Equations

There are three main equations used in the PIC model to describe the fundamental particle processes in a plasma:

i. *Newton's Second Law* is used to dictate the motion of each super-particle, and is given by,

$$\vec{v} = \frac{d\vec{r}}{dt}, \tag{4.3}$$

$$\vec{F} = m\frac{d\vec{v}}{dt} = q\vec{E}, \tag{4.4}$$

where q is the particle charge, and m is the mass of the charged particle.

ii. *Poisson's equation* is solved for the electric field,

$$\nabla(\epsilon_r \nabla\phi(\vec{r})) = \frac{-\rho_c}{\epsilon_0}, \tag{4.5}$$

where $\phi(\vec{r})$ is the electric potential, ρ_c is the charge density, ϵ_0 is the vacuum permittivity, and ϵ_r is the dielectric constant of the media. $\vec{r} = (x, y)$ represents the notion that we are once again considering a two-dimensional system. The total electric charge density is defined as,

$$\rho_c = e(n_i(\vec{r}) - n_e(\vec{r})). \tag{4.6}$$

The plasma body force is calculated by substituting for the electric field and electric potential in (3.31).

iii. *Boltzmann's relation* is used to simplify the complications arising from the differing time-scales of propagation of ion, and electrons. Extremely small computational time steps are required if we are to observe the motion of electrons without the introduction of numerical errors, but this leaves the method unusable in studying large-scale problems. In the reference frame of an ion, the electrons move instantaneously. Thus, this PIC model defines electrons as a fluid,

$$n_e(\vec{r}) = n_0 exp\Big(\frac{e(\phi(\vec{r}) - \phi(0))}{kT_e}\Big), \tag{4.7}$$

and leaves the ions (positive) to be kinetic.

4.2.3 Solution Algorithm

The PIC model's solution algorithm consists of seven iterative steps [29],

i. *Compute, and distribute charge density*: Particles positions are distributed within the computational domain.

ii. *Compute the electric potential*: Solve Poisson's equation.

iii. *Compute the electric field*: Solve for the electric field using $\vec{E} = -\nabla\phi$.

iv. *Move the particles*: Update the positions, and velocities of particles using Newton's Second Law.

v. *Generate particles*: Sample sources for new particles.

vi. *Output results*: Save information on simulation state at preset time-steps.

vii. *Repeat*: Repeat the loop, iterating until either the maximum number of time-steps is achieved, the tolerance criterion is met, or the simulation reaches a steady state.

4.3 Conclusion

This completes our brief review on the theory of the PIC model. The PIC model treats the electrons as a fluid background via the Boltzmann relation, while the ions remain dynamic. This makes it a hybrid model compared to Orlov's fluid model where the ions and electrons are both modeled as a fluid background. The following chapter will discuss how these two models are numerically implemented.

Chapter 5

Applying the Orlov and PIC Models

5.1 Overview

Having reviewed the theory behind the Orlov and PIC models, this chapter will discuss how this knowledge is applied in a computational framework. To begin with, the Orlov and PIC model solvers were both implemented using MATLAB software. Two-dimensional cellular grids with discrete cell widths (input by the user) were utilized as computational domains. Finite-difference schemes were used to discretize the relevant equations in the two models meaning the computational iterations largely involved the manipulation of matrices that quantified the various parameters in the two methods over iterative procedures. The MATLAB codes for both models have been included in the Appendices.

5.2 Orlov's Original Framework

The SDBD plasma actuator configuration consists of two electrodes in an asymmetric arrangement with one exposed to the airflow, and the other encapsulated in a dielectric medium. It has been proven via several experiments [4; 5; 8] that the plasma discharge appears and exists only above the encapsulated electrode. In fact, the plasma extent can be modeled to die off linearly away from the encapsulated electrode [10].

Orlov modeled the SDBD plasma actuator flow problem by solving the electrostatic equation (3.23) over a 201 × 201 square grid domain. The electrodes were provided with normalized potential values of,

$$\begin{aligned} \phi|_{ExposedElectrode} &= 1.0, \\ \phi|_{EncapsulatedElectrode} &= -1.0. \end{aligned} \tag{5.1}$$

All four boundaries of the square domain were assigned electric potential values of zero,

$$\phi|_{Boundaries} = 0. \tag{5.2}$$

The encapsulated electrode was set within a 3×10^{-3} inches thick dielectric layer of Kapton at the center of the domain. A Debye length value of 0.001 inches (25.4 μm) was assumed for the characteristic plasmas being considered [4]. Relative dielectric permittivity constants for air, and the Kapton layer were used to differentiate the two environments:

$$\begin{aligned} \epsilon_{r,air} &= 1.0, \\ \epsilon_{r,kapton} &= 2.7. \end{aligned} \tag{5.3}$$

Orlov then partitioned the domain as illustrated in Figure 5.1. The electrostatic equation has a non-zero charge term, ρ_c, on the right hand side (3.6), for the region right above the encapsulated electrode. Meanwhile, in all other sub-regions of the computational domain, the electrostatic equation is modeled with zero charge density, such that it takes the form of Laplace's equation,

$$\nabla(\epsilon_r \nabla\phi) = 0. \tag{5.4}$$

Orlov resolved the electric field in the high charge density region of the plasma

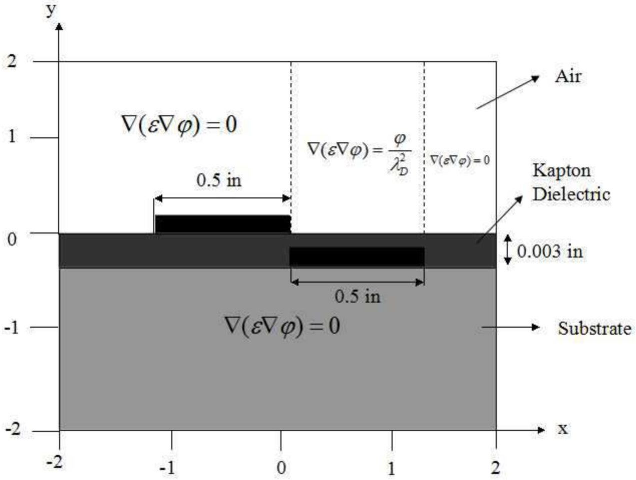

Figure 5.1: *Solving the electrostatic equation in the computational domain (not to scale) of the SDBD plasma actuator.*

formation near the dielectric surface above the encapsulated electrode. It is noted that the length of this region of high charge density is primarily determined by the Debye length. The smaller the Debye length, the narrower the region. Using Robert's stretching formulation [30], Orlov configured the domain into a non-uniform grid such that the grid lines clustered near the inner edge of the electrodes- to resolve the plasma body force coupled to the neutral air- while becoming coarser in the distance, and using the Gauss-Seidel procedure to solve the electrostatic equation accordingly. The convergence criterion for the iterative algorithm was defined by an error parameter of the maximum absolute difference in the electric potential between two consecutive iterative steps,

$$ERR = max(|\phi_{i,j}^{n+1} - \phi_{i,j}^{n}|). \tag{5.5}$$

Convergence was achieved if ERR is less than 10^{-10}. This particular value was chosen for sufficient accuracy in the results of the plasma body force calculations. However, various facets of the Orlov model have been modified to accommodate for the objectives of this thesis:

i. Orlov solved the Navier-Stokes equations involving the stream and vorticity functions, in tandem with Maxwell's equations, providing for a more detailed analysis of the flow problem. This is not utilized here, as this thesis focuses mainly on the plasma dynamics and electrostatics of the problem.

ii. Unlike the non-uniform grid (via Robert's stretching formulation) used to resolve the electric field and body force, this work utilizes a uniform grid. This largely simplified the original electrostatic equations as presented in Orlov's dissertation [1].

iii. The base set-up used in this thesis for the Orlov model follows the configuration presented in Figure 5.1 with the exception that the electrostatic equation is not partitioned accordingly but solved over the entire domain with a non-zero charge density.

We will now detail the numerical formulation of Orlov's electrostatic model as utilized in this thesis.

5.3 Numerical Formulation of Orlov's Model

The governing electrostatic equation of the Orlov model is solved over the computational domain, which is discretized into a two dimensional uniform cellular grid. Along with the corresponding boundary conditions on the electrodes, and the domain, the equations are discretized using the standard centered second order scheme. We begin by expanding equation (3.23) as

$$\epsilon_r \nabla^2 \phi(\vec{r}) + \nabla \epsilon_r \cdot \nabla \phi(\vec{r}) = \frac{1}{\lambda_D^2} \phi(\vec{r}). \tag{5.6}$$

The gradient operator is defined as,

$$\vec{\nabla} = \frac{\partial}{\partial x} \hat{i} + \frac{\partial}{\partial y} \hat{j}, \tag{5.7}$$

which gives the following,

$$\epsilon_r \frac{\partial^2 \phi}{\partial x^2} + \epsilon_r \frac{\partial^2 \phi}{\partial y^2} + \frac{\partial \epsilon_r}{\partial x} \frac{\partial \phi}{\partial x} + \frac{\partial \epsilon_r}{\partial y} \frac{\partial \phi}{\partial y} = \frac{\phi}{\lambda_D^2}. \tag{5.8}$$

Using centered-difference approximations for the first, and second derivatives,

$$
\begin{aligned}
\frac{\partial \phi}{\partial x} &= \frac{\phi_{i,j+1} - \phi_{i,j-1}}{2\Delta x}, \\
\frac{\partial \phi}{\partial y} &= \frac{\phi_{i+1,j} - \phi_{i-1,j}}{2\Delta y}, \\
\frac{\partial^2 \phi}{\partial x^2} &= \frac{\phi_{i,j+1} - 2\phi_{i,j} + \phi_{i,j-1}}{\Delta x^2}, \\
\frac{\partial^2 \phi}{\partial y^2} &= \frac{\phi_{i+1,j} - 2\phi_{i,j} + \phi_{i-1,j}}{\Delta y^2},
\end{aligned}
\tag{5.9}
$$

this results in a final equation of the form,

$$
A_{i+1,j}\phi_{i+1,j} + B_{i-1,j}\phi_{i-1,j} + C_{i,j+1}\phi i, j+1 + D_{i,j-1}\phi i, j-1 = E_{i,j}\phi_{i,j}, \tag{5.10}
$$

where the numerical coefficients A, B, C, D, and E can be computed at every node of the computational grid before the iteration procedure:

$$
\begin{aligned}
A(i,j) &= \frac{\epsilon_{r(i,j)}}{\Delta y^2} + \frac{\epsilon_{r(i+1,j)}}{(2\Delta y)^2} - \frac{\epsilon_{r(i-1,j)}}{(2\Delta y)^2}, \\
B(i,j) &= \frac{\epsilon_{r(i,j)}}{\Delta y^2} + \frac{\epsilon_{r(i-1,j)}}{(2\Delta y)^2} - \frac{\epsilon_{r(i+1,j)}}{(2\Delta y)^2}, \\
C(i,j) &= \frac{\epsilon_{r(i,j)}}{\Delta x^2} + \frac{\epsilon_{r(i,j+1)}}{(2\Delta x)^2} - \frac{\epsilon_{r(i,j-1)}}{(2\Delta x)^2}, \\
D(i,j) &= \frac{\epsilon_{r(i,j)}}{\Delta x^2} + \frac{\epsilon_{r(i,j-1)}}{(2\Delta x)^2} - \frac{\epsilon_{r(i,j+1)}}{(2\Delta x)^2}, \\
E(i,j) &= \frac{2\epsilon_{r(i,j)}}{\Delta x^2} + \frac{2\epsilon_{r(i,j)}}{\Delta y^2}.
\end{aligned}
\tag{5.11}
$$

This system of equations, along with the boundary conditions stated earlier is then solved using the standard Gauss-Seidel procedure for the electric potential. Using Poisson's equation, the electric field values at every point of the domain can also be computed,

$$
\vec{E} = -\frac{\phi_{i,j+1} - \phi_{i,j-1}}{2\Delta x} - \frac{\phi_{i+1,j} - \phi_{i-1,j}}{2\Delta y}. \tag{5.12}
$$

The electric field and electric potential can then be substituted accordingly into (3.31) allowing the plasma body force vector to be computed over the domain. Note that we have maintained the same boundary conditions as utilized by Orlov in his original formation where the potential is set to zero at the four corners of the square domain. The upper electrode, and lower electrode are also set with normalized potentials of ± 1. On the other hand, relevant parameters such as the grid resolution, relative permittivities, and Debye lengths will be modified through the course of our evaluations. The schematics, and relevant details as such will be discussed in great detail in the following chapter where we will address our numerical results.

5.4 Numerical Formulation of the PIC Model

In the previous chapter, we summarized the various steps that contribute to the PIC solution algorithm ranging from the distribution of the charge density to the generation of particles. Let us look into each individual step with further detail and how we apply the PIC method to model the SDBD plasma actuator flow problem.

5.4.1 Computing the Charge Density

The computational domain is in essence a two-dimensional mathematical grid used to measure charge, and if necessary, current densities. It is from the charge density that one is subsequently able to calculate and obtain values for the electric, and magnetic fields on the grid. The spatial grid, used for obtaining the field from the charge density has grid points,

$$\begin{aligned} x_i &= i\Delta x, \\ y_j &= j\Delta y. \end{aligned} \tag{5.13}$$

The charge density on the grid is defined as the number of charge units per unit volume. In other words, each cell is attributed with an infinitesimal charge

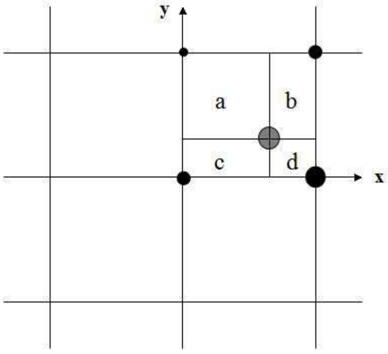

Figure 5.2: *Charge density weighting.*

density; the charge of all particles are distributed onto the nodes of each cell, from which the charge density at each cell is computed by dividing by the corresponding nodal volume. This distribution of particle charge among the nodes of a cell the particle occupies adheres to the name of the method, *Particle-In-Cell.*

A first-order linear scatter operation is used for the distribution of the charges along the nodes, and is schematically shown in Figure 5.2. Super-particles are used to represent a large number of particles, a property defined by their *specific weights.* Therefore, the total charge carried by each super-particle is offset by a value, *specific weight*$\times q$. The weight factors [29] for the four area fractions presented in Figure 5.2 are,

$$\begin{aligned} w_a &= (h_x)(1-h_y), \\ w_b &= (1-h_x)(1-h_y), \\ w_c &= (h_x)(h_y), \\ w_d &= (h_y)(1-h_x), \end{aligned} \tag{5.14}$$

where,

$$h_x = \frac{x}{\Delta x}, \tag{5.15}$$

$$h_y = \frac{y}{\Delta y},$$

represent the fractional distance of the particle from the cell origin (at the center) in the x-, and y-directions. Nodal volumes are defined by the product of the cell's dimensions, $\Delta x \Delta y$. The weights are all multiplied by the charge density uniformly filling each cell (q/cell area). The charge densities at all grid points then are included in the solution of Poisson's equation. Domain boundaries and edges do result in exceptions in computing charge distributions within cells, requiring complicated boundary conditions. The corresponding boundary conditions utilized for the model in this work also play a major role in the determination of the electric potential.

5.4.2 Computing the Electric Potential

The electric potential is solved for using Equation (3.23) that can be expanded as,

$$\epsilon_r \frac{\partial^2 \phi}{\partial x^2} + \epsilon_r \frac{\partial^2 \phi}{\partial y^2} + \frac{\partial \epsilon_r}{\partial x}\frac{\partial \phi}{\partial x} + \frac{\partial \epsilon_r}{\partial y}\frac{\partial \phi}{\partial y} = -\frac{e}{\epsilon_0}\Big[n_i - n_0 exp\Big(\frac{e(\phi - \phi_0)}{kT_e}\Big)\Big]. \tag{5.16}$$

Using centered-difference approximations for the first, and second derivatives,

$$\begin{aligned} \frac{\partial \phi}{\partial y} &= \frac{\phi_{i,j+1} - \phi_{i,j-1}}{2\Delta y}, \\ \frac{\partial \phi}{\partial x} &= \frac{\phi_{i+1,j} - \phi_{i-1,j}}{2\Delta x}, \\ \frac{\partial^2 \phi}{\partial y^2} &= \frac{\phi_{i,j+1} - 2\phi_{i,j} + \phi_{i,j-1}}{\Delta y^2}, \\ \frac{\partial^2 \phi}{\partial x^2} &= \frac{\phi_{i+1,j} - 2\phi_{i,j} + \phi_{i-1,j}}{\Delta x^2}, \end{aligned} \tag{5.17}$$

resulting in a final equation of the form,

(5.18)

$$A_{i+1,j}\phi_{i+1,j} + B_{i-1,j}\phi_{i-1,j} + C_{i,j+1}\phi_{i,j+1} + D_{i,j-1}\phi_{i,j-1} + E_{i,j}\phi_{i,j} \\ = -\frac{e}{\epsilon_0}\Big[n_i - n_0 exp\Big(\frac{e(\phi-\phi_0)}{kT_e}\Big)\Big]. \tag{5.19}$$

The numerical coefficients A, B, C, D, and E can be computed at every node of the computational grid before the iteration procedure:

$$\begin{aligned} A(i,j) &= \frac{\epsilon_{r(i,j)}}{\Delta x^2} + \frac{\epsilon_{r(i+1,j)}}{(2\Delta x)^2} - \frac{\epsilon_{r(i-1,j)}}{(2\Delta x)^2}, \\ B(i,j) &= \frac{\epsilon_{r(i,j)}}{\Delta x^2} + \frac{\epsilon_{r(i-1,j)}}{(2\Delta x)^2} - \frac{\epsilon_{r(i+1,j)}}{(2\Delta x)^2}, \\ C(i,j) &= \frac{\epsilon_{r(i,j)}}{\Delta y^2} + \frac{\epsilon_{r(i,j+1)}}{(2\Delta y)^2} - \frac{\epsilon_{r(i,j-1)}}{(2\Delta y)^2}, \\ D(i,j) &= \frac{\epsilon_{r(i,j)}}{\Delta y^2} + \frac{\epsilon_{r(i,j-1)}}{(2\Delta y)^2} - \frac{\epsilon_{r(i,j+1)}}{(2\Delta y)^2}, \\ E(i,j) &= -\frac{2\epsilon_{r(i,j)}}{\Delta x^2} - \frac{2\epsilon_{r(i,j)}}{\Delta y^2}. \end{aligned} \tag{5.20}$$

Note, the Boltzmann relation has been substituted on the right hand side of (5.20) for the electron charge density. Now, Poisson's equation is an elliptic equation, which is a boundary-value problem. Two types of boundaries exist: Dirichlet, and Neumann. Dirichlet boundary conditions specify the electric potential values along the boundary of the computational domain. Neumann boundary conditions specify the values of the electric field, the derivative of the electric potential, along the boundary of the computational domain. The specifications for the boundary conditions is varied throughout our use of the PIC model, and will be analyzed in further detail in the following chapter. The solution for the electric potential is achieved by transposing (5.16) into matrix form,

$$Ax = b, \tag{5.21}$$

where A represents the multiplication matrix for the potential solver containing the coefficients of the left hand side of the equation, while b is the multiplication matrix for the right hand side of the same equation expressing the difference in ion and electron charge densities. x is the electrostatic potential, the solution we seek. Using an iterative method, one obtains a sequence of approximations to this solution,

$$x^k, k = 0, 1, 2, ..., \tag{5.22}$$

such that $(b - Ax^k) \rightarrow 0$ as $k \rightarrow \infty$. The superscript k is an iteration counter. The condition for convergence with this iterative method is defined such that the iterations continue until,

$$\frac{\|r^k\|}{\|b\|} < \epsilon. \tag{5.23}$$

r^k refers to the residual of the k^{th} iteration,

$$r^k = b - Ax^k. \tag{5.24}$$

ϵ is a specified tolerance, and is typically between $5 \times 10^{-3} > \epsilon > 1 \times 10^{-6}$ [31], but can vary depending on the problem under question. This is the method used to solve for the electric potential in the PIC model.

5.4.3 Computing the Electric Field

The electric field is computed over the two dimensions as,

$$\begin{aligned} E_{x,i} &= -\frac{\phi_{i+1,j} - \phi_{i-1,j}}{2\Delta x}, \\ E_{y,j} &= -\frac{\phi_{i,j+1} - \phi_{i,j-1}}{2\Delta y}. \end{aligned} \tag{5.25}$$

The plasma body force is calculated by substituting for the electric field and electric potential in (3.31).

5.4.4 Moving the Particles

Particle positions, and velocities are updated using the classical Leapfrog method (Figure 5.3). Firstly, the particle velocities are integrated through the time-step Δt following which the particle positions are updated. The two quantities are

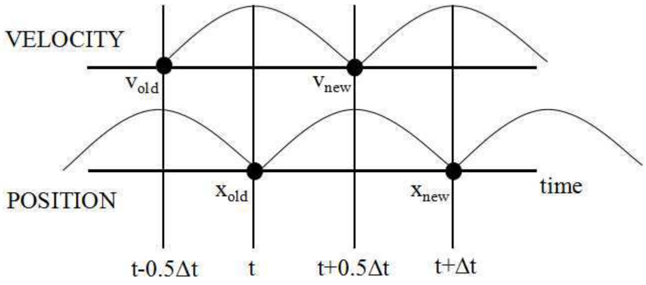

Figure 5.3: *Leap-Frog integration method*

offset from each other by half a time-step as prescribed by the Leapfrog method. The fundamental equations of this method are,

$$\begin{aligned} \vec{v}^{k+0.5} &= \vec{v}^{k-0.5} + \frac{q}{m}\vec{E}\Delta t, \\ \vec{x}^{k+1} &= \vec{x}^{k} + \vec{v}^{k+0.5}\Delta t. \end{aligned} \tag{5.26}$$

Using a *gather* operation, the electric field at the position of each particle can be computed with the corresponding specific weights, in a manner inversely analogous to the computation of charge densities. After the particles have been updated, it is important to make sure that the particles are within the computational domain. Two particular interactions are made possible, namely that particles can either exit the domain, be reflected, or collide with solid objects. Thus, there are two further cases of computational boundaries presented in the model: *absorbing*, and *reflective*. Details of such interactions will be considered in the following chapter.

5.4.5 Generating New Particles

New particles are generated by sampling sources [29]. This is quite specific to the problem that is considered, but in general, the simulation begins by loading all the particles, following which it computes their final distribution state through its progress. In this work, the particle generator is sampled using the Maxwellian Distribution. As given in Birdsall [29], this is approximated as,

$$v_M = v_t \left(\frac{M}{12}\right)^{-\frac{1}{2}} \left[\sum_{i=1}^{M} R_i - \frac{M}{2}\right]. \tag{5.27}$$

Here, M is an integer, and R_i is an i-th random number in the range [0:1). v_t is the thermal velocity. The respective value for M controls the accuracy of the model. Birdsall [29] uses M=12 to prevent entries larger than six times the thermal velocity. This work uses M=3. The method basically works directly with a uniform set of random numbers $R_1, R_2, ..., R_M$ between 0 and 1, generating a random normal distribution. So we begin with the expression,

$$\sum_{i=1}^{M} \left(R_i - \frac{1}{2}\right), \tag{5.28}$$

where we are basically adding a series of random numbers distributed uniformly between the range -0.5 and 0.5 such that they have a mean of 0. In the limit of taking an infinite number of such random deviates, we can, according to the Central Limit Theorem, obtain a Maxwellian distribution. In probability theory, the Central Limit Theorem states that under certain conditions, the arithmetic mean of a large number of iterations of independent random numbers, each with a unique and well-defined expected value and finite variance, will be normally distributed, no matter what the underlying distribution may be.

The fundamental idea is that since the R_i are assumed to be statistically independent, the average of the products of such random numbers is the same as the product of the averages leading to us finding the variance (which is the square of the standard deviation) of (5.28) for M such values to be M/12. Now, the standard deviation of (5.28) if I were to add M such numbers would be $\left(\frac{M}{12}\right)^{\frac{1}{2}}$. In order to produce a Maxwellian, we basically take (5.28) and multiply it by $\left(\frac{M}{12}\right)^{-\frac{1}{2}}$ to provide us a standard deviation of 1. Multiplying this final product with the thermal velocity as seen in (5.27) provides us a Maxwellian distribution.

5.4.6 Outputting Results, and Loop Repetition

During each iteration, a set criteria of results pertaining to various geometric, and physical properties of our system will be output for display, and analysis. The main body of the PIC algorithm is computed over a set series of iterations. In each individual iteration, the five previous steps are repeated. This loop/algorithm continues until a certain convergence criterion is satisfied or a tolerance level is met.

5.5 Conclusion

This brings to an end our discussion on the numerical implementations of the two models. We will now begin our analysis of the various results procured in modeling the SDBD plasma actuator with these two models.

Chapter 6

Modeling Results, and Analyses

6.1 Introduction

We will now present the results pertaining to the Orlov and PIC models in analyzing the SDBD plasma actuator flow problem. Results from the Orlov model will largely be utilized as a referential bookmark while being compared regularly with those from the PIC model. This approach will help generalize the utilization of both methods, and evaluate their validity as fluid and hybrid models for the SDBD plasma actuator.

Table 6.1: *Orlov Model Parameters*

Variable	**Description**
Nx, Ny	Number of nodes in $\hat{x}$, and $\hat{y}$
Lx, Ly	Domain length in $\hat{x}$, and $\hat{y}$
dx, dy	Domain discretization in $\hat{x}$, and $\hat{y}$
λ_D	Debye length
Err	Iteration error
Tol	Convergence criterion

Tables 6.1-6.2 list the main parameters in the Orlov and PIC models. Three specific parameters including the electric potential, electric field, and the plasma

Table 6.2: *PIC Model Parameters*

Variable	**Description**
ϵ_0	Vacuum permittivity constant
q_e	Elementary charge
k_B	Boltzmann's constant
amu	Atomic mass unit
M	Ion mass
n_0	Initial number density
T_e	Electron temperature
T_i	Ion temperature
v_{Drift}	Drift/Particle injection velocity
λ_D	Debye length
$v_{Thermal}$	Thermal velocity
Nx, Ny	Number of nodes
ts	Total number of time-steps
dcell	Cell size
np_insert	Number of particles per cell
dt	Discretization of time-steps
Lx, Ly	Domain length in $\hat{x}, and\hat{y}$
ω_{pi}	Ion plasma frequency
flux	Flux of entering particles
npt	Number of real particles created per time-step
spwt	Specific weight
mp_q	Macro-particle charge
$max_{particles}$	Maximum particle buffer

body force will be analyzed in every simulation. As shown in Figure 3.1, we expect the plasma discharge to exist on the dielectric surface directly above the encapsulated surface, and decreasing in its extent away from the encapsulated electrode. Thus, it is natural to also presume that the highest magnitudes for the electric field and body force will be found by the inner edge between the two electrodes. As reviewed earlier, we also expect the electric field vector to be directed from the dielectric surface to the exposed electrode, and the plasma body force vector to be directed in the opposite direction from the exposed electrode to the dielectric surface.

Let us begin by first examining the benchmark cases utilized for the two models.

6.2 Orlov and PIC - Benchmark Cases

The relevant parameters utilized in the benchmark cases for the two models are summarized as follows:

i. The physical area of the square computational domain is 34.225 mm^2 (25 × 25 cells).

ii. The length and width of each cell in the grid is equivalent to a Debye length (λ_D) of 7.4 mm.

iii. The thicknesses of the electrodes and the dielectric layer are equivalent to a cell width (7.4 mm). The electrode widths are set to 59.2 mm (8 cells).

iv. A Kapton dielectric is the dielectric layer of choice.

v. A particle density of 10^{12} $particles/m^3$ is assumed along with an electron temperature (T_e) of 1 eV and an ion temperature (T_i) of 0.1 eV. (Only applicable to the PIC model.)

vi. A particle injection velocity of 70000 m/s is utilized. (Only applicable to the PIC model.)

The boundary conditions in the benchmark Orlov model are such that the exposed electrode has a fixed potential of 1 V, and the encapsulated electrode has a fixed potential of -1 V. The electric potential is initialized to zero at the boundaries and everywhere else throughout the computational grid. Following the algorithm provided in the previous chapter, and assuming a uniform grid division, the electrostatic equation is solved iteratively using the Gauss-Seidel procedure over the computational domain. The solver tolerance is set to a value of 0.1 (equivalent to that in the benchmark PIC model). Convergence is achieved if the error calculated in the differences of electric potential between consecutive iterations is less than this value. Using (3.31), the body force is calculated throughout the entire computational domain.

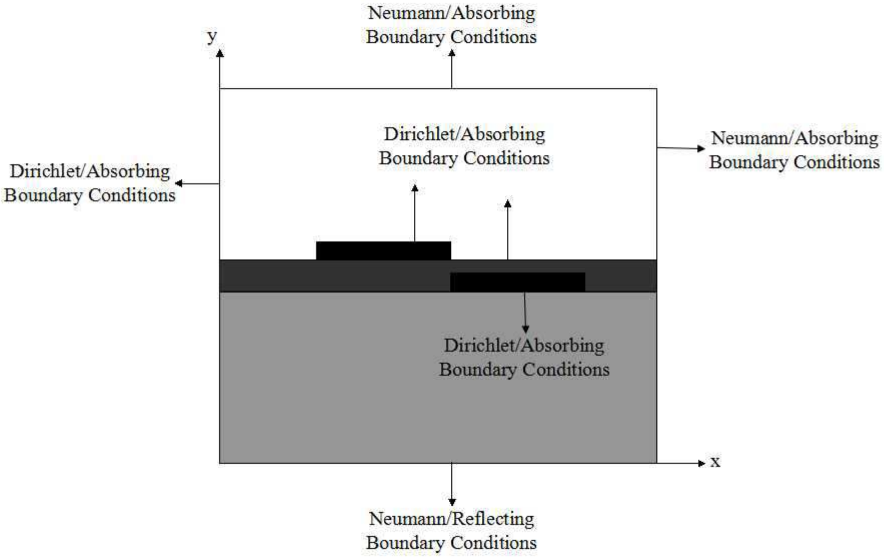

Figure 6.1: *Boundary conditions on the computational domain for the benchmark case of the PIC model.*

Similarly, Figure 6.1 presents a schematic involving the boundary conditions utilized in the benchmark PIC model. Particles travel from the left hand side of the domain, and exit out the right hand side, replicating an airflow over the SDBD plasma actuator configuration. Ions are modeled to be kinetic, while the electrons are a fluid background. Thus, it is the ion motion that is described in the flow of the particles.

The exposed electrode is set to an electric potential of 1 V and the encapsulated electrode is set to an electric potential of -1 V. A total of 400 iterations is used for the simulation with time-steps of $\Delta t \approx 1.06 \times 10^{-8}\ s$. At the beginning of each simulation, a preliminary check is made to ensure that the parameters maintain, and follow the stability criterion for a plasma that $\omega_{pi}\Delta t < 1$. About 375 particles are inserted per cell with a maximum particle buffer of 50000 particles. This can be modified if necessary. A tolerance of 0.1 is set for the electric potential solver.

The PIC model outnumbers the Orlov model in the number of parameters it uses to characterize the problem. This is essential, and greatly contributes to the PIC model's scope of detail in analyzing the plasma actuator, and the types of

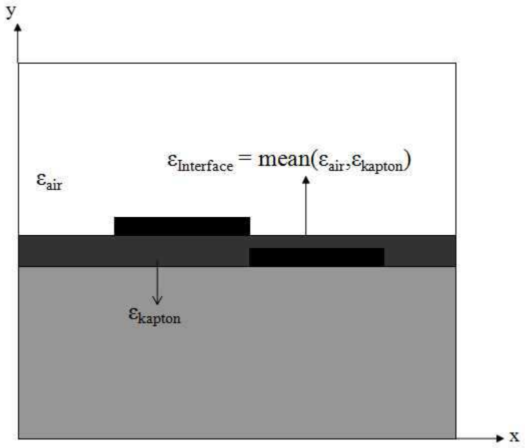

Figure 6.2: *Determination of dielectric constants over the computational domain.*

results obtained. Furthermore, a variety of boundary conditions have also been used between the two models. In that vein, Orlov's model is indeed highly simplified. The primary boundary condition is that the electric potential is set to zero at the domain boundaries. On the other hand, the default PIC model includes a combination of Dirichlet, and Neumann boundary conditions used in the calculation of the elliptic Poisson's equation (5.16) among the internal nodes of the domain. This is further supplemented by a mix of absorbing, and reflecting boundary conditions at the domain boundaries, electrodes, and dielectric surface.

In both models, the electrodes have the same dielectric constant or relative permittivity (ϵ_r) as the surrounding medium they are exposed to i.e. Last but not least, in order to characterize the different environments the system is exposed to, we assume that the electrodes have the same relative permittivity or dielectric constant as the surrounding medium they are exposed to i.e. the upper electrode has the dielectric constant of air (ϵ_{air}=1.0), and the encapsulated electrode has the dielectric constant of the dielectric in which it is buried. At the interface between the dielectric medium, and air, a mean value of the corresponding dielectric constants are assumed, as shown in Figure 6.2. Thus, at the interface between the Kapton dielectric medium, and air, $\epsilon_{Interface} = mean(\epsilon_{Kapton} + \epsilon_{Air}) = 1.85$.

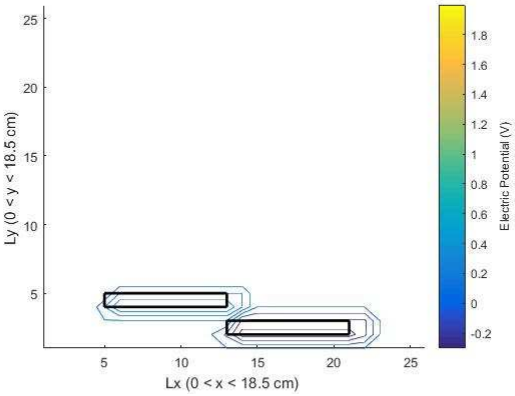

Figure 6.3: *Electric potential contours for the benchmark Orlov simulation.*

This concludes our discussion on the main parameters involved in the two models. Working knowledge of these parameters is important in order to formulate valid comparisons of results. Figures for the electric potential, electric field, and plasma body force values will be presented when appropriate. The x-, and y-axis on the figures correspond to the nodal coordinates. A colorbar will also be provided to identify with field magnitudes.

6.2.1 Orlov Benchmark Case - Analysis

A view of the contours of constant electric potential is shown in Figure 6.3. The structure of the potential field is such that they are densely collected about the electrode surface, and their inner edges, while decaying off rapidly in space away from the structure. The lines circle around the electrodes, with lines of higher electric potential clustered about the upper electrode (0.0937 V to 0.4000 V), and lines of lower electric potential clustered around the encapsulated electrode (-0.1208 V to -0.3496 V).

The electric field structure corresponding to the electric potential contours is shown in Figure 6.4. The magnitude of the electric field is highest about the inner edge between the two electrodes at ≈ 60 N/C, with consistently high values about the dielectric surfaces, and decaying at greater distances. This can be attributed to the gradients in electric potential resulting in a strong electric

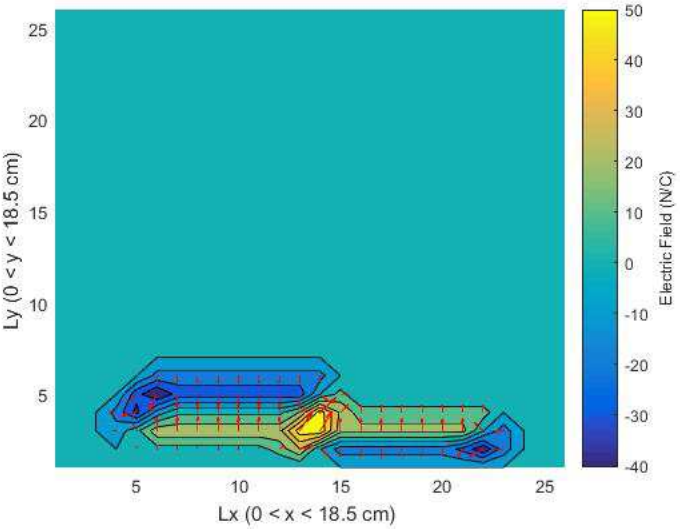

Figure 6.4: *Electric field contours overlaid with corresponding vector plot for the benchmark Orlov simulation.*

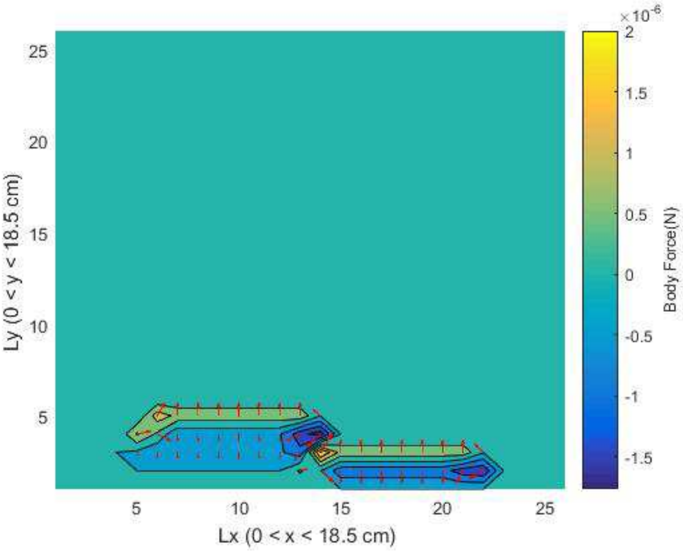

Figure 6.5: *Body force field overlaid with corresponding vector plot for the benchmark Orlov simulation.*

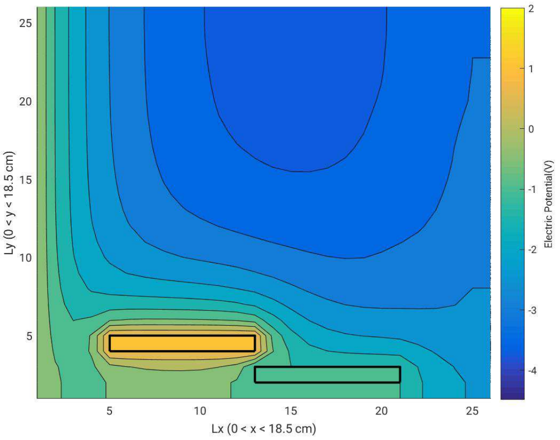

Figure 6.6: *Electric potential contours for the benchmark PIC simulation.*

field at this selective location. The electric field is directed from the encapsulated electrode to the upper electrode matching our earlier expectations.

The body force calculated from the electric field is presented in Figure 6.5. This is a volumetric body force, and exists only where free charges are present in the air. The body force is concentrated at the inner edge between the two electrodes, and is mainly distributed along the dielectric surfaces with a maximum value of $\approx 2.05 \times 10^{-6} N$. Elsewhere about the domain, the body force is essentially zero. Momentum addition to the airflow by way of this body force allows for the modification of the airflow. The body force is directed downward toward the dielectric surface as expected. The injection of the body force along the dielectric layer is also observable.

6.2.2 PIC Benchmark Case - Analysis

The basic characteristics presented in the results of the benchmark Orlov simulation follow suit in the results procured from the benchmark PIC simulation. The electric potential contour field is presented in Figure 6.6.

While the PIC model allows for greater detail in its analysis, the results find common grounds with those obtained from Orlov's model. The structure of the

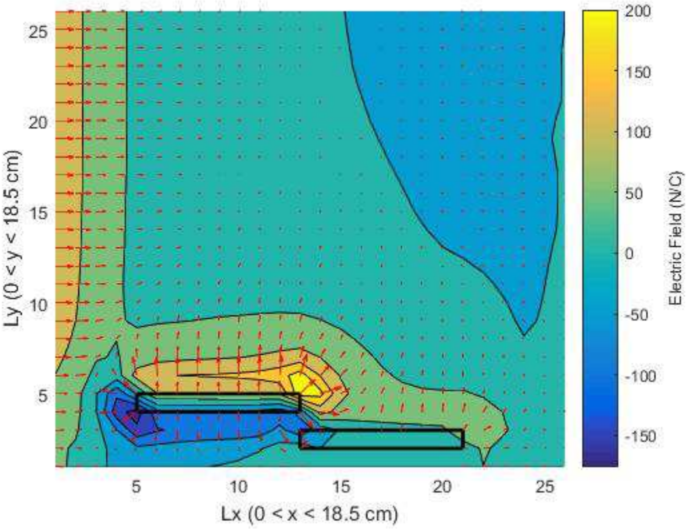

Figure 6.7: *Electric field overlaid with corresponding vector plot for the benchmark PIC model.*

potential field is such that the contour lines are once again densely collected about the exposed electrode surface, and the inner edges between the two electrodes, while decaying off rapidly in space away from the structure. The color field also displays the fact that there is a greater electric potential distribution about the exposed electrode compared to the encapsulated electrode. The exposed electrode is maintained at a positive potential of 1 V, and the encapsulated electrode is maintained at a negative potential of -1 V. The behavior is such that the electric potential decays the further one moves away from either electrode, sinking towards smaller and negative potential values as is evident in the color field.

The electric field structure is shown in Figure 6.7. The magnitude of the electric field is highest about the inner edge between the two electrodes, registering a maximum value of $\approx 230\ N/C$. Here too, the gradients in electric potential have resulted in a strong electric field close to the electrodes surface, directed from the encapsulated electrode to the upper electrode. Once again there is a remarkable similarity to the results from Orlov's model.

Similarly, we find that the body force magnitudes along the dielectric surface

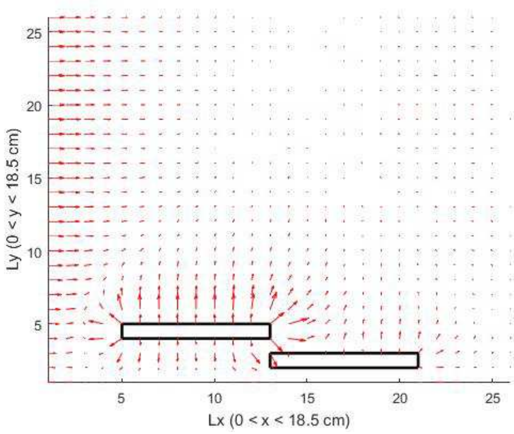

Figure 6.8: *Body force field overlaid with corresponding vector plot for the benchmark PIC simulation.*

range from a minimum $1.22 \times 10^{-4} N$ by the edge of the encapsulated electrode to a maximum of 0.0010 N closer to the inner edge by the exposed electrode. In particular, the structure of the body force field is reminiscent of a modified flow about an activated plasma actuator when one graphs the vector fields for the body forces of the individual particles (Figure 6.8).

6.2.3 Further comparisons

So far, this chapter describes the basic premise of the thesis to compare the PIC and Orlov algorithms, and evaluate their efficiency in modeling the plasma actuator. Results involving the electric potential, electric field, and the plasma body force were presented for the benchmark cases of each model. But, despite the qualitative agreements in the results between the two models there is quite a discrepancy in the numerical results. The Orlov model produces a maximum electric field magnitude of 60 N/C compared to the PIC's 230 N/C. Similarly, the Orlov model results with a maximum body force magnitude of $\approx 2.05 \times 10^{-6} N$ compared to the PIC's 0.0010 N. Furthermore, the two models are divisive in the degree of detail relegated upon their results. It is essential that these differing aspects of the two models be considered in detail, and in order to do so, the effects of further parametric variations are explored:

i. Modifying the computational domain, we made two simulations of the Orlov model with the use of a 50 × 50, and a 201 × 201 grid. All other parameters including the Debye length and the solver tolerance are set equivalent to those used in the benchmark model with corresponding values of 0.0074 m and 0.1. Having maintained the choice of a Kapton dielectric layer, and equivalent values for the Debye length and the convergence criterion, the main difference is elicited in the the physical lengths of the domains. For the 25 × 25 grid used in the benchmark case the domain length (x- and y-axes) was 0.1859 m, for the 50 × 50 grid it is 0.3700 m, and for the 201 × 201 grid it is 1.4874 m. But, neither of these differences in grid resolutions or physical domain lengths proved influential as the contour structures and the corresponding maxima of the electric potential, the electric field, and the plasma body force were identical to the results found in the benchmark simulation.

ii. Using the 201 × 201 grid resolution, a series of simulations were run with varying Debye length values, ranging from 0.0074 m (as in the benchmark simulation) to 35.4 μm, and smaller. Tables 6.3-6.5 present the corresponding values for the electric potential, electric field, and body force found in each case, at the inner edge between the two electrodes,

Table 6.3: *Electric field magnitudes for varying Debye Lengths*

Debye Length (m)	**Electric Field** (N/C)
0.010	2512.3
0.0074	2512.1
0.0000354	484.8970
0.0000254	278.3433
0.0000154	110.9881
0.000001	0.4924

A few generalized observations can be made from these tables. Beginning with Tables 6.3-6.4 we see that the magnitudes of the electric field, and the electric potential decrease as the Debye length decreases. On the other

Table 6.4: *Electric potential magnitudes for varying Debye lengths*

Debye Length (m)	**Electric Potential** (V)
0.010	0.1064 to 0.5,-0.25 to -0.3819
0.0074	0.1064 to 0.5,-0.25 to -0.3814
0.0000354	0.0202 to 0.0562,-0.0474 to -0.0973
0.0000254	0.0114 to 0.0306,-0.0261 to -0.0571
0.0000154	0.0045 to 0.0117,-0.0106 to -0.0232
0.000001	1.9881×10^{-5} to 5.0496×10^{-5}, -1.0413×10^{-4} to -4.6705×10^{-4}

Table 6.5: *Body force magnitudes for varying Debye lengths*

Debye Length (m)	**Body Force** (N)
0.010	5.4961×10^{-5}
0.0074	1.0036×10^{-4}
0.0000354	0.1625
0.0000254	0.0530
0.0000154	0.0440
0.000001	2.0360×10^{-4}

hand, in Table 6.5 we see that the plasma body force does not follow such a one to one relationship increasing to reach a maximum value of 0.1625 N at $\lambda_d = 35.4\ \mu m$, and decreasing afterward.

iii. Another simulation was done using the PIC model, where the Debye length was modified to the value of 25.4 μm originally used in Orlov's thesis [1], along with the corresponding number density of 8×10^{16} particles per cubic meter. Here too, we maintained the choice of a Kapton dielectric layer, and equivalent values for all other major parameters, as in the benchmark PIC simulation. The results basically showed that the electric potential, electric field, and the plasma body force values were of higher magnitude compared to those obtained in the benchmark PIC simulation while maintaining similar structures about the plasma actuator configuration. About the inner edge of the two electrodes, the electric field, and body force took on maximum values of $\approx 6.71 \times 10^4 N/C$, and $\approx 2.19 \times 10^4\ N$. The electric field magnitude is two orders of magnitude greater than that from the benchmark PIC simulation (230 N/C). Similarly, the body force magnitude is seven orders of magnitude greater than that from the benchmark PIC simulation (0.0010 N). Moreover, there is not much agreement either, when these results are compared to those from the benchmark Orlov simulation where we found a maximum electric field of 60 N/C and body force of $2.05 \times 10^{-6} N$.

6.3 Analyzing the PIC Model

The benchmark simulations for the Orlov and the PIC model, and the various cases considered so far have reinforced the importance in individually examining the major parameters and conditions in both models, and their relationship to other variables. It is now the basis of our motivation to further understanding the mechanisms of these two models, their limitations, and evaluate their efficiency in modeling the plasma actuator flow problem. A glaring weakness of the Orlov model has been its highly simplified approach that is vastly efficient, but failing to provide results with the degree of detail as in the PIC model. This is an inherent attribute of the fluid model. Similarly, there are various facets of the PIC model that can be manipulated to allow for the simulation of different flow environments. The number of parameters utilized in the hybrid PIC model also outnumber those in the fluid Orlov model. While this may allow for a higher degree of detail in the analysis of the phenomenon, it also contributes to the method's selective applicability. So, focusing on the PIC model we will cover a series of simulations that help validate, generalize, as well as review the various properties that differentiate it from the Orlov model. Results from the benchmark Orlov simulation will be referenced whenever appropriate.

6.3.1 Boundary Conditions

The PIC model uses a variety of boundary conditions. For the benchmark simulation, a set criteria of boundary conditions were used along the domain boundaries, the electrodes, and the dielectric layer (Figure 6.1). In order to test particle flow behavior, as well as provide a simple validation of the PIC model, various combinations of boundary conditions were tested:

i. Reflective conditions on the upper electrode, dielectric surface, and on the domain boundaries.

ii. Reflective conditions on the upper electrode and on the domain boundaries, with absorbing conditions on the dielectric surface.

iii. Absorbing conditions on the domain boundaries, the upper electrode, and the dielectric surface.

iv. Reflective conditions on the electrodes, lower ($y = 0$) and upper ($y = Ly$) domain boundaries, with absorbing conditions at the left ($x = 0$) and right ($x = Lx$) domain boundaries.

The settings for the evaluation of Dirichlet and Neumann conditions at the boundaries have been maintained as utilized in the benchmark PIC model shown in Figure 6.1. It suffices to consider one particular example, Case (iv), for analysis. The main parameter concerns the evolution of particle positions through the course of the simulation. The evolution of the particle flow can be seen in Figures 6.9-6.12.

As was expected, due to the reflecting conditions on the electrodes, as well as the upper and lower domain boundaries, the simulation registered a higher particle count, and particles tend to pile up at the edges of the exposed electrode and the dielectric layer. Having maintained the same values for all other parameters, results involving the electric potential, electric field, and the body force contours are structurally similar, and to a certain extent, numerically equivalent to those obtained in the benchmark PIC simulation. Focusing on the body force and the electric field as our primary candidate variables for comparison, Case (iv) results

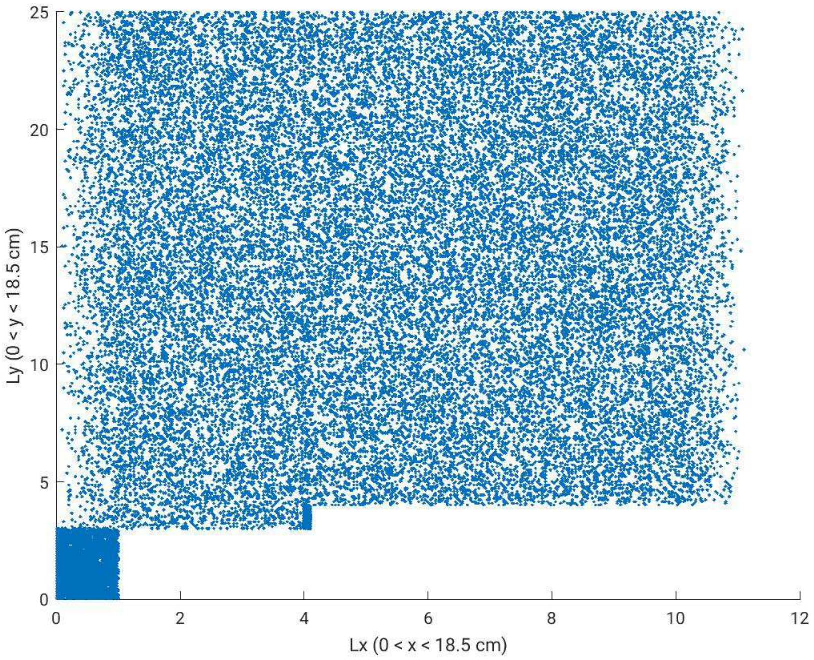

Figure 6.9: *Particle Positions at ts =100.*

in a maximum body force of 0.0015 N, and a maximum electric field of $\approx$ 232 N/C. These values agree very well with the range of maxima found in the benchmark PIC simulation which involves a maximum body force value of 0.0010 N, and a maximum electric field of 230 N/C. The maxima that have been identified for the body force, and the electric field generally refer to the region at the inner edge between the two electrodes, where the electric potential and electric fields are most concentrated. Henceforth, we will mainly list the maxima found for these parameters in our results.

While the results for the plasma body force fields are similar in structure in all the cases considered, the density of contour lines about the inner edges, between the electrodes, and the surface of the dielectric above the encapsulated electrode is the greatest in Case (iv). The maxima for the plasma body force fields from Cases (i) to (iii) are as follows: 4.4325×10^{-5} N (Case (i)), 3.8464×10^{-5} N (Case (ii)), and 0.0011 N (Case (iii)). The magnitude of the plasma body force tends

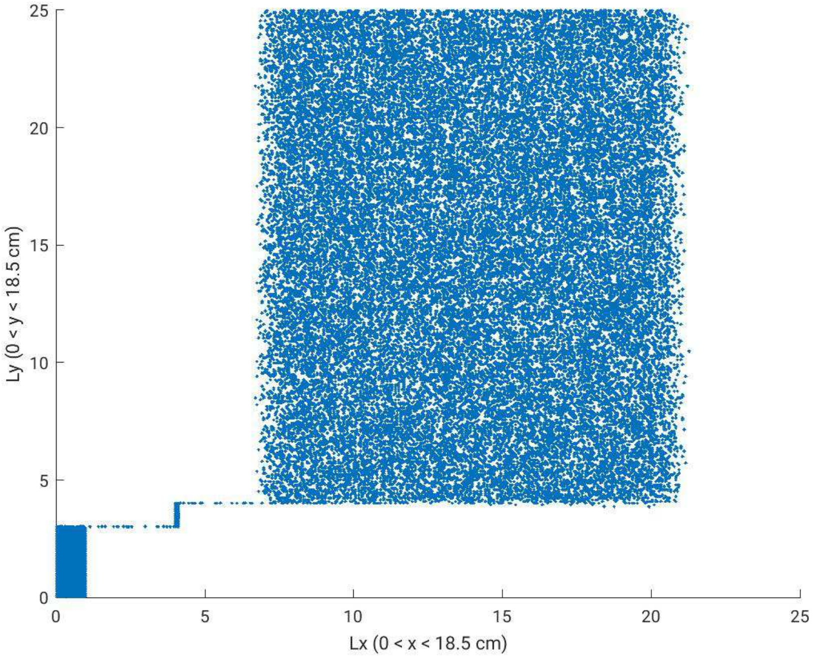

Figure 6.10: *Particle Positions at ts=200.*

to gradually increase until we get to Case (iv) where we have a maximum body force of 0.0015 N.

Furthermore, the periodicity that could be attributed to the electric potential, as observed in the benchmark PIC and Orlov simulations, reaching a unique steady state at the end of the simulation, is not seen in Cases (i) and (ii) (Figures 6.13-6.14) as compared to Cases (iii) and (iv). Similarly, the uniform electric field calculated from these cases also lack in the structure found in the results from the benchmark PIC simulation, for example as in Case (ii), shown in Figure 6.15. While we registered a maximum electric field of 230 N/C in the benchmark PIC simulation, Cases (i) and (ii) result with electric field magnitudes of $\approx$ 124 N/C, and 125 N/C. Similarly, the area above the encapsulated electrode, registers a less negative electric potential compared to the benchmark PIC simulation with a smaller potential fallout of -0.0596 V, -0.4306 V, ..., in Case (i), and -0.0588 V, -0.4294 V, ..., in Case (ii), compared to -0.6702 V, -1.6707 V, ..., in the bench-

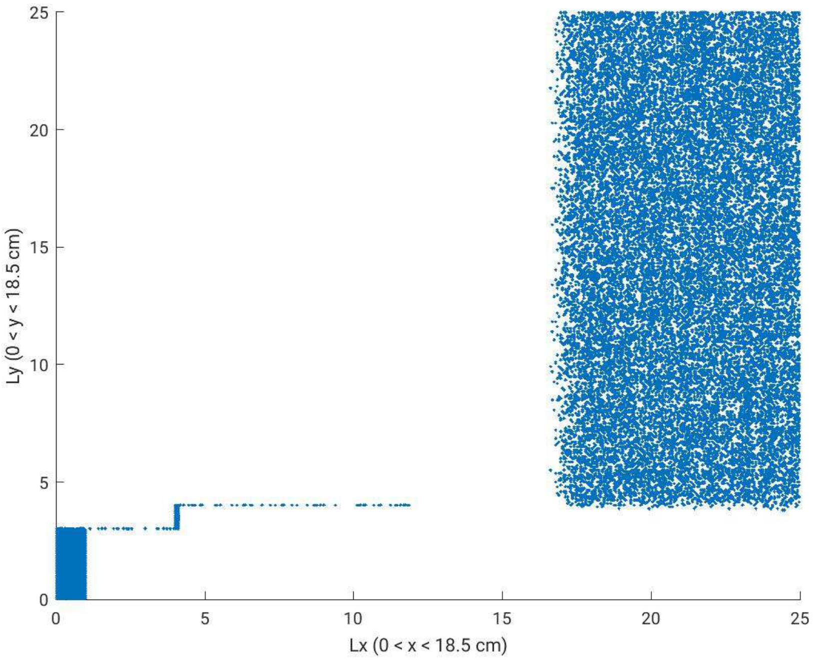

Figure 6.11: *Particle Positions at ts=300.*

mark simulation.

The numerical values of the electric potential and the electric field along the surface of the dielectric, above the encapsulated electrode, as discussed in Cases (i), and (ii) attest to the smaller body force values obtained in those simulations, and the necessity to run the simulation for a longer duration of time in order for the system to achieve a steady state, which may or may not be possible.

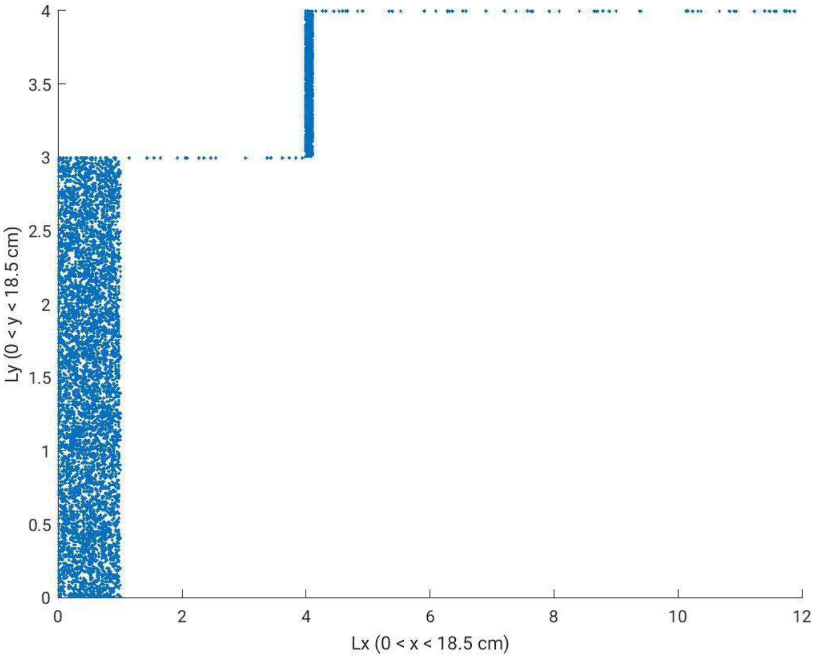

Figure 6.12: *Particle Positions at ts=400.*

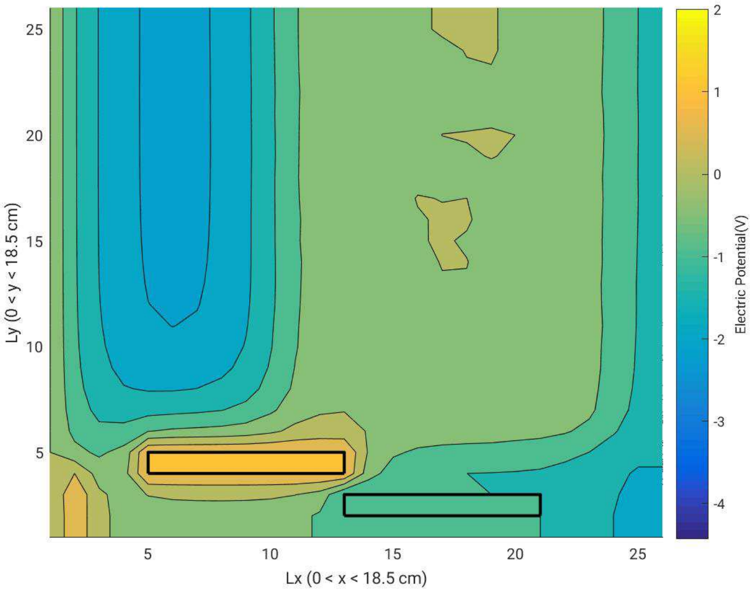

Figure 6.13: *Electric potential contours for Boundary Conditions Case (i).*

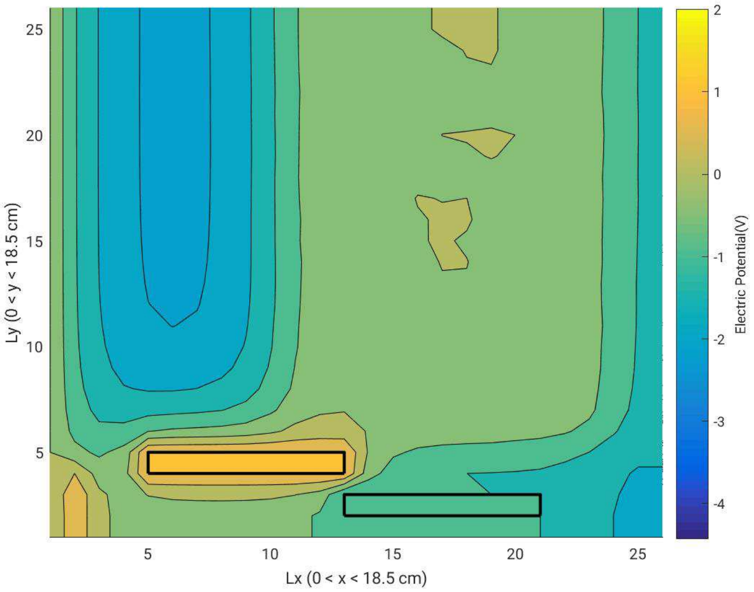

Figure 6.14: *Electric potential contours for Boundary Conditions Case (ii).*

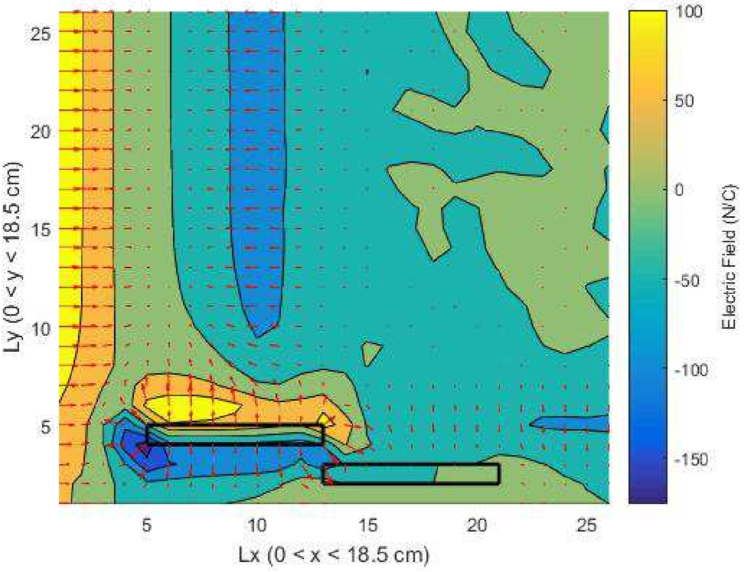

Figure 6.15: *Electric field overlaid with corresponding vector plot for Boundary Conditions Case (ii).*

6.3.2 Electrode Size

The physical size of the electrode, as would be found in a lab environment, does not match the representation provided in the benchmark PIC simulation. With reference to Figure 2.5b, it is understood that the wider the electrode the greater the plasma extent, with ions getting accelerated for a longer distance, subsequently resulting in an increase in the induced velocity at the plasma-dielectric interface. A maximum is achieved at an electrode width of 0.02 m, beyond which there is no significant change in the maximum induced velocity. The benchmark PIC simulation (25 × 25 grid) involves electrode widths of 8 cells ($\approx$ 0.0592 m, where the cell size is 0.0074 m). Modifying only the widths of the electrodes, while maintaining the default constants, and conditions of the PIC model, three different cases were considered,

i. Electrodes are 2 cells long ($\approx$ 0.0148 m).

ii. Electrodes are 4 cells long ($\approx$ 0.0296 m).

iii. Electrodes are 14 cells long ($\approx$ 0.1036 m).

The contours for the electric potential, as well as the vector fields for the electric field, and the plasma body force were representative of the electrode widths. In Case (i), we get the following magnitudes for the body force, and the electric field: $\approx 6.21 \times 10^{-4}$ N, and 227 N/C. In Case 2 we have $\approx 7.28 \times 10^{-4}$ N, and 221 N/C, and lastly in Case 3, we have 0.0012 N, and 217 N/C. The electric potential field is such that for smaller electrode widths we observe a faster drop in the electric potential, and a more negative dielectric surface. For example, in Case (i) we evidence a drop in the following order from -0.6575 V, -1.3805 V, -1.8022 V ...compared to Case (ii) where we have -0.6340 V, -1.3236 V, -1.6721 V...For smaller electrode widths, we also find the contour fields for these parameters to be restricted and clustered about the electrodes, while falling off rapidly beyond the domain of the encapsulated electrode (particularly observable in the electric potential contours). On the other hand, in Case (iii), we find contour structures quite similar to the default PIC simulation. Figures 6.16-6.18 display the contours involving the electric potential in all three cases.

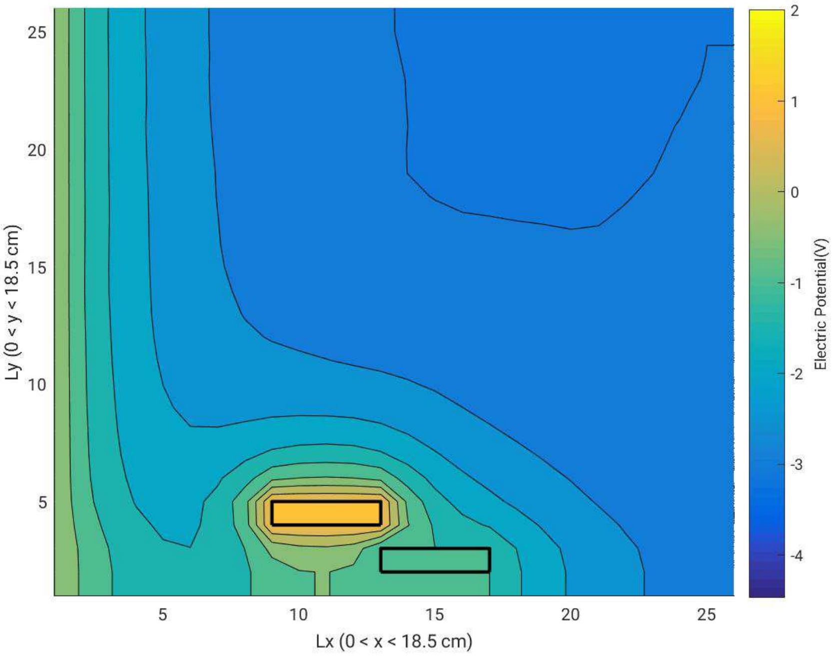

Figure 6.16: *Electric potential contours for Electrode Size Case (i) (PIC model).*

Taking Case (ii) for example, we tried to replicate the same procedure with the benchmark Orlov model, for the specific electrode width. Figure 6.19 presents the electric potential contours involving Case (ii), from the corresponding Orlov simulation. The results from the Orlov model show a maximum electric field magnitude of 58.0799 N/C, and a maximum body force of 2.0492×10^{-6} N. Electric potential isolines about the exposed electrode range from magnitudes of 0.0937 V to 0.04 V, and -0.1208 V to -0.3496 V about the encapsulated electrode.

Just as we had observed in the prior chapter, the PIC and Orlov model results do not agree numerically, or even remotely, though they seem to agree on the general characteristics of the contour fields for each parameter. It seems that smaller electrode widths lead to a faster decay of the aforementioned parameters, as one moves away from the plasma actuator. This can be due to the greater plasma extent involving larger electrode widths, resulting in higher magnitudes for the electric field, electric potential, and the plasma body force, in the vicinity

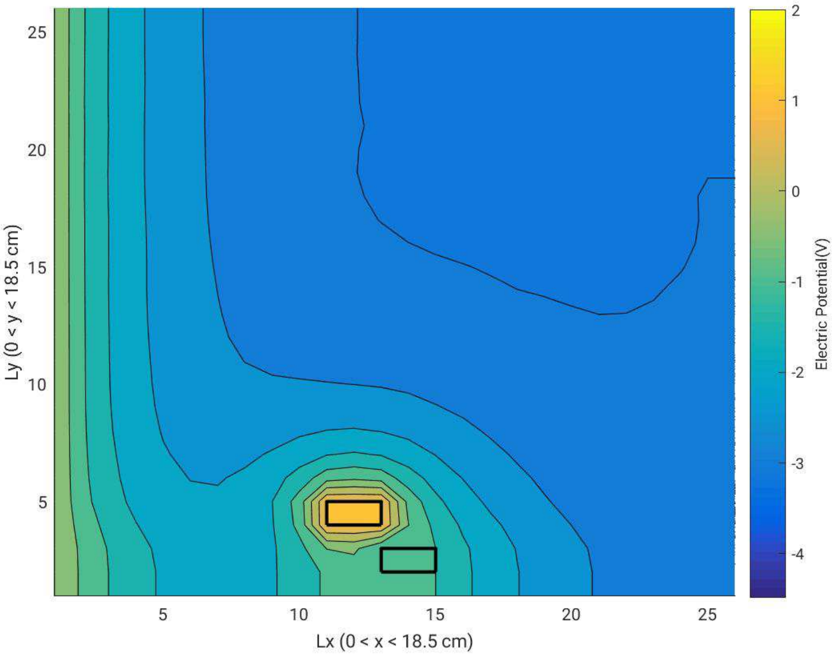

Figure 6.17: *Electric potential contours for Electrode Size Case (ii) (PIC model).*

of the space above the encapsulated electrode, and a slower decay rate in all three parameters. This may lead to more prominent flow field configurations in cases involving longer electrode widths since the plasma extent is longer due to the larger surface area and width of the encapsulated electrode.

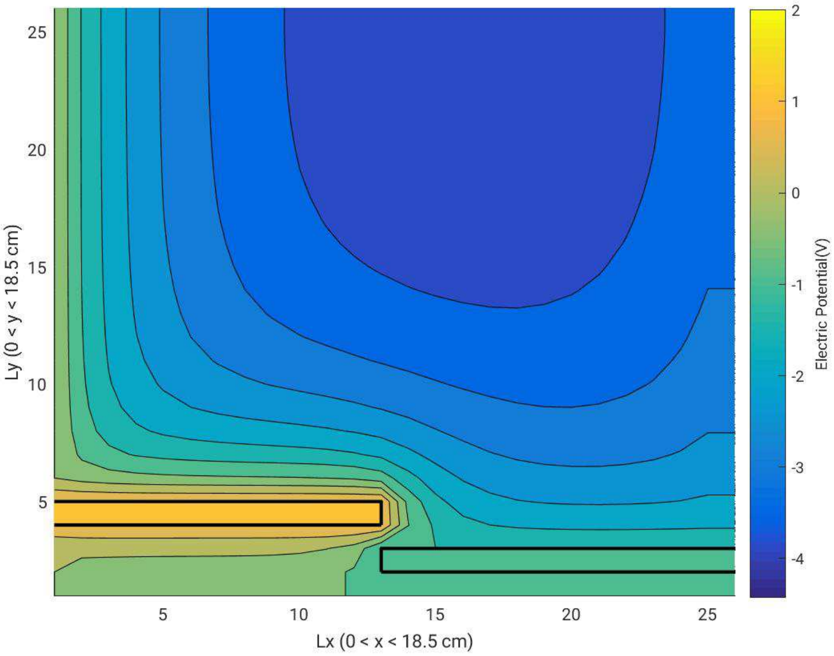

Figure 6.18: *Electric potential contours for Electrode Size Case (iii) (PIC model).*

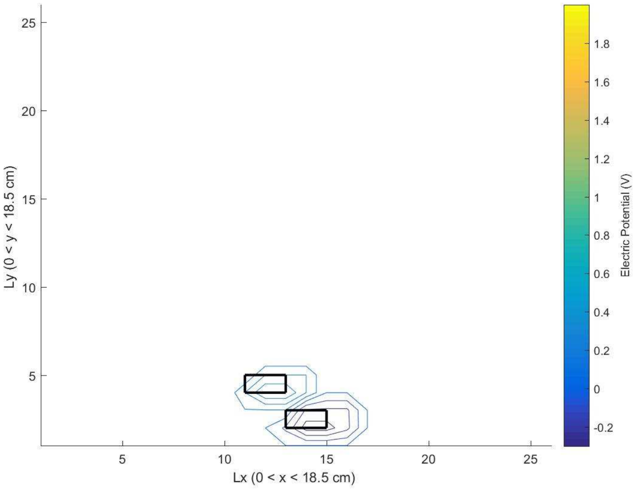

Figure 6.19: *Electric potential contours for Electrode Size Case (ii) (Orlov model).*

6.3.3 Electrode Gap

With reference to experimental work performed by Forte [15], and Corke [5; 9], the gap between the electrodes can be modified to reinforce, and strengthen the plasma body force exerted by the plasma actuator. Forte presented the evolution of the maximum induced velocity of the volumetric SDBD plasma as a function of electrode gap (Figure 2.5a). An ideal gap value of 5 mm provided the maximum induced velocity. This was done using a 2 mm-thick plexiglass dielectric plate, with two 5 mm-wide electrodes, an AC voltage of 20 kV, and frequency of 700 Hz. The optimum electrode gap is considered to be 5 mm, as for higher gap values, it is surmised that the electric field may drop down, and the space charge cannot continue onward to the encapsulated electrode downstream. We specifically consider the following four cases where a cell width of 0.0074 m is assumed.

i. Electrode gap of 2 cells (0.0148 m).

ii. Electrode gap of 4 cells (0.0296 m).

iii. Electrode gap of 5 cells (0.037 m).

iv. No electrode gap, but the encapsulated electrode is moved one cell width deeper into the dielectric.

Figures 6.20-6.23 present the plasma body force fields for the various gap scenarios listed above superimposed on electric field contours. Rather than vector plots for the electric field, we are presenting the figures using contours to show that despite the modification of electrode gaps, the plasma body force and electric fields are most concentrated by the edge of the exposed electrode, as has been noted in all our results so far. Beginning with Case 1-3, we get body force maxima, in that order, of $9.02 \times 10^{-4}N$ N, $9.42 \times 10^{-4}N$, and 9.95×10^{-4} along with electric field maxima of 223 N/C ,225 N/C, and 227 N/C. This shows that by increasing the electrode gap we are proceeding towards higher magnitudes for the set parameters. Case (iv) presents the largest resultant magnitudes for both the body force, and the electric field with 0.0010 N, and 230 N/C.

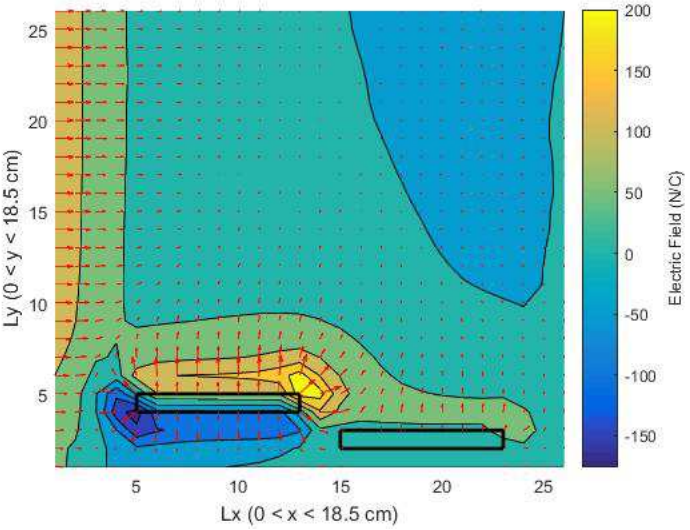

Figure 6.20: *Body force vector field superimposed on Electric field contours for Electrode Gap Case (i) of 2 cells.*

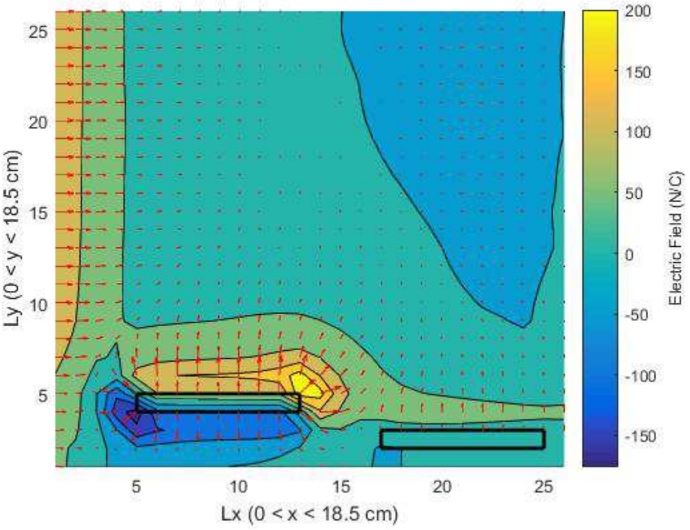

Figure 6.21: *Body force vector field superimposed on Electric field contours for Electrode Gap Case (ii) of 4 cells.*

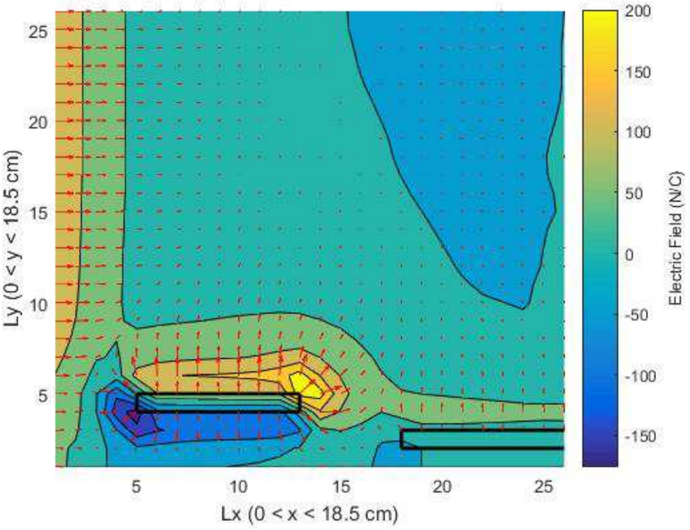

Figure 6.22: *Body force vector field superimposed on Electric field contours for Electrode Gap Case (iii) of 5 cells.*

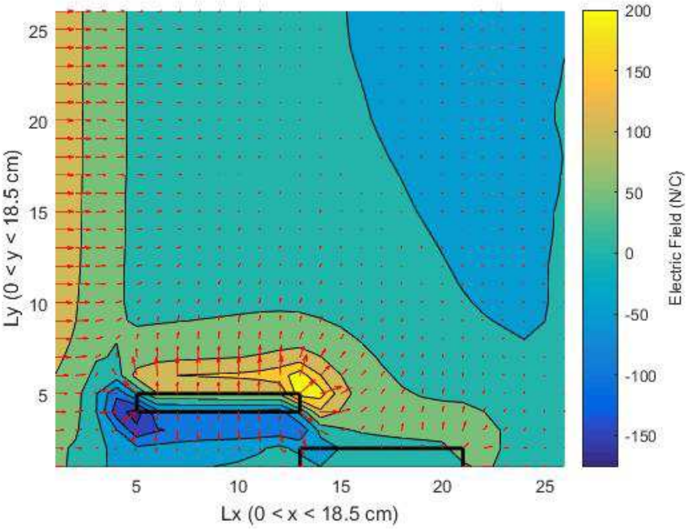

Figure 6.23: *Body force vector field superimposed on Electric field contours for Electrode Gap Case (iv).*

6.3.4 AC Voltage

In the approaches considered so far, the electrodes are provided with a constant potential value of $\pm 1\ V$. This would correspond to the use of a DC voltage, which in reality, would not be suitable for a SDBD actuator, as a direct current cannot cross the dielectric barrier, and may not provide for a stable plasma discharge. In fact, DC voltages would be more appropriate for a DC discharge/Coronal discharge actuator, both of which utilize slightly different configurations compared to the SDBD plasma actuator. Thus, it is necessary that unlike the constant voltages used in the original PIC simulations, an AC voltage involving a simple time-dependent structure, be used as follows,

$$\phi(t) = \phi^{max}(t) f(t) \tag{6.1}$$

where,

$$f(t) = sin(2\pi\omega t). \tag{6.2}$$

ϕ^{max} is the amplitude of the sine wave, while $\omega = 2\pi f$ is the angular frequency, and f is the frequency of the wave. The exposed electrode is generally provided with an AC voltage while the encapsulated electrode remains grounded. Four simulations were made with varying ranges of amplitudes (A), and frequencies (f) for the AC voltage (while maintaining the benchmark PIC conditions on all other parameters):

i. $A = 2\ V, f = 3\ Hz$.

ii. $A = 2\ V, f = 100\ Hz$.

iii. $A = 50\ V, f = 100\ Hz$.

iv. $A = 100\ V, f = 3\ Hz$.

It was observed that in all four cases, a secondary area of concentrated electric fields formed at the edge of the encapsulated electrode, as in Cases (iii), and (iv), for example, shown in Figures 6.24 - 6.25.

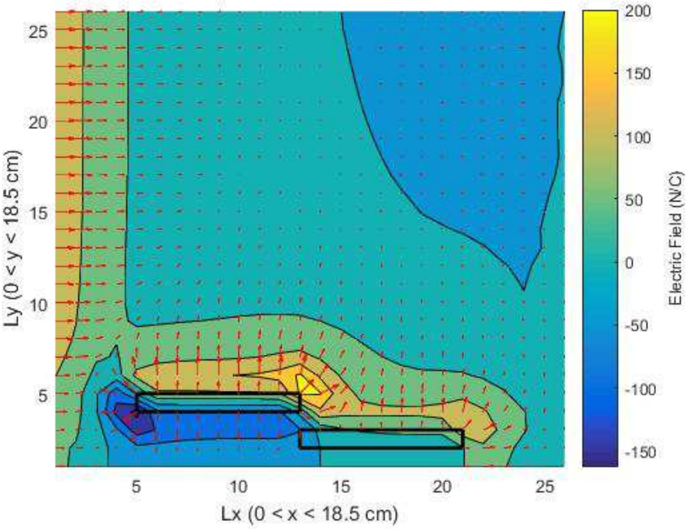

Figure 6.24: *Electric field contours for AC Voltage Case (iii) superimposed with the corresponding vector field.*

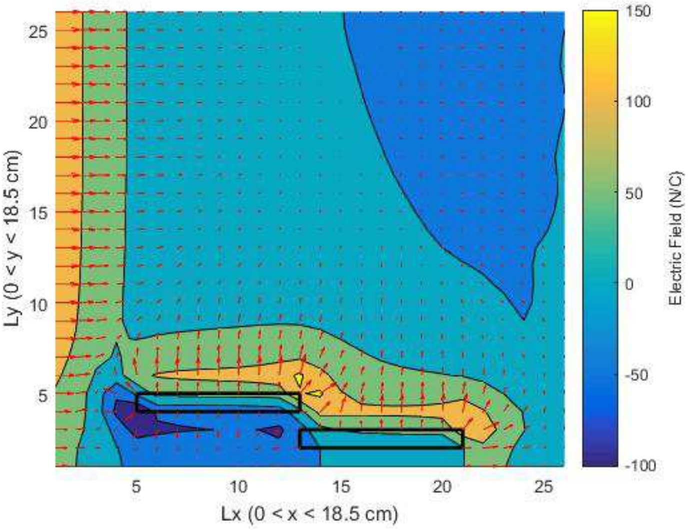

Figure 6.25: *Electric field contours for AC Voltage Case (iv) superimposed with the corresponding vector field.*

Starting with Case (i), we have a maximum plasma body force near the inner edge of the two electrodes of 8.1×10^{-4} N. The corresponding magnitudes of the electric field at the primary and secondary regions are 155 N/C, and 140 N/C. The electric potential of the exposed electrode at the end of the simulation is 0.0010 V. There is a progressive increase in the magnitudes of the *primary* parameters when larger frequencies are used for the AC voltage supplied to the electrodes. For example, in Case (ii), we have *primary* and *secondary* electric field magnitudes of 158 N/C, and 140 N/C. The plasma body force involved has a maximum magnitude of 8.5×10^{-4} N. The electric potential on the exposed electrode at steady state is now 0.0335 V. Note, the *secondary* regions for the electric field do not experience any changes in magnitudes.

Corresponding increases in the amplitude of the voltage waveform also accommodates for similar behavior, as in Case (iv), where the amplitude of the waveform is increased to 100 V, while maintaining a frequency of 3 Hz as in Case (i). This resulted in *primary* and *secondary* electric field magnitudes of 158 N/C, and 140 N/C. The electric potential on the exposed electrode is now 0.0503 V. A maximum plasma body force of $8.34 \times 10^{-4} N$ is also noted. Similarly, Case (iii) combines an increase in the amplitude as well as the frequency of the AC voltage waveform, giving us *primary* and *secondary* electric field magnitudes of 207 N/C, and 140 N/C. The results present a maximum plasma body force magnitude of 0.0010 N.

In the end, it is by changing the frequency of the waveform that we achieve greater magnitudes for the resultant *primary* electric field magnitudes, and the plasma body force parameters. This is of great interest as the related region is where we would prefer the plasma actuator to impart the most momentum into the airflow in order for it to be diverted smoothly along the dielectric surface.

6.3.5 Material Considerations

A variety of materials can be utilized for the dielectric layer. The benchmark PIC model uses a Kapton dielectric layer ($\epsilon_{r,Kapton} = 2.7$). Two additional cases were analyzed using the benchmark PIC setup, each involving a different dielectric medium, including Teflon ($\epsilon_{r,Teflon} = 2.1$), and Plexiglass ($\epsilon_{r,Plexiglass} = 3.4$). The dielectric constant at the interface for each medium is found to be,

i. $\epsilon_{r,Teflon-Air} = \text{mean}(2.1 + 1.0) = 1.55$

ii. $\epsilon_{r,Plexiglass-Air} = \text{mean}(3.4 + 1.0) = 2.2$

Simulations involving the two dielectric media were also made using Orlov's model, with the benchmark setup. Beginning with Teflon, the PIC results register a maximum body force of 0.0011 N, and a maximum electric field of 231 N/C at the inner edges of the two electrodes. A Plexiglass dielectric medium results in a body force of 0.0010 N, and an electric field of 227 N/C. With a Plexiglass medium, the system registers a weaker negative potential line along the surface (-0.6479 V, -1.3375 V, -1.6743 V...) compared to a Teflon medium (-0.6900 V, -1.3905 V, -1.7235 V...). Figures 6.26 and 6.27 present the electric potential contours resulting from the use of the two dielectric media.

Note that in the benchmark PIC simulation, which uses a Kapton dielectric medium, the system sustains a maximum body force of 1.22×10^{-4} N, and an electric field of 230 N/C. These results portray Teflon as the most favorable dielectric medium for the plasma actuator system. When compared to the results obtained from Orlov's model, we are once again faced with numerical discrepancies in the individual magnitudes of each parameter. Otherwise, the Orlov results also prove Teflon as the most favorable dielectric medium for the plasma actuator system. The Teflon medium results with a body force of 2.10×10^{-6} N, and an electric field magnitude of 60 N/C, compared to 2.03×10^{-6} N, and 56 N/C for the Plexiglass medium. The behavior of the electric potential is equivalently similar with the Plexiglass medium registering weaker electric potential isolines about the two electrodes ranging from 0.0714 V to 0.4000 V (for the exposed electrode), and -0.1096 V to -0.3425 V (for the encapsulated electrode), versus 0.1198 V to 0.4000 V, and -0.1356 V to -0.3590 V for the Teflon medium.

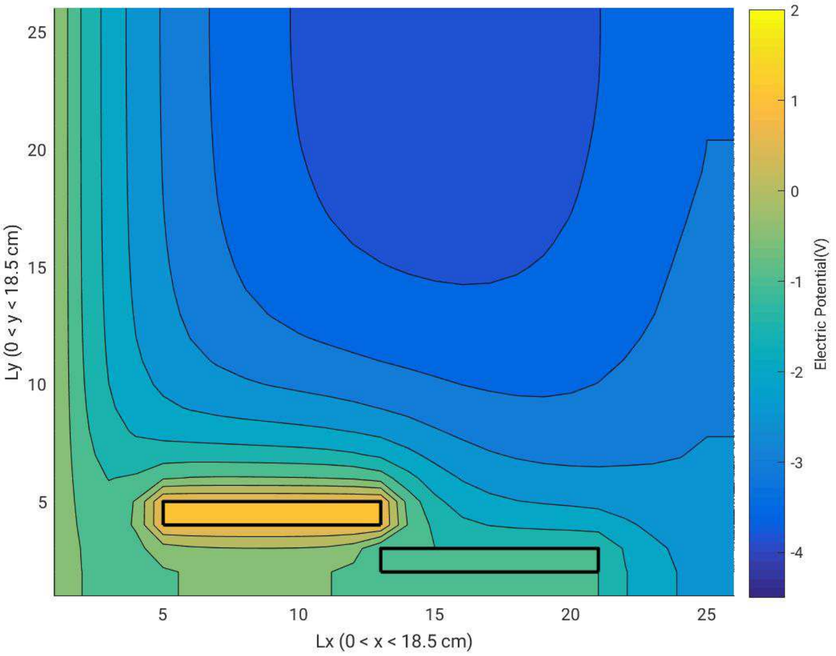

Figure 6.26: *Electric potential contours for a Teflon dielectric.*

6.3.6 Flight Conditions

The benchmark PIC model involves a particle injection velocity of 70000 m/s. This is not practical considering the flow speeds generally encountered in cruise flight conditions. Four cases of varying flow speeds have been tested, while maintaining the benchmark PIC parameters for all other variables. This has allowed us to test possible scenarios which could involve system instabilities. The four cases are as follows,

i. $v_{Drift} = 260\ m/s$

ii. $v_{Drift} = 990\ m/s$

iii. $v_{Drift} = 977.55\ m/s$

iv. $v_{Drift} = 500\ m/s$

The cruising flight speed on commercial airliners is 926 km/h or $\approx 260\ m/s$. It was noted that with the benchmark PIC conditions (where $n_0 = 10^{12}$ particles per

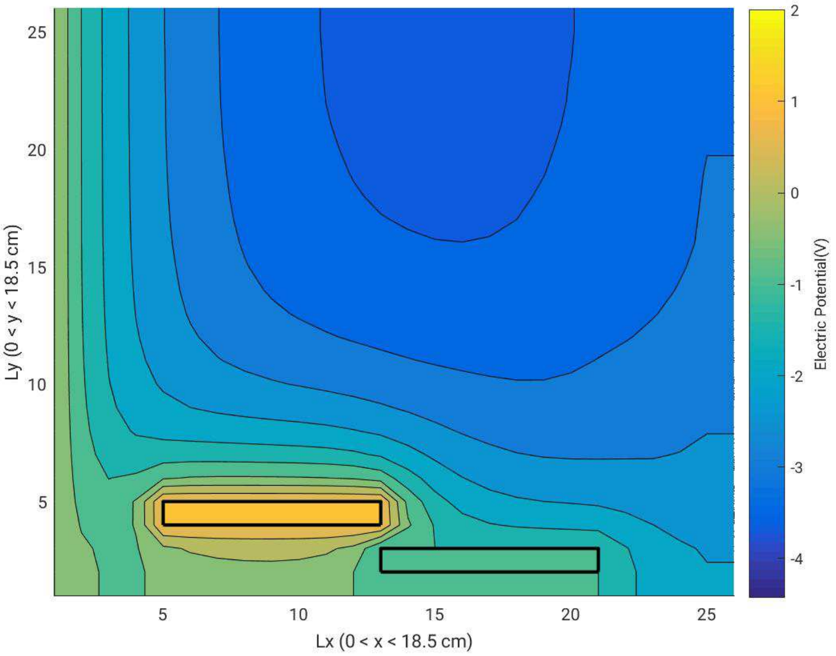

Figure 6.27: *Electric potential contours for a Plexiglass dielectric.*

cubic meter, along with a cell width of 0.0074 m), Cases (i), and (iv) violated the plasma stability criterion as $\omega_{pi}\Delta t > 1$. We are considering here the plasma ion frequency rather than the plasma electron frequency as noted in (2.4) as the PIC model involves kinetic ions with a fluid electron background. Cases (ii), and (iii) registered values of ≈ 0.9920, and ≈ 0.9999 for the same product nearly avoiding violation of the stability criterion. We are mainly interested in addressing the evolution of particle positions through the course of these simulations.

The particle positions are defined via the equations of motion, which requires knowledge of the electric potential, and the subsequent electric field at a given location in the computational domain. Figures 6.28-6.31 illustrate the particle distributions for these four cases.

Unlike the benchmark simulation, where the particles travel from the left, to the right, while being absorbed at the dielectric surface, and the upper electrode, the

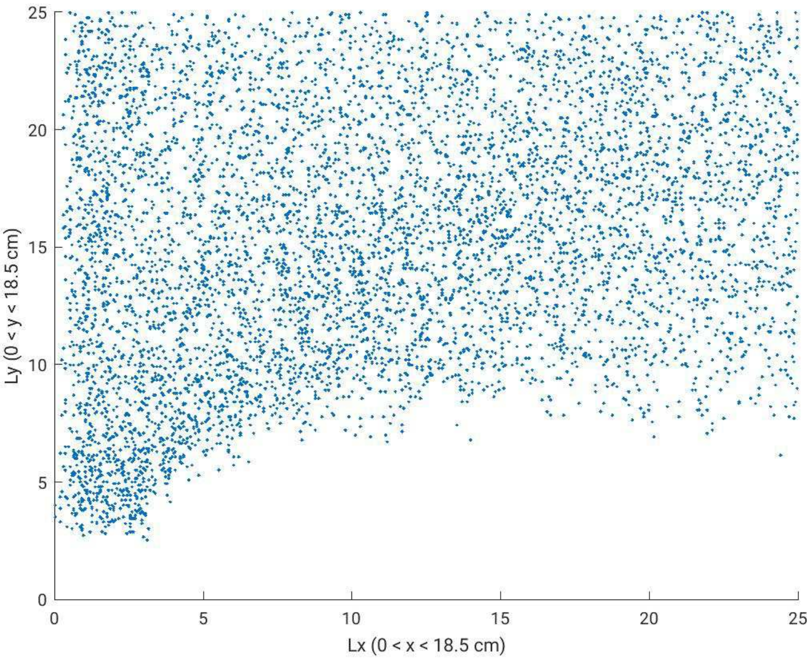

Figure 6.28: *Particle Positions for Case (i) for 260 m/s.*

particles here encounter a divergence in the speeds listed above, resulting in a flow that is reminiscent to that of an airfoil, surrounding the plasma actuator. As observed, the airfoil-like distribution of the particles dips lower towards the dielectric surface as $v_{Drift} \rightarrow$ stable conditions where the plasma stability criterion is satisfied (Cases (ii), and (iii)). We also find that by approaching flight speed conditions, the system presents higher magnitudes for the electric field, and plasma body force.

6.4 Conclusion

This chapter involved several parametric tests of the Orlov and PIC models. A variety of simulations involving different scenarios were made. In the following chapter, we will shed some perspective on these collective results with a thorough discussion of their meaning, significance, and end with closing remarks on the prospects for future research on this subject.

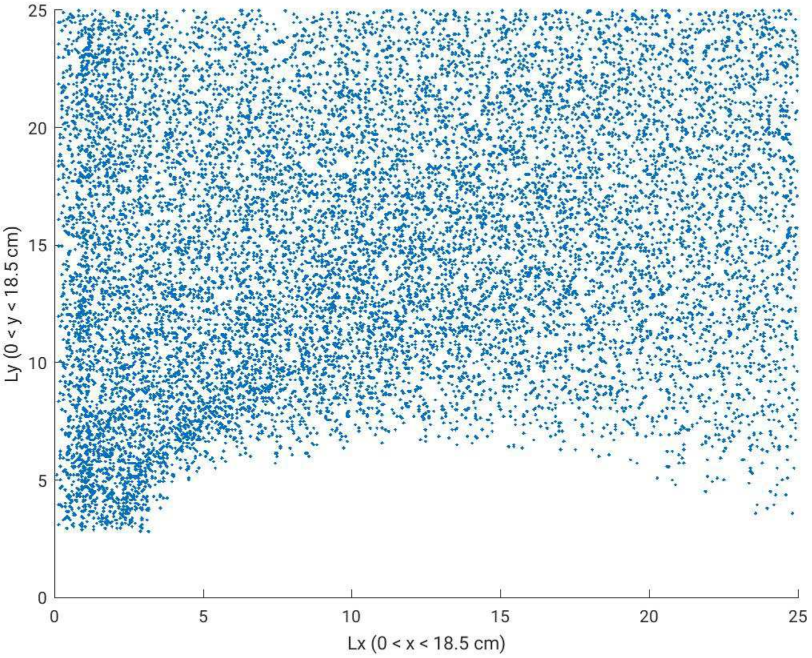

Figure 6.29: *Particle Positions for Case (iv) for 500 m/s.*

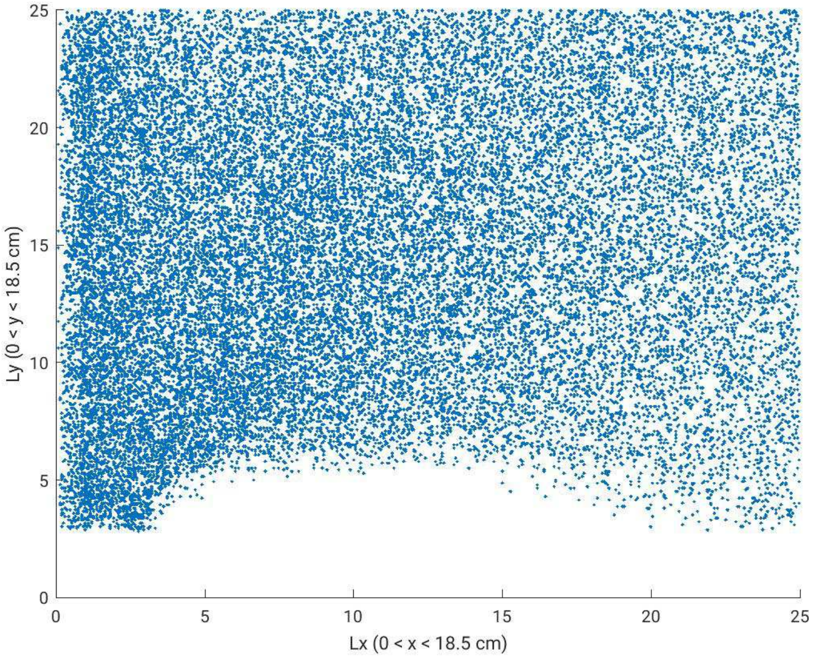

Figure 6.30: *Particle Positions for Case (iii) for 977.55 m/s.*

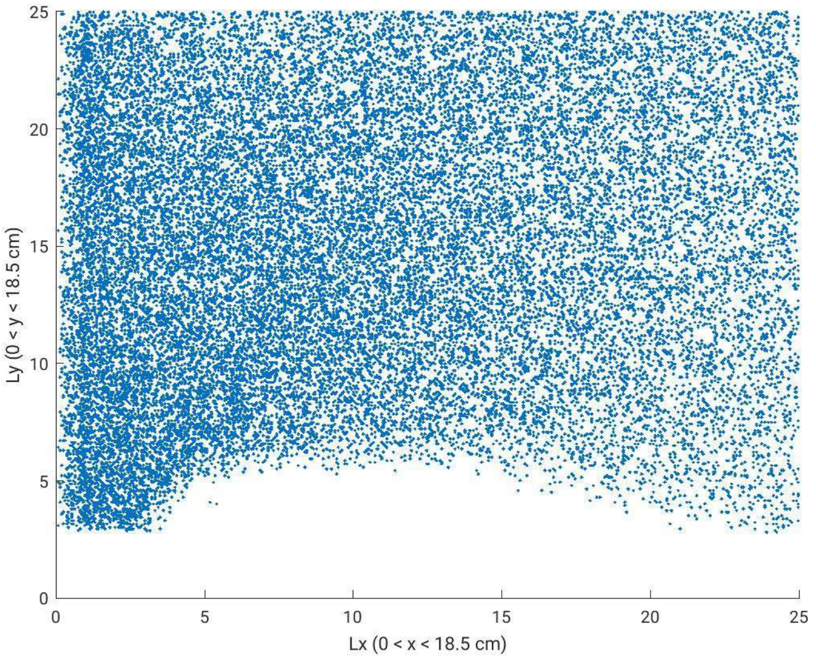

Figure 6.31: *Particle Positions for Case (ii) for 990 m/s.*

Chapter 7

Discussing the Results

7.1 Summary

A variety of simulations have been considered so far. Having analyzed the results from the benchmark PIC and Orlov simulations, we moved on to Case (i) where two simulations were made with the Orlov model using 50×50, and 201×201 grids. The Debye length utilized in both cases was 0.0074 m, along with a tolerance level of 0.1 for the potential solver. We noted that the physical lengths of the domains were different in these latter cases compared to the benchmark Orlov simulation but despite this found our final results from the two simulations to be identical to those from the benchmark Orlov simulation. This was an indication that the differing physical lengths of the computational domain do not have much of an influence in the problem. This left us with the parameters for the dielectric materials, solver tolerance, and the Debye lengths. One of these scenarios, involving the Debye length, was tested in Case (ii) where we found that the magnitudes of the electric field and electric potential decrease as the Debye length decreases. This one-to-one relationship did not translate to the results involving the plasma body force.

Now in analyzing these results, it is necessary to consider the practicality of the Debye length values used to characterize the SDBD plasma. Discharge plasmas used for airflow control are usually atmospheric corona discharges and dielectric barrier discharges. Their characteristics are typically as follows: high voltages of a few kV to several tens of kV with DC or AC excitation, with frequencies from 50 Hz to 50 kHz, electrical currents from a few μA to a few mA. In these conditions, the density of charged species is between 10^9 and 10^{13} cm^{-3}, and the electron temperature is a few eV. Unlike the PIC model, the Orlov model lacks in the number of parameters used to characterize the plasma actuator. In fact, it is only the Debye length that serves as the primary variable in the Orlov model's simulation of the SDBD plasma. Industrial plasmas in general involve Debye lengths of 25.4 μm. The Debye lengths utilized in Case (ii) from 25.4 μm, and in the range between ± 0.01 mm of this value are applicable in reality. Alternatively, Debye lengths within the range of 10^{-2} m to 10^{-3} m can be used to model plasmas in the atmosphere, specifically, the ionosphere, while a Debye length of 10^{-6} m would be found in environments such as a fusion reactor or the solar core. These choices do not necessarily make for practical implementation in modeling the SDBD discharge. Thus, we have shown the significance of the Debye length in the Orlov model. In comparing results from this model to that of the PIC model, it is necessary that practical and correct values for the Debye length are used.

This paved the way to the discussion of Case (iii), where the Debye length was modified in the benchmark PIC model to the value of 25.4 μm along with the corresponding number density of 8×10^{16} particle per cubic meter. While the output values for the electric potential, electric field, and the plasma body force registered higher values compared to the benchmark PIC simulation, there was also no room for agreement with the results from the benchmark Orlov simulation. But most importantly, the results found in Case (iii) are impractical as the physical area of the domain is an unrealistic 4.03225×10^{-7} m^2. Nevertheless, the simulation certainly indicated that the electric field and plasma body force magnitudes are also influenced by changes in number density.

Through these simulations we have been able to show that even the smallest of parameters used to characterize the SDBD plasma actuator flow problem have a great influence on our results. This is particularly evident in the PIC model.

Unlike the Orlov model, the PIC model involves the use of codependent variables, like the Debye length, in its formulation. In the PIC model, the cell size is set equivalent to the Debye length. The cell is generally the smallest size across which we can resolve changes in various properties. Thus, the cell size is also a function of whatever phenomena we are trying to resolve. For example, if we a have a beam that is 5 cm across, a 2 cm cell size will only provide for two to three nodes across the beam. This will not be enough to resolve the beam's detailed structure. The physical lengths of our domain is computed by taking the number of nodes in the grid, and multiplying it to the cell size. In Case (iii), the PIC simulation used $\lambda_D = 25.4\ \mu m$, in a 25 × 25 grid, such that the area of our domain is an impractical $4.03225 \times 10^{-7}\ m^2$.

It is important that the Debye length value is chosen such that the code satisfies the plasma stability criterion, where if $\omega_{pi}\Delta t > 1$, the plasma is unstable. Furthermore, we must also consider the values utilized for the number density, the temperature of the particle species, the particle injection velocities etc. Altering the physical length by using the correct proportionality factor does not solve the problem, as this conflicts with the random number particle generator used for particle generation in the code. The particle generator is set such that particles are randomly distributed in $\hat{y}$ and the first cell. The cell size, and the length of the domain come into play in determining this factor which subsequently is utilized in the calculations for particle propagation. In the end, to get a reasonable physical length for the domain with a set Debye length, a larger grid would be required. This would require a larger number of iterations toward the solution, and is ultimately a time consuming procedure. These concepts are at the crux of this thesis. In the end, the results procured from the benchmark simulations emphasized the importance of individually examining the major parameters and conditions in both models, as well as their relation to other variables.

Consequently, a select number of simulations were made relating these concepts, and allowing us to decipher the various pros and cons of the two methods in their modeling of the SDBD plasma actuator flow problem. These simulations were also a means through which we provided for the validation and generalization of the Orlov, and PIC models, as they surveyed a variety of scenarios:

i. Evaluating differing boundary conditions.
ii. Analyzing the influence of various electrode sizes, and configurations.
iii. Running an AC voltage through the plasma actuator system.
iv. Consideration of different dielectric materials.
v. Testing the PIC model's validity under flight conditions.

7.1.1 On Differing Boundary Conditions

Let us begin by discussing the *evaluation of differing boundary conditions.* Much of this section emphasized the importance of boundary conditions in accurately characterizing the plasma actuator mechanism and particle interactions, involving a fixed configuration, for an optimal mechanical output. The simulations also provided for the validation of the benchmark PIC model, and its construction.

Case (iii) was most similar to the benchmark PIC simulation, and provided an accurate characterization of the plasma actuator with a maximum electric field magnitude of 228 N/C, and a maximum body force of 0.0011 N. These values agree within 1 % of those computed in the benchmark simulation. Case (iv), on the other hand, provided values within the same range of error with an electric field of 232 N/C, and a body force of 0.0015 N. Case (iv) also correctly modeled the expected pile-up phenomena about the electrodes, and the dielectric surface, as one would expect in reality, unlike Case (iii) and the benchmark PIC simulation, which both use absorbing boundary conditions on the electrodes, and the dielectric surface.

Cases (i) and (ii) were lacking in their results, as they unrealistically portrayed the system with reflecting conditions to the domain's left, and right, or even at all its boundaries. The lack of structure in the electric fields, along with a loss of the periodic behavior in the electric potential, often observed as the system settles into a steady state, the numerical discrepancies in the magnitudes of the plasma body force and the electric field when compared to the benchmark PIC simulation supports this fact.

While Case (iii) was closest in construction to the benchmark PIC simulation, in the end, it was Case (iv) that served to be the most realistic of all the scenarios considered, with a great degree of agreement to the results conceived in the benchmark PIC simulation. The study also highlighted an obvious deficiency in the Orlov model which is the lack of complex boundary conditions in modeling the SDBD plasma actuator flow problem. This is of great importance if one wishes to analyze plasma sheath physics, or is interested in plasma phenomena occurring at the edges of the electrodes.

7.1.2 On Varying Electrode Sizes, and Gaps

We then moved on to *analyzing the influence of various electrode widths/sizes, and gap configurations* on the mechanical output of the plasma actuator system. Due to the nature of the code and the MATLAB programming environment used extensively in this thesis, it was difficult to account for fractional discretization involving structural modifications of the electrode widths and gaps.

Beginning with the three cases considered for varying electrode widths, we worked with the knowledge that an optimum electrode width of 0.02 m achieved a maximum induced velocity as presented by Forte [15]. Forte also states that while the wider the electrode, the greater the plasma extent, causing ions to be accelerated for a longer distance, and resulting in a velocity increase. But, there is a limit. While the phenomenon behind the plasma formation may be self-sustaining, it is a dissipative process, leaving the plasma to expand not more than 20 mm. Roth concludes in his work that the best SDBD plasma actuator configuration would involve an electrode gap of 0, and an electrode width of 20 mm, or a gap of 5 mm, and an electrode width of 15 mm. The electrode widths mentioned pertain to the encapsulated electrode, over which the plasma forms.

In our study, we considered three cases involving electrode widths of 0.0148 m (Case (i)), 0.0296 m (Case (ii)), and 0.1036 m (Case (iii)). An electrode gap of 0 m was utilized in all three cases. As expected, we observed a faster drop in the electric potential for smaller electrode widths. This was shown by comparing the electric potential values along the dielectric surface for Cases (i) and (ii). The result agrees with the fact that longer electrodes provide for a greater plasma extent, which brings us to Case (iii) involving the largest electrode width. Interestingly enough, while Case (iii) provides for a smaller drop in the electric potential along its surface with values of -0.6763 V, -1.3759 V, -1.7129 V, hinting at a longer plasma extent, and resulting in the largest magnitude for the plasma body force (0.0012 N), but the smallest magnitude in the electric field (217 N/C).

These seemingly contradictory results can be a consequence of the fact that unlike Forte, the electrode width modifications were utilized on both the exposed and the encapsulated electrode (Forte only modified the width of the encapsulated electrode) making direct comparisons to his results impractical. One must also note that Forte's plasma actuator configuration involved a 2 mm thick plexiglass plate, with the electrodes supplied an alternating voltage of 20 kV, and frequency 700 Hz. Our simulations do not account for this, where a constant potential of ± 1 has been used on the electrodes with a Kapton dielectric layer.

Moving on, through the *evaluation of different electrode gaps* it was observed that the highest concentration of the electric field and the body force is restricted exclusively to the inner edge of the upper electrode, while the fields dissipate at faster rates, along the gap region for larger gaps. This was later identified to be a consistent behavior of the SDBD plasma actuator system throughout all the simulations discussed in this work. Another result of interest was that Case (iv) (electrode gap of zero, but the encapsulated electrode is moved one cell width (0.0074 m) deeper into the dielectric) displayed the largest resultant magnitudes for the plasma body force force (0.0010 N), and the electric field (230 N/C). This result agreed with the experimental observations of Erfani [32] where it was found that actuators with a deeper encapsulated electrode are able to induce higher velocities (which implies a greater injection of momentum in the boundary layer, and subsequently a larger plasma body force magnitude). We initially presumed that the electric field, and plasma body force quantities are directly coupled to the equations of particle motion, and as such these results confirmed our expectations. At the same time, we cannot deny that our results are not comparatively valid, as unlike Erfani, we used a DC voltage implementation on our plasma actuator system.

Implementing these varied gap configurations in the Orlov model, we found that the results for the body force, electric field, and electric potential were identical over all four cases. A maximum body force magnitude of 1.3521×10^{-6} N was found at the inner edge of exposed electrode, corresponding to an electric field of 40.3536 N/C. The electric potential contours about the exposed electrode varied in a range from 0.0937 V to 0.4000 V, and -0.1208 V to -0.3496 V about the encapsulated electrode. The identical results served to illustrate the Orlov model's weakness in representing the influence of structural changes in the plasma actuator configuration.

In the future, in order to make valid comparisons to the work presented by Erfani, Forte, and Corke on the use of electrode gaps to optimize the mechanical output of the plasma actuator, it will be fruitful to consider modeling the plasma actuator problem with a smaller cell width. The four cases that have been explored in this thesis utilize a cell width of 0.0074 m. As mentioned earlier, Forte states that the best SDBD plasma actuator configuration would involve an electrode gap of 0 and an electrode width of 20 mm, or a gap of 5 mm and an electrode width of 15 mm. Thus, a suitable simulation would involve modifying the cell width, or configuring the electrode positions to match the optimal scenario.

7.1.3 Running an AC Voltage

With respect to the deductions made regarding the use of different electrode widths and gaps, it was natural to follow up by considering the *use of an AC voltage* on the electrodes. The AC voltage was applied on the exposed electrode while the encapsulated electrode remained grounded. Four simulations involving waveforms of different amplitudes, and frequencies were considered.

Unlike earlier results, a secondary area of concentrated electric fields was observed at the edge of the encapsulated electrode. This was most prominent in Cases (iii) (A= 50 V, f = 100 Hz), and (iv) (A = 100 V, f = 3 Hz). Between changing the amplitudes, and frequencies of the waveforms, we found that we can achieve greater magnitudes for the plasma body force, and *primary* electric field magnitudes for waveforms of higher frequencies. This was exemplified by the results provided in Case (iii), where the plasma body force (0.0010 N), *primary* (207 N/C), and *secondary* electric field (140 N/C) magnitudes were the highest among the four cases.

The small magnitudes for the amplitude, and frequency of the sine waveforms were chosen specifically to avoid instabilities that afflicted the particle flow with the choice of larger values for the same parameters. This manifested in the form of a clear loss of structure in the electric potential contours, the electric, and the plasma body force fields. Thus, the PIC model, in its current state, is unable to accommodate for such modifications. This can also be a natural limitation of the system as the stability of the plasma discharge is linked to the magnitudes of frequencies and amplitudes used for the AC voltage [8]. To construct a stable glow discharge and avoid the unfavorable filamentary phase or glow-to-arc transitions, experiments generally focus on low magnitudes for the amplitude and frequencies of the AC waveform as during said transitions the electrical currents are concentrated within a few filaments, sparks may appear, and the discharge would be difficult to control.

Future work would focus on addressing this flaw of the PIC model. Further optimization can also be made in the selection of the AC waveform to improve the performance of the plasma actuator. Corke et al. [9] have proven that the use of a sawtooth waveform with a long rise time corresponding to the forward-charge cycle phase when electrons are deposited on the dielectric surface, produces more induced thrust compared to sine waves. In fact, it has been generally understood that triangle waves are an optimal choice compared to sine, square, or rectangular pulses that are less favorable in providing for the cascade ionization of the neutral air in SDBD plasma actuators. It will be imperative to explore these waveforms, and analyze the differences they make in our simulations.

Alterations along the same line could be made to facilitate for the use of an AC voltage in the Orlov model. Currently, the absence of a time-dependent factor or a time counter bars the Orlov algorithm from using an AC voltage to model the plasma actuator problem and allow for comparison with the results from the PIC model. By setting grounds for such modifications, we would be able to combine our results with the deductions made involving the use of optimal electrode gaps and widths, and replicate Erfani's measurements.

7.1.4 Dielectric Material Considerations

Following this, we studied the *use of different dielectric materials.* Two dielectric media of choice including Teflon and Plexiglass were tested. Having thoroughly compared the magnitudes registered for the plasma body force, electric field, and the electric potential between the two dielectric media, we found Teflon to be the most favorable dielectric medium for the plasma actuator system registering a maximum body force of 0.0010 N, and an electric field of 227 N/C. We reached the same conclusion with the results from the Orlov model where we registered a maximum body force magnitude of 2.10×10^{-6} N, and an electric field magnitude of 60 N/C. Through these simulations we were able to accomplish our objective to show that different dielectric materials do have an influence in the mechanical output of the SDBD plasma actuator. Future work would involve similar tests being made with the use of an AC voltage supplied to the electrodes, while also addressing questions pertaining to certain characteristics of the plasma actuator system such as:

i. Does the use of particular dielectric surfaces restrict or even regulate the AC voltage magnitudes supplied to the electrodes?

ii. Which dielectric surfaces are most effective in sustaining the plasma discharge mechanism of the SDBD plasma actuator?

7.1.5 Flight Speeds

Last but not least, we *tested the PIC model under flight conditions.* While Cases (i) (260 m/s), and (iv) (500 m/s) violated the plasma stability criterion, Cases (ii) (990 m/s), and (iii) (977.55 m/s), nearly avoided the same fate registering values of 0.9920, and 0.9999 for the product $\omega_{pi}\Delta t$. We observed that as v_{Drift} approaches stable conditions, the airfoil-like distribution of particles dipped lower towards the dielectric surface. Furthermore, we found that by approaching flight speed conditions, the system presents higher magnitudes for the electric field, and body force contours. In Case (iii), we find the maxima for the electric field, and the plasma body force to be 178 N/C, and 3.2843×10^{-4} N. Case (i) results with a maximum plasma body force magnitude of 9.1×10^{-4} N, and a maximum electric field magnitude of 223 N/C. While these values tend to agree with the observations mentioned earlier, Case (i) violates the plasma stability criterion, and thus its results are invalid.

The plasma stability criterion involves the variables ω_{pi}, the ion plasma frequency, and dt, the particle propagation time-steps. The plasma frequency can be modified by changing the particle number density, n_0, used in the simulation. dt can be modified by changing both the cell size (which we generally equate with the Debye length, and so as mentioned earlier, making the correct choice for this parameter is highly influential to our results), and the drift velocity of the particles. Having maintained the default values for all parameters, while singularly modifying the drift speed, Cases (i) and (iv) are found to be in violation of the plasma stability criterion. This begs the question on what the results may be if the appropriate number densities, and cell sizes were used in these simulations, for the selective flight speed of 260 m/s.

7.2 Conclusion

Throughout this thesis, we have been plagued by the discrepancies between the results from the Orlov and PIC models. While we found that our results agreed upon a patterned characterization of the phenomena, for example, in the consideration of dielectric materials, where Teflon was identified as the favorable dielectric medium in both the Orlov and the PIC models, the results did not agree numerically.

Hoping to set these differences straight, we also tried an additional test where we played around with the magnitudes of the two model's solver tolerances. Three cases were tested for varying tolerance levels,

i. Tol $= 0.0001$
ii. Tol $= 0.00001$
iii. Tol $= 1 \times 10^{-10}$

but no discernible differences were found in the results for all three cases, in both the Orlov and the PIC models. In fact, the results were practically identical. There was literally zero margin for difference. Case (iii) resulted in a failure for convergence involving the potential solver in the PIC model. The smaller the tolerance level, the greater the number of iterations that were required. This was disadvantageous in the case of the PIC model where the given tolerance was not only beyond the typical range used for the matrix solver, but also because of the necessity for a greater number of iterations. Unlike the Orlov model, which is quite flexible in this criteria, the PIC model is computationally intensive, thus making the necessity for a greater number of iterations, an additional complication. In the end, we were unable to label a unique reason behind the numerical differences that persist in the results between the two models.

So what is the purpose of all this experimentation? Through the cases we have considered in Chapter 6, we have furthered our knowledge on the functionality, and various aspects of the two models. By doing so, we were able to identify their advantages and deficiencies in modeling the plasma actuator. It is now particularly suggestive that a simulation compiling the various aspects of each of the cases considered in this chapter be made, and can be easily accomplished.

Such a simulation would have the SDBD plasma actuator system configured with the optimal electrode gaps, widths, dielectric materials, as have been identified in our simulation, while supplied with a sawtooth AC voltage waveform, and tested under flight conditions that satisfy the plasma stability criterion, where the cell width will be resolved to a Debye length that provides for the best resolution in our results along with an acceptable tolerance criterion specific to each model.

Nevertheless, there still remains a bounty of questions on the observations we have made so far. While our analyses have provided for the distinctions between the two models, there is much left to do towards a complete understanding of their properties, and inherent differences. This will be the subject of the following chapter, where the basis of these questions will be laid bare, along with a conclusive note on further work that can be pursued on this subject.

Chapter 8

Toward the Future

8.1 A Brief Recap

The primary objective of this thesis was to model the SDBD plasma actuator flow problem. Two approaches involving different models, Orlov's fluid Electrostatic model and the author's hybrid Particle-In-Cell model, were considered. Having outlined the theory involved in implementing the two models, they were then tested using different sets of parameters and constraints. The corresponding results were summarized and discussed in Chapters 6 and 7. So what did we learn from this? Much of this work focused on understanding the basic properties of the SDBD plasma actuator using these two simplified computational models. Consequently we were able to identify key parameters and configurations, specifically in the PIC model, that can influence the dynamic behavior of the SDBD plasma actuator system such as:

i. The use of different dielectric materials for the dielectric barrier.

ii. The correct choice of the Debye length, and the appropriate discretization of the computational grids.

iii. The use of varying electrode geometries involving different electrode widths and gaps.

iv. The use of AC and DC voltages, and their influence in the formation of a stable plasma, and subsequently, the magnitude of the resultant plasma body force field.

v. The appropriate use of particle boundary conditions to replicate a realistic airflow at flight speed conditions.

Through the models, we have successfully learned to distinguish between the inherent limitations of our methods in modeling the SDBD plasma actuator system, as well as explore the myriad characteristics of the flow control device itself. These observations serve as the foundation to a larger effort in learning about the inherent mechanics of the two models,and their applicability to the SDBD plasma actuator flow problem. There is now a necessity for larger effort towards the optimization of both models in order to accommodate for the discrepancies detailed in the numerical results.

Therefore, this chapter will focus on further generalizing the two models with consideration of what we have learned from their numerical results, and the questions that we have encountered. We will end this thesis with a conclusive note on the future work that could be pursued on this subject, and contribute to its applicability in industrial research.

8.2 Questions to Consider

Variables that are known to influence plasma formation and its intensity in the SDBD plasma actuator system include the DC/AC voltage amplitudes and frequencies, electrode configurations, dielectric materials, dielectric thickness, and dielectric temperature, to name a few. It has been shown through various experiments that the correct choice, and selection of these parameters influence the performance of the plasma actuator device.

The tests that have been conducted with the two models form the basis of an optimization problem, involving the plasma actuator system. In that vein, it is normal to question why we chose to use the specific numerical values for the relevant parameters as we did in these two models. The source of our decisions can be relegated to the myriad articles that were utilized for reference, and as supplementary materials in this thesis. In particular, the experimental work of Roth, Orlov, Corke, Enloe, and Moreau et al. [1; 4; 5; 8] assisted greatly in the correct choice of preliminary parameters that could be used test these simplified models. For example, the PIC code uses an electron temperature of 1 eV, and ion temperature of 0.1 eV both of which characterize the plasma temperatures encountered in the SDBD plasma actuator system. The thicknesses of the electrodes were set equivalent to that of a cell width, which in most cases was 7.4 mm which is also fairly representative of the general order of magnitude thicknesses of the electrodes in real experiments. Similarly, the use of set Debye length magnitudes, Particle Injection velocities, and Grid resolutions were also referenced, setting the stage for the myriad tests conducted in Chapter 6. In many ways, our goal was to probe the SDBD plasma actuator system with our models. Therefore the varied parametric values between the PIC and Orlov models were purposely set to facilitate this goal, evolving from preliminary trial values to testing realistic values, ultimately allowing us to explore the basic tenets of the plasma actuator system, the applicability of the two models, and ascertain the great influence of our numerical choices for the system's variables.

In this manner, we gained ample knowledge on the physical nature of the SDBD plasma actuator system. But, along with this knowledge came an equivalent share of questions that must be answered. Our incentive is not to provide a definitive answer to each and every question (as in various cases a unique solution does not exist), but to probe the alternatives, and plausible solutions that may reinforce progress in our research.

8.2.1 Boundary Conditions

Four cases of boundary conditions were analyzed, and were the first of the many results that validated the PIC model and its application to the SDBD plasma actuator flow problem. Unfortunately, it was not possible to compare said results with those of Orlov's model, namely because the electrostatics of the model do not facilitate for the same level of detail in its boundary conditions. This can be readily fixed.

The benchmark Orlov model was set such that it maintained our interest in the plasma physics of the flow problem. This restriction only allowed for selective comparisons to the PIC model. By incorporating the Navier- Stokes equations, the governing equations for the flow problem, the fluid nature of the model can be implemented, and through the use of vorticity and stream functions, provide for greater detail, and flexibility in the configuration of boundary conditions as well as modeling the effects of viscosity. In fact, this was the original approach proposed by Orlov.

8.2.2 Grid Resolutions

One of the main disadvantages of using the MATLAB programming environment was the inability to account for fractional positions in the structural configurations of the electrode sizes and gaps. This could be circumvented by the use of advanced multiphysics software such as Comsol.

The modeling of the plasma actuator flow problem would also benefit from the use of Finite Element Analyis which provides several advantages compared to the basic PIC method constructed in this thesis, such as:

i. The accurate representation of complex geometry.

ii. Capturing local flow effects, which is particularly beneficial if we are to incorporate the Navier-Stokes equation in the Orlov model with that of the electrostatics in the PIC model.

iii. Mesh structure flexibility, particularly with regards to the fractional discretization of the computational domain, adding further precision, and detail to the results.

iv. Inclusion of varying material properties that are encountered in modeling the flow problem.

This method can be applied to great precision in understanding the influence of structural modifications of the plasma actuator system involving the electrodes. Having explored various electrode sizes and gaps, we could also test the influence of different electrode thicknesses. In physical experiments, the electrodes are usually quite thin, on the order of millimeters. Increasing the thickness of the electrode may be influential in the formation of the plasma discharge. Turbulent flows at the end of the electrode may help sweep electrons released about that area into a recirculating region above the encapsulated electrode, further helping sustain the plasma discharge. Such local flow effects involving the dynamics of the charged particles in the plasma, and edge behavior can be easily captured with the use of the Finite Element Analysis method.

Much of this would be influential to our current inability to compare the results obtained from the simulations between the two models, specifically those exercising different electrode gaps and widths. We quoted Forte's analysis of the evolution of the maximum induced velocity of the volumetric SDBD plasma as a function of electrode gap, but were unable to compare it directly to the results obtained in our corresponding simulations, as we did not utilize an AC voltage in our simulations. Although we were able to replicate the use of a Plexiglass dielectric medium in our simulation, the magnitudes presented for the AC voltage, and the wave frequency, were also far too large to simulate, leading to instabilities in our results.

Nevertheless, the results that we compiled from our simulations for varying electrode gaps generally agreed with the observed performance of the SDBD plasma actuator. For example, in one simulation, locating the encapsulated electrode deeper within the dielectric medium resulted in greater magnitudes for the electric field, as well as the body force. This agreed with proven experiments that higher velocities can be induced along the dielectric surface for a given voltage, for similar configurations [32].

8.2.3 AC Voltage

The PIC model was constructed using a constant potential of ± 1 V on the exposed, and encapsulated electrode. Orlov utilizes the same configuration in his electrostatic model. It would be necessary to incorporate the application of an AC voltage, as in reality, a DC voltage may not provide for the most stable plasma. To accommodate for this, a few simulations were made with the PIC model using an AC voltage on the exposed electrode, while grounding the encapsulated electrode.

In said simulations, apart from small amplitudes and frequencies, the PIC model suffered from instabilities when higher voltage, and frequency magnitudes were utilized (for example, the specifications used in Forte's measurements for the evolution of the induced velocity, with respect to electrode gaps.) This is a limitation of the system but it would be beneficial to address a solution to this problem.

Furthermore, exploring the use of various waveforms, such as the highly efficient saw-tooth waveform [9], may help in ultimately canceling the current restrictions on the PIC model where there is a preference towards a DC versus an AC voltage.

8.2.4 Dielectric Materials

We found that using a Teflon dielectric resulted in the highest value for the electric field, along with the slowest rate of decay of the field away from the upper electrode, compared to the other two dielectric surfaces (Kapton, and Plexiglass). Therefore, the correct choice of dielectric materials has a significant influence in SDBD plasma formation. Erfani et al. [32] have shown that correct material selection can lead to great performance gains, and a reduction in dielectric heating.

Dielectric heating is the process in which a high-frequency alternating electric field (in SDBD actuators, the AC voltage would be the primary source), leads to the heating of the dielectric surface. If the electric field is too strong, this may lead to the rupture of the dielectric material, so it is desirable to not apply extremely high voltages, but rather use high frequencies.

This is why the correct choice of materials for the dielectric surface is very important. Future work on this topic would also consider the following aspects:

i. The various issues or problems that accompany dielectric heating, such as non-uniform heating, voltage gradients etc.

ii. The effects of the dielectric surface on the flow behavior.

iii. The constraints on the AC voltage for the system depending on the dielectric surface to avoid corona, and arcing.

iv. The influence of the dielectric surface on plasma stability.

v. General factors that affect dielectric heating (including electrode gaps).

8.3 Conclusion

Much of the future work to be done on the PIC and Orlov models in simulating the SDBD plasma actuator flow problem will begin with consideration of the following,

i. The PIC model, by way of its potential solver, is restricted in its range of convergence criteria. The current solver involves the use of an iterative method involving residuals, and a matrix solver. Alternative approaches could be considered in the works of Birdsall et al. [29], allowing the PIC model to be enhanced for greater precision, and accuracy in its results. Similar considerations have to be made for the Orlov model. The current solver in the Orlov model utilizes a simplified tolerance criterion. To further improve the accuracy of both methods, higher order finite difference schemes can be utilized to discretize the fundamental equations.

ii. In conjunction with what is mentioned above, various modifications can be made to enhance the PIC model, such as the incorporation of Monte-Carlo collisions, interactions with neutral particles, smoothing and noise aspects, finite size particle simulations, Fourier particle distribution functions etc. The reader is referred to existing literature by Dawson, and Birdsall et al.[28; 29] for details.

iii. Plasma stability conditions are very significant in the PIC model. Various parameters including the domain length, Debye length, particle temperatures, and particle injection velocities must be considered carefully. The simulations that have been performed in this thesis maintained the benchmark settings on the aforementioned parameters. Thus, the next obvious step would be to allow for the correct, and realistic modifications of said parameters such that we can replicate the results of successful physical experiments. A simple case of this issue was addressed in our analysis involving simulations with different particle injection velocities.

The greatest advantage of the hybrid PIC model is its potential to reliably predict the dynamics involved in the SDBD plasma actuator, from the formation of micro-discharges to flow generation. Discharge processes dominate the performance of plasma actuators. The PIC model presented in this thesis is simplified in its approach to the plasma actuator flow problem. Such a hybrid model should achieve the high computational efficiency of the fluid model without compromising the detailed physical description found in a particle model.

In order to optimize the hybrid PIC model, the next step, as mentioned in the list earlier, would be to account for particle interactions. Currently, the hybrid model is configured such that ions are kinetic, while electrons are approximated as a fluid background. The particles do not interact. By incorporating Monte Carlo methods into the model we would be able to simulate charged-particle interactions (ion-electron, electron-electron, ion-ion etc.), and particle-neutral gas collision effects.

The basic equation of motion for binary collisions is the Boltzmann equation, and is given as,

$$\frac{\partial(nf)}{\partial t} + \vec{c}\cdot\frac{\partial(nf)}{\partial\vec{x}} + \vec{F}\cdot\frac{\partial(nf)}{\partial\vec{c}} = n^2\int\int[f(\vec{c}')f(\zeta') - f(\vec{c})f(\zeta)]g\sigma d\Omega d\zeta, \quad (8.1)$$

where f denotes the velocity distribution function. ζ and $\vec{c}'$ are the post-collision velocities of a colliding pair, and are determined from pre-collision velocities ζ

and $\vec{c}$. g is the relative velocity of the colliding pair. $\sigma d\Omega$ is the differential cross section. The Monte Carlo Collision (MCC) method uses a large number of particles to sample random collisional events. The change in position, and momenta of the particles involved in such interactions are estimated stochastically during each time-step of the simulation. The PIC method covers the grounds for electric interactions between charged particles. The inclusion of the MCC method will treat for particle interactions via collisions, and optimize the hybrid PIC method in accurately modeling the plasma dynamics of the SDBD plasma actuator. There is an expansive literature by Birdsall [29] discussing the methods used to simulate electron-neutral elastic collisions, electron-ion Coulomb collisions, such as the Lorentz gas model that have been used to represent such interactions, and how to assimilate such interactions into the PIC model. Such a hybrid model could also be configured to include an interface that would allow for computing between particle, and fluid domains during simulations. Regions with low electric fields, and high charge densities may be treated by the fluid model, and vice-versa by the particle model. This would effectively unite the two models discussed in this thesis. But, at first, it will be necessary to focus our efforts in addressing the lingering questions and doubts, to be resolved between the individual methods.

This concludes our discussion of the work established in this thesis. Two methods including Orlov's fluid Electrostatic model, and the author's hybrid PIC model were evaluated. Their results were accordingly verified, and validated. The generalization of the models, and the necessary requirements for their applicability to simulating physical experiments were extensively analyzed, setting the grounds for future work to be accomplished in the hope of accurately modeling the SDBD plasma actuator flow problem.

Bibliography

[1] Dmitriy M. Orlov. *Modelling and Simulation of Single Dielectric Barrier Discharge Plasma Actuators*. PhD thesis, University of Notre Dame, Graduate School of Aerospace, and Mechanical Engineering, 2006. ii, 4, 8, 9, 12, 14, 25, 26, 43, 64, 103

[2] Gad el Hak. *Flow Control: Passive, Active, and Reactive Flow Management*. Cambridge University Press, New York, 2000. x, 1, 2, 3

[3] Guillermo Artana Maxime Forte Gerard Touchard Eric Moreau, Christophe Louste. Contribution of plasma control technology for aerodynamic applications. *Plasma Process. Polym.*, 3:697–707, 2006. x, 3

[4] J. Roth. *Industrial Plasma Engineering*. Institute of Physics Publishing, London, 2001. x, 10, 15, 17, 26, 32, 40, 41, 103

[5] Stephen P. Wilkison Thomas C. Corke, C. Lon Enloe. Dielectric barrier discharge plasma actuators for flow control. *Annu. Rev. Fluid Mech.*, 42:505–529, 2010. x, 4, 8, 9, 14, 19, 20, 21, 40, 76, 103

[6] Adil Bouchmal. Modeling of dielectric barrier discharge actuator - implementation, validation, and generalization of an electrostatic model. Master's thesis, Delft University of Technology, 2011. 1, 4, 7, 9, 18, 19, 20, 21, 22, 24, 25

[7] G. Touchard. Plasma actuators for aeronautics applications - state of art review. *I.J. PEST*, 2:1–25, 2008. 1, 2, 15

[8] Eric Moreau. Airflow control by non-thermal plasma actuators. *J. Phys. D: Appl. Phys*, 40:605–636, 2007. 3, 4, 7, 8, 12, 13, 15, 17, 40, 96, 103

[9] Dmitriy M. Orlov Thomas C. Corke, Martiqua L. Post. Single dielectric barrier discharge plasma enhanced aerodynamics: physics, modeling, and applications. *Exp Fluids*, 46:1–26, 2009. 4, 7, 8, 9, 12, 15, 76, 96, 106

[10] Wei Shyy Balaji Jayaraman. Modeling of dielectric barrier discharge-induced fluid dynamics and heat transfer. *Progress in Aerospace Sciences*, 44:139–191, 2008. 4, 18, 22, 23, 25, 41

[11] J.A. Bittencourt. *Fundamentals of Plasma Physics*. Springer-Verlag, New York, 2004. 6, 9, 10, 12, 24, 29, 30, 31

[12] J. P. Richardson M. Laroussi, I. Alexeff and F. F. Dyer. The resistive barrier discharge. *IEEE Trans. Plasma Sci*, 30, 2002. 9

[13] D.D. Sijacic U. Ebert, I.R. Rafatov. Structure formation in a dc-driven "barrier" discharge stability analysis and numerical solutions. *28th ICPIG*, 2007. 9

[14] K. Stalter R. Vidmar. Air chemistry and power to generate and sustain plasma: plasma lifetime calculations. *AIAA 1189*, 2003. 14

[15] E. Moreau G. Touchard M. Cazalens M. Forte, J. Jolibois. Optimization of a dielectric barrier discharge actuator by stationary and instationary measurements of the induced flow velocity, application to airflow control. 15, 17, 76, 93

[16] G.I. Font R.S. Mangina, C.L. Enloe. Dielectric barrier discharge-based plasma actuator operation in artificial atmospheres for validation of modeling and simulation. *AIP-Physics of Plasmas*, 22, 2015. 18

[17] E. Lifshitz L.D. Landua. *Electrodynamics of continuous media*. Pergamon, Burlington, MA, 1984. 19

[18] Trevor M. Moeller Richard J. Thompson. Numerical investigations of plasma actuator lorentz body forces. *50th AIAA Aerospace Sciences Meeting*, AIAA 1032:1–9, 2012. 19

[19] L.C. Pitchford J.P. Boeuf. Electrohydrodynamic force and aerodynamic flow acceleration in surface dielectric barrier discharge. *J. App. Phys*, 97, 2005. 19

[20] VanDyken Kachner E. Jumper T. Corke M. Post O. Haddad L. Enloe, T. McLaughlin. Mechanisms and responses of a single-dielectric barrier plasma actuator: geometric effects. *AIAA*, 42:595–604, 2004. 19, 21

[21] D.E. Ashpis Y.B. Suzen, P.G. Huang. Numerical simulations of flow separation control in low-pressure turbines using plasma actuators. *45th AIAA Aerospace Sciences Meeting*, AIAA 937:1–8, 2007. 19

[22] J.D. Jacob D.E. Ashpis Y.B. Suzen, P.G. Huang. Numerical simulations of plasma based flow control applications. *35th AIAA Aerospace Sciences Meeting*, AIAA 937:1–11, 2005. 19

[23] M. Patel D. Orlov, T. Corke. Electric circuit model for aerodynamic plasma actuator. *AIAA*, 2006-1206, 2006. 20, 21

[24] A. Andersson W. Shyy, B. Jayaraman. Modeling of glow discharge-induced fluid dynamics. *J. Appl. Phys.*, 92, 2002. 21

[25] S. Macheret R. Miles A. Likhanskii, M. Shneider. Modeling of interaction between weakly ionized near-surface plasmas and gas flow. *AIAA*, 2006-1204, 2006. 21

[26] D.B. Graves T.E. Nitschke. A comparison of particle in cell and fluid model simulations of low-pressure radio frequency discharges. *J. Appl. Phys.*, 1994. 24

[27] Naofumi Ohnishi Kazuya Sugimoto. Toward hybrid simulation of flow generation in dbd plasma actuator. *28th International Symposium on Rarefied Gas Dynamics*, AIP Conf. Proc.1501:1408–1415, 2012. 25

[28] John M. Dawson. Particle simulation of plasmas. *Reviews of Modern Physics*, 55, 1983. 35, 107

[29] A. Bruce Langdon Charles K. Birdsall. *Plasma Physics via Computer Simulation*. McGraw-Hill Inc., 1985. 38, 46, 50, 51, 107, 109

[30] R.H. Pletcher D.A. Anderson, J.C. Tannehill. *Computational Fluid Mechanics and Fluid Transfer*. Hemisphere Publishing Corporation, Boca Raton, 1984. 42

[31] Gerald Recktenwald. Stopping criteria for iterative solution methods- lecture notes for me 448/548. 49

[32] C. Hale K. Kontis Rasool Erfani, H. Zare-Behtash. Development of dbd plasma actuators: The double encapsulated electrode. *Acta Astronautica 109:132-143*, 2014. 94, 105, 106

Appendix A- Orlov's Electrostatic Model MATLAB Code

```
%---
%The Default Electrostatic Code
%Number of Nodes
%(Nx-1), (Ny-1) = # of square of grids
Nx = 26;
Ny = 26;
%---
%---
%Error and Tolerance
err = 1;
tol = 0.1; %Potential Solver Tolerance
%---
%---
%Domain Lengths
Lx = 0.04; %in m
Ly = 0.04; %in m
%---
%---
%Grid Discretization
dx = Lx/(Nx-1);
dy = Ly/(Ny-1);
Debyeconstant = 0.0000254;
%---
```

```
%---
%Initialization of Potential, and Dielectric Matrices
V = zeros(Nx, Ny);
eps = zeros(Nx, Ny);
%---
%---
%Potential Boundaries
V(1,1:Ny) = 0.0;
V(Nx,1:Ny) = 0.0;
V(1:Nx,1) = 0.0;
V(1:Nx,Ny) = 0.0;
%---
%For the 25x25 Grid
V(22:23,5:13) = 1.0;
V(24:25,13:21) = -1.0;
epskapton = 2.7;
epsair = 1.0;
%New Dielectric Constant conditions over the domain for 201 x 201 grid
for i=1:23
     for j=1:Nx
         eps(i,j) = 1.0;
     end
end
for i=24
    for j=1:Nx
          eps(i,j) = 1.85; %Kapton-Air interface
     end
end
for i=25:26
     for j=1:Nx
          eps(i,j) = 2.7;
     end
end
%---
Vkpl = V;
A = zeros(Nx, Ny);
B = zeros(Nx, Ny);
C = zeros(Nx, Ny);
D = zeros(Nx, Ny);
E = zeros(Nx, Ny);
```

```
%We are considering uniform gridding (no Robert's stretching), and a
%non-uniform dielectric constant.
while err > tol
    for i=2:Ny-1
        for j=2:Nx-1
            x = j*dx;
            y = i*dy;
            %First derivatives of eps with respect to x and y.
            Firstdepsx = (eps(i,j+1)-eps(i,j-1))/(2*dx);
            Firstdepsy = (eps(i+1,j)-eps(i-1,j))/(2*dx);
            A(i,j) = (eps(i,j)/(dy*dy)) + (Firstdepsy/(2*dy));
            B(i,j) = (eps(i,j)/(dy*dy)) - (Firstdepsy/(2*dy));
            C(i,j) = (eps(i,j)/(dx*dx)) + (Firstdepsx/(2*dx));
            D(i,j) = (eps(i,j)/(dx*dx)) - (Firstdepsx/(2*dx));
            E(i,j) = (2*eps(i,j)/(dx*dx)) + (2*eps(i,j)/(dy*dy))
            + (1/(Debyeconstant*Debyeconstant));
            Vkpl(i,j) = (A(i+1,j)*V(i+1,j) + B(i-1,j)*V(i-1,j)
            + C(i,j+1)*V(i,j+1) + D(i,j-1)*V(i,j-1))/E(i,j);
        end
    end
    V = Vkpl;
    err = max(abs(Vkpl-V));
end

FirstdVx = zeros(Nx,Ny);
FirstdVy = zeros(Nx,Ny);
Efield = zeros(Nx,Ny);
Bforce = zeros(Nx,Ny);
for i=2:Ny-1
    for j=2:Nx-1
        FirstdVx(i,j) = (V(i,j+1) - V(i,j-1))/(2*dx);
        FirstdVy(i,j) = (V(i+1,j) - V(i-1,j))/(2*dy);
        Efield(i,j) = (-1)*FirstdVx(i,j) + (-1)*FirstdVy(i,j);
    end
end
for i=2:Ny-1
    for j=2:Nx-1
        Bforce(i,j) = ((-1)*(8.854E-12)*(Debyeconstant)^-2)
        *V(i,j)*Efield(i,j);
    end
```

```
end

%Let's graph our results
uelect(1,:) = [5 13];
uelect(2,:) = [22 23];
lelect(1,:) = [13 21];
lelect(2,:) = [24 25];
object1 = zeros(26,26);
object2 = zeros(26,26);

for i=uelect(1,1):uelect(1,2)
object1(i,uelect(2,1):uelect(2,2)) = ones(uelect(2,2)-uelect(2,1)+1,1);
end
for i=lelect(1,1):lelect(1,2)
object2(i,lelect(2,1):lelect(2,2)) = ones(lelect(2,2)-lelect(2,1)+1,1);
end

[j,i] = meshgrid(1:1:Nx,Ny:-1:1);
a=figure(1);
hold on;
contour(j,i,V);
contour(flipud(object1'),[1 1],'-k','LineWidth',2);
contour(flipud(object2'),[1 1],'-k','LineWidth',2);
hold off;
title('Potential Field')
xlabel('Lx')
ylabel('Ly')
z1 = colorbar;
ylabel(z1, 'Electric Potential (V)');

b=figure(2);
hold on;
contour(j,i,Efield);
contour(flipud(object1'),[1 1],'-k','LineWidth',2);
contour(flipud(object2'),[1 1],'-k','LineWidth',2);
hold off;
title('Electric Field')
xlabel('Lx')
ylabel('Ly')
z2 = colorbar;
```

```
ylabel(z2, 'Electric Field (N/C)');

c=figure(3);
hold on;
contourf(j,i,Bforce);
contour(flipud(object1'),[1 1],'-k','LineWidth',2);
contour(flipud(object2'),[1 1],'-k','LineWidth',2);
hold off;
title('Body Force')
xlabel('Lx')
ylabel('Ly')
z3 = colorbar;
ylabel(z3, 'Body Force (N)');
```

Appendix B - The Hybrid PIC Model MATLAB Code

```
global eps0 qe den A n0 phi0 phi_p_u phi_p_l Te Ti uelect lelect kapton

eps0= 8.854E-12;        %Permittivity of free space
epsair = 1.0;           %Dielectric constant for air
epskapton = 2.8;        %Dielectric constant for kapton
qe = 1.602E-19;         %Elementary charge
k = 1.381E-23;          %Boltzmann constant
amu = 1.661E-27;        %Atomic mass unit
M = 32*amu;             %Ion mass (Molecular oxygen)

%Input settings
n0 = 1E12;              %Particle number density in #/m^3
phi0 = 0;               %Reference Potential
Te = 1;                 %Electron temperature in eV
Ti = 0.1;               %Ion temperature in eV
v_drift = 70000;        %Ion injection velocity in m/s

%Voltage on the electrodes
phi_p_u =1;
phi_p_l = -1;

%Plasma parameters
Debye = sqrt(eps0*Te/(n0*qe));  %DebyeLength
vth = sqrt(2*qe*Ti/M);          %Thermal velocity
```

```
%Domain paramaters
nx = 26;                %Number of nodes in x-direction
ny = 26;                %Number of nodes in y-direction
ts = 400;               %Number of time steps
dcell = Debye;          %Cell Size
np_insert = (ny-1)*15;  %Insert np_insert particles per cell
nn = nx*ny;             %Total number of nodes
dt = 0.1*dcell/v_drift; %Time steps
Lx = (nx-1)*dcell;      %Domain Length in x direction
Ly = (ny-1)*dcell;      %Domain Length in y direction
wpi = sqrt(n0*qe*qe/(amu*eps0)); %Ion plasma frequency

if((wpi*dt)>1)
    disp('(wpi*dt) > 1!! Unstable Conditions!');
    break
end

%Electrode dimensions for 26 x 26 grid
uelect(1,:) = [5 13];
uelect(2,:) = [4 5];
lelect(1,:) = [13 21];
lelect(2,:) = [2 3];

%We create an object domain for visualization.
object1 = zeros(nx,ny);
object2 = zeros(nx,ny);

for j=uelect(2,1):uelect(2,2)
object1(uelect(1,1):uelect(1,2),j) = ones(uelect(1,2)-uelect(1,1)+1,1);
end
for j=lelect(2,1):lelect(2,2)
object2(lelect(1,1):lelect(1,2),j) = ones(lelect(1,2)-lelect(1,1)+1,1);
end

%Specific Weight calculations
flux = n0*v_drift*Ly;   %Flux of entering particles
npt = flux*dt;          %# of real particles created per timestep
spwt = npt/np_insert;   %Specific weight
mp_q = 1;               %Macroparticle charge
max_part = 50000;       %Buffer size
```

```
%Setup particle array for allocation
part_x = zeros(max_part, 2);     %Particle positions
part_v = zeros(max_part, 2);     %Particle velocities

%Set up multiplication matrix for potential solver
A = zeros(nn);
eps = zeros(nx,ny);

%Dielectric Constant conditions over the domain for 25 x 25 grid
%Region above Upper Electrode
for i=1:nx
    for j=4:ny
    eps(i,j) = 1.0;
    end
end
%Within the Dielectric
for i=1:nx
    for j=1:2
        eps(i,j) = 2.7;
    end
end
%At the Dielectric Interface
for i=1:nx
    for j=3
        eps(i,j) = 1.85;
    end
end
%Set up the stencil on the internal nodes
for i=2:nx-1
    for j=2:ny-1
      u = (i-1)*ny+j;
      Firstdepsx = (eps(i+1,j) - eps(i-1,j))/(2*dcell);
      Firstdepsy = (eps(i,j+1) - eps(i,j-1))/(2*dcell);
      A(u,u) =
      -4*eps(i,j)/(dcell*dcell);
      A(u,u-1) =
      (eps(i,j)/(dcell*dcell))-(Firstdepsx)/(2*dcell);
      A(u,u+1) =
      (eps(i,j)/(dcell*dcell))+(Firstdepsx)/(2*dcell);
```

```
      A(u,u-nx)=
      (eps(i,j)/(dcell*dcell))-(Firstdepsy)/(2*dcell);
      A(u,u+nx)=
      (eps(i,j)/(dcell*dcell))+(Firstdepsy)/(2*dcell);
    end
end

%y=0
for i=1:nx
    %j=1
    u=(i-1)*ny+1;
    %phi(i,j)
    A(u,u) = -1/dcell;
    %phi(i,j+1)
    A(u,u+1) = 1/dcell;
end

%y=Ly
for i=1:nx
   %j=ny
    u =(i-1)*ny+ny;
    %phi(i,j-1)
    A(u,u-1) = 1/dcell;
    %phi(i,j)
    A(u,u) = -1/dcell;
end

%x=Lx
for j=1:ny
    %i=nx
    u=(nx-1)*ny+j;
    A(u,:) = zeros(1,nn);   %clear row
    %phi(i-1,j)
    A(u,u-nx) = 1/dcell;
    %phi(i,j)
    A(u,u) = -1/dcell;
end
```

```
%x=0
for j=1:ny
   %i=1
    u=j;
    A(u,:) = zeros(1,nn);   %clear row
    A(u,u) = 1;             %phi(i,j)
end

for j=uelect(2,1):uelect(2,2)
    for i=uelect(1,1):uelect(1,2)
         u=(i-1)*ny+j;
         A(u,:)=zeros(1,nn);
         A(u,u)=1;
    end
end

for j=lelect(2,1):lelect(2,2)
    for i=lelect(1,1):lelect(1,2)
        u=(i-1)*ny+j;
        A(u,:)=zeros(1,nn);
        A(u,u)=1;
    end
end

phi = ones(nx,ny)*phi0;
np=0;   %Clear number of particles

disp('Solving potential for the first time.
Please be patient, this could take a while.');

%%%%%%%%%%%%%%%%%%%%
%MAIN LOOP
%%%%%%%%%%%%%%%%%%%%

for it=1:ts     %Iterate for ts timesteps
    %Reset Field Quantities
    den = zeros(nx,ny);     %Number density
    efx = zeros(nx,ny);     %Electric field, x-component
    efy = zeros(nx,ny);     %Electric field, y-component
    chg = zeros(nx,ny);     %Charge distribution
```

```
%*** 1. CALCULATE CHARGE DENSITY ***

%Deposit charge to nodes
for p=1:np  %Loop over particles
    fi = 1+part_x(p,1)/dcell;   %Real i index of particle'scell
    i = floor(fi);              %Integral part
    hx = fi-i;                  %Remainder

    fj = 1+part_x(p,2)/dcell;   %Real j index of particle's cell
    j= floor(fj);               %Integral part
    hy = fj-j;                  %Remainder

    %Interpolate charge to the nodes. This follows the method of
    %weighted averaging
    chg(i,j) = chg(i,j) + (1-hx)*(1-hy);
    chg(i+1,j) = chg(i+1,j) + hx*(1-hy);
    chg(i,j+1) = chg(i,j+1) + (1-hx)*hy;
    chg(i+1,j+1)= chg(i+1,j+1) + hx*hy;
end

%Calculate Density
den = spwt*mp_q*chg/(dcell*dcell);

%Apply boundaries
den(1,:) = 2*den(1,:);
den(nx,:) = 2*den(nx,:);
den(:,1) = 2*den(:,1);
den(:,ny)= 2*den(:,ny);

%Add density floor for plotting and to help the solver
den = den + 1E4;

%*** 2. CALCULATE POTENTIAL ***
phi = PotentialSolver(phi);

%*** 3. CALCULATE ELECTRIC FIELD ***
efx(2:nx-1,:) = phi(1:nx-2,:) - phi(3:nx,:);
efy(:,2:ny-1) = phi(:,1:ny-2) - phi(:,3:ny);
efx(1,:) = 2*(phi(1,:)-phi(2,:));
```

```
efx(nx,:) = 2*(phi(nx-1,:)-phi(nx,:));
efy(:,1) = 2*(phi(:,1)-phi(:,2));
efy(:,ny) = 2*(phi(:,ny-1)-phi(:,ny));

efx = efx/(2*dcell);
efy = efy/(2*dcell);
uniformE = zeros(nx,ny);
%Calculate Electric Field using Poisson's equation
uniformE = efx + efy;
bforce = zeros(nx,ny);
%Calculate the body force
bforce = -(eps0/(Debye*Debye))*phi*uniformE;

%*** 4. GENERATE NEW PARTICLES ***
if(np+np_insert>=max_part)
     np_insert = max_part-np;
end

part_x(np+1:np+np_insert,1) = rand(np_insert,1)*dcell;
part_x(np+1:np+np_insert,2) = rand(np_insert,1)*Ly;

part_v(np+1:np+np_insert,1) = v_drift+(-1.5+rand(np_insert,1)
+ rand(np_insert,1)+rand(np_insert,1))*vth;
part_v(np+1:np+np_insert,2)= 2*(-1.5+rand(np_insert,1)
+rand(np_insert,1) +rand(np_insert,1))*vth;
np = np+np_insert;

%*** 5. MOVE PARTICLES ***
p = 1;
while(p<=np)
    fi = 1+part_x(p)/dcell;      %i index of particle's cell
    i  = floor(fi);
    hx = fi-i;                   %fractional x position in cell

    fj = 1+part_x(p,2)/dcell;    %j index of particle' cell
    j = floor(fj);
    hy = fj-j;                   %fractional y position in cell

    %gather electric field
    E=[0 0];
```

```
 E = [efx(i,j) efy(i,j)]*(1-hx)*(1-hy);  %from (i,j)
 E = E + [efx(i+1,j) efy(i+1,j)]*hx*(1-hy);  %(i+1,j)
 E = E + [efx(i,j+1) efy(i,j+1)]*(1-hx)*hy;  %(i,j+1)
 E = E + [efx(i+1,j+1) efy(i+1,j+1)]*hx*hy;  %(i+1,j+1)

 %update velocity and position
 F = qe*E;                           %Lorentz force, F=qE
 a = F/M;                            %acceleration
 part_v(p,:) = part_v(p,:)+a*dt;     %update velocity
 part_x(p,:) = part_x(p,:)+part_v(p,:)*dt;   %update position

 %process boundaries
 %DEFAULT BOUNDARY CONDITIONS

 %reflective boundary on bottom
 if (part_x(p,2)<0)                  %y<0
 part_x(p,2) = -part_x(p,2);     %move particle back to domain
 part_v(p,2) = -part_v(p,2);     %reverse y-velocity
 end

 %see if particle is inside upper electrode
 in_uelect=false;
 if ((i>=uelect(1,1) && i<uelect(1,2)) && ...
     (j>=uelect(2,1) && j<uelect(2,2)))
      in_uelect=true;
 end

 in_kapton=false;
 if ((i>=1 && i<nx) && ...
     (j>0  && j<lelect(2,2)))
     in_kapton=true;
 end

%absorbing boundary on left, right, top or if in object
 if (part_x(p,1)<0 || part_x(p,1)>=Lx || part_x(p,2)>=Ly
 || in_uelect || in_kapton)
     part_x(p,:) = part_x(np,:);
     %kill particle by replacing it with last particle,
     %i.e. absorbing conditions
     part_v(p,:) = part_v(np,:);
```

```
            np = np - 1; %reduce particle count
            p = p-1;
            %reduce particle index so this entry will be processed again
        end

        p=p+1; %move to the next particle
    end

%*** 6.PLOT RESULTS ***%

if(mod(it,25) == 0 || it==ts)     %plot only every 25 time steps

        a=figure(1);
        hold on;
        contourf(den');
        contour(object1',[1 1],'-k','LineWidth',2);
        contour(object2',[1 1],'-k','LineWidth',2);
        hold off;
        title(sprintf('Density-26x26- %i', it));
        xlabel('Lx')
        ylabel('Ly')
        z1=colorbar;
        ylabel(z1,'Density (1/m^3)');

        b=figure(2);
        hold on;
        contourf(phi');
        contour(object1',[1 1],'-k','LineWidth',2);
        contour(object2',[1 1],'-k','LineWidth',2);
        hold off;
        title(sprintf('Potential-26x26- %i', it));
        xlabel('Lx')
        ylabel('Ly')
        z2=colorbar;
        ylabel(z2,'Electric Potential Density (V)');

        c=figure(3);
        contour(object1',[1 1],'-k','LineWidth',2);
        contour(object2',[1 1],'-k','LineWidth',2);
        scatter(part_x(1:np,1)/dcell,part_x(1:np,2)/dcell,5,'fill');
```

```
        title(sprintf('Particle Positions-26x26- %i', it));
        xlabel('Lx')
        ylabel('Ly')
        hold off;

        d=figure(4);
        hold on;
        contourf(uniformE');
        contour(object1',[1 1],'-k','LineWidth',2);
        contour(object2',[1 1],'-k','LineWidth',2);
        hold off;
        title(sprintf('uniformE-26x26- %i', it));
        xlabel('Lx')
        ylabel('Ly')
        z3=colorbar;
        ylabel(z3,'Electric Field (N/C)');

        e=figure(5);
        hold on;
        contour(bforce1');
        contour(object1',[1 1],'-k','LineWidth',2);
        contour(object2',[1 1],'-k','LineWidth',2);
        hold off;
        title(sprintf('bforce1-26x26- %i', it));
        xlabel('Lx')
        ylabel('Ly')
        z4=colorbar;
        ylabel(z4,'Body Force Fields (N)');

    end
    disp(sprintf('Time Step %i, Particles %i',it, np));

end

disp(sprintf('Complete!\n'));                   %exit
toc

%%%%%%%%%%%%%%%%%%%%%%%%%%%%%%%%%%%%%%%%%%%%%%%%%%%%%%%%%%%%%%%%%%%%
```

```
%POTENTIAL SOLVER
function [x] = PotentialSolver(phi)
global A den n0 phi0 Ti Te phi_p_u phi_p_l uelect lelect qe eps0 kapton
tol = 0.1;  %Solver Tolerance
nx = size(den,1);
ny = size(den,2);
nn = numel(den);
b0 = reshape(permute(den,[2 1]),numel(den),1);
x = reshape(permute(phi,[2 1]),numel(phi),1);
%Solve
for it=1:2000
    %Recalculate RHS
    b = b0 - n0*exp((x-phi0)/Te);
    b = -b*(qe/eps0);
    b(1:nx) = phi0;         %Fixed potential on x = 0
    b(nn-nx+1:nn) = 0;      %Zero Electric field on x = L
    b(nx:nx:nn)= 0;         %Zero Electric field on y = L;
    b(1:nx:nn) = 0;         %Zero Electric field on y = 0;

    for i=uelect(1,1):uelect(1,2)
        b([uelect(2,1):uelect(2,2)]+(i-1)*ny)
        = ones(uelect(2,2)-uelect(2,1)+1,1)*phi_p_u;
    end
    for i=lelect(1,1):lelect(1,2)
        b([lelect(2,1):lelect(2,2)]+(i-1)*ny)
        = ones(lelect(2,2)-lelect(2,1)+1,1)*phi_p_l;
    end
    %Update nodes
    for i=1:nn
        %xold = x;
        x(i) = (b(i) - A(i,1:i-1)*x(1:i-1)-A(i,i+1:nn)*x(i+1:nn))/A(i,i);
    end
    %Compute residue to check for convergence, do only every 10 iterations
    if mod(it,10)==0
        R=norm(b-A*x);  %Residue
        %disp(R);
        if(R<=tol)
            %disp(sprintf(' GS converged in %i iterations with norm
            %g',it,R));
           break;
```

```
        end
    end
end
%Check if the solver converged to the specified tolerance
if(R>tol)
    disp('GS Failed to converge!!');
end
%Return solution as a nx*ny array
x=reshape(x,nx,ny);
x=reshape(reshape(permute(x,[2 1]),nx,ny),nx,ny);
```